

Experimental evidence for narrow baryons in the mass range $1.0 \leq M \leq 1.46$ GeV

B. Tatischeff¹ *, J. Yonnet¹, M. Boivin², M. P. Comets¹, P. Courtat¹,
R. Gacougnolle¹, Y. Le Bornec¹, E. Loireleux¹, F. Reide¹,
and N. Willis¹

¹*Institut de Physique Nucléaire, CNRS/IN2P3, F-91406 Orsay Cedex, France*

²*Laboratoire National Saturne, CNRS/IN2P3, F-91191 Gif-sur-Yvette Cedex, France*

()

The reaction $p p \rightarrow p \pi^+ X$ was studied at different incident energies around $T_p=2$ GeV. Narrow baryonic structures were observed in the missing mass M_X and in the invariant mass $M_{p\pi^+}$. The masses of these structures are: 1004, 1044, 1094, 1136, 1173, 1249, 1277, and 1384 MeV (and possibly 1339 MeV). Some of them were also observed at the same masses in the missing mass spectra of the $d p \rightarrow p p X$ reaction although with a weaker signature. Many checks were performed to make sure that these structures were not produced by experimental artifacts. Several narrow small amplitude peaks, were also extracted using already published photo-nucleon cross sections. The small widths of all these results, and the stability of the observed structures, regardless of the experiment, were used to conclude that they are genuine baryons which and not merely the consequence of dynamical rescatterings. These baryons cannot be associated with classical q^3 quark configurations. We associate them with two colored cluster quark configurations.

PACS numbers: 14.20.Gk, 12.40.Yx, 13.75.Cs, 14.20.Pt

I. INTRODUCTION

For a number of years narrow structures have been observed in hadronic spectra. Isovectorial dibaryons were first observed [1] (and references therein), then other narrow dibaryon isospin states [2]. Narrow structures were also observed later in baryons [3] and in mesons [4] [5] [6]. Since these structures were observed at stable masses, whatever the reaction, incident energy or production angle, they were associated

*Corresponding author: B. Tatischeff, E-mail: tati@ipno.in2p3.fr

with real hadrons and not with final state rescatterings. There is no room for new low mass mesons within the many quark models for mesons, that consider only $q\bar{q}$ configurations, given the excellent agreement between observation and calculations [7]. Once again there is no room in the mass range $M \leq 1.5$ GeV for new baryons within the many quark models for baryons, if we consider only qqq configurations. The classical baryonic spectrum, which corresponds to broad resonances, is rather well understood. This is not the case for the narrow structures observed.

An interpretation was tentatively proposed to explain these narrow and exotic hadrons, associating them with two colored quark clusters. It was shown in the already quoted references that such an attempt allows to reproduce the masses with models using a very small number of adjusted parameters (from zero to two), depending on the hadronic species in question. In these models, where the exotic hadron arises from a partial deconfinement, we would expect small narrow amplitude signatures throughout the complete hadronic spectra. This paper presents the analysis and the results obtained in order to check this idea in low mass baryons. Preliminary results concerning the three first exotic baryons have previously been published [3].

This paper is constructed in the following way: in Sec II we will describe the detector performances, and the data processing; in Sec. III the various normalizations applied in order to get the cross sections will be described; the simulation used to make some of these normalizations and to test the complete experimental device will be discussed in Sec. IV whereas the various checks performed in order to underline our confidence in the genuine reality of the observed structures are presented in Section V. In Section VI the results of our two experiments are presented, namely:

- the $p p \rightarrow p \pi^+ X$ reaction, studied at three incident energies: $T_p=1.52$ GeV, 1.805 GeV, and 2.1 GeV and several forward angles. Narrow baryons were looked for in the missing mass M_X and in the invariant mass $M_{p\pi^+}$;
- the missing mass of the $\bar{d} p \rightarrow p p X$ reaction was studied at two incident deuteron energies: $T_d=1.722$ GeV and 2.1 GeV.

We compare the masses of our structures to the masses of small structures which can be extracted from various reactions studied with incident hadrons or leptons by different collaborations. The observed masses will be discussed in section VII within a phenomenological model based on two quark cluster configurations. Finally, the last part is devoted to conclusions.

II. EXPERIMENT

A. Experimental description

The measurements were performed at the Saturne synchrotron beam facility. The proton beam energies were 1.52 GeV, 1.805 GeV and 2.1 GeV, and the deuteron beam energies were 1.72 GeV and 2.1 GeV. The particles were detected using the SPES3 spectrometer and detection system (see Fig. 1). The main properties of the spectrometer were:

- a solid angle of ± 50 mrad in both the horizontal and vertical planes, and
- a large momentum range ($600 \text{ MeV} < p < 1400 \text{ MeV}$) at $B=3.07 \text{ T}$.

The liquid H_2 target of 393 mg/cm^2 was held in a container with $130 \mu\text{m}$ thick Ti windows. External heat shields comprised of $24 \mu\text{m}$ thick aluminium were placed in the beam-line on either side of the target. The beam particles/burst varied between $10^8/\text{burst}$ and $5 \times 10^8/\text{burst}$, depending on the spectrometer angle and the incident energy. It was chosen in such a way that the acquisition dead time was less than 10%. The vertical angular acceptance was determined using the spectrometer magnetic field map and GEANT code [8]. The drift chambers, the trigger and the acquisition code were conceived in order to detect, to identify and to measure the properties of two-particle reactions.

Several drift chambers were used to reconstruct the particle trajectories. The first chamber C1 [9] (called “MIT-type”), was situated on the spectrometer focal plane. Its spatial and angular horizontal resolutions are : $\sigma_x=90 \mu\text{m}$ and $\sigma_\theta=18 \text{ mrad}$ respectively. Its efficiency was carefully calibrated using the other drift chambers. Two multidrift chambers, C2-C3 (called the “CERN-type” chambers), placed perpendicular to the average particle direction, were designed to get information on trajectories in the horizontal and vertical planes. However, due to the small vertical magnification of the spectrometer (≈ 0.14), the ϕ resolution at the target was too poor to be useful.

The trigger consisted of four planes of plastic scintillator hodoscopes. The first and last planes were each made of 20 scintillators each. The dimensions of each plastic detector were $12 \times 40 \text{ cm}^2$ for the first plane (A), and $18 \times 80 \text{ cm}^2$ for the last plane (B). The time of flight baseline from the first scintillator plane to the last one was 3 m. Particles were identified by their time of flight between the A_i and B_j detectors and also by their energy loss in the A_i detectors. This latter measurement was mainly used to discriminate between one and two charged particles. Mean-timers and constant fraction discriminators were used and the time resolution for each scintillator was typically $\sigma = 180 \text{ ps}$. The large horizontal angular magnification of the spectrometer produced a large horizontal angular opening (up to 30°) of the trajectories at the output of the spectrometer. This resulted in a large number of useful $A_i B_j$ combinations (125), between the first and last scintillator planes, which required the same number (125) coincidences. It is important to note that a mean range of $\approx 200 \text{ MeV}/c$ (25% of the focal plane momentum dependant acceptance) is seen by each $A_i B_j$ combination. Therefore, there is a large overlap between

many $A_i B_j$ trigger combinations for each spectrometer momentum. The count rate at each momentum value is then less liable to be influenced by errors from the scintillator efficiency. Careful trigger efficiency measurements of all the 125 combinations were performed using a system of scintillator counters moving in front of the A-hodoscope and behind the B-hodoscope. The mean value of the trigger efficiency was $\approx 95\%$.

When the scattering angle or the incident energy vary, the mean value of the missing mass M_X moves for a given $A_i B_j$ coincidence.

B. MIT drift chamber efficiency

The MIT drift chamber was located in the focal plane of the spectrometer. It therefore played a major role in our detection system, justifying a careful efficiency calibration. The efficiency of the MIT drift chamber was evaluated using the CERN drift chambers, by calculating the ratio of the number of times where all three detectors were hit to the number where only the two CERN chambers were hit. Figure 2 shows that this efficiency displays a slowly varying value as a function of position. Consequently this efficiency correction cannot be a source of eventual structures. In Fig. 2 the circles correspond to events where two particles were detected, and the triangles to single particle events. Thanks to the large momentum bite of the spectrometer, the data were taken without having to move the magnetic field. Consequently, the regularly spaced structures seen in the results cannot be attributed to an eventual mis-treatment of the MIT drift chamber efficiency.

C. Pion-proton identification

In Fig. 3, four typical time of flight raw spectra, chosen among the 125 different possibilities, are shown. We observe the quality of the particle identification by looking at the two peak separation corresponding to pion and proton times of flight. The four inserts correspond to different spectrometer mean momenta and different angles. The inserts (a), (b), (c), and (d) correspond respectively to 1.36 GeV/c (top spectrometer momentum value), 1.25 GeV/c, 1.00 GeV/c, and 0.83 GeV/c. The separation is always very good, even on the high momentum side.

A second level trigger filters the events that are stored. This was done thanks to a second time of flight between both detected particles which was used online in order to control the intensity dependent random hit rate. The same device was also used offline in order to reject the very small amount of misidenti-

fied particles between pions and protons at the top of the momentum range (see Fig. 3(a)). The time measured was corrected using the particle momenta, the corrections being calculated from the variable distances from the target to the first scintillating plastic hodoscope plane A. After pedestal corrections and variable distance corrections, the time differences of all the $A_i A_j$ time of flights ($20 \times (20-1)/2 = 190$ combinations) were plotted on the same histogram and are shown in Fig. 4. We observe a tail due to accidental coincidences to the left of the peak. A window of ± 9 channels, as drawn on the figure, was used in the detailed data analysis. Incorrect proton-pion identifications fell around channel -21, and can be seen as a small peak in the figure. These misidentified proton-pion events correspond to events that lie in the tail crossovers of the particle identification at the top end of the momentum scale (see Fig. 3(a)). The spectra of the first time of flight (Fig. 3) were vetoed by the second time of flight.

D. Mass resolution

An important property of the experiment is the good mass resolution, essential when narrow and weakly excited structures are being looked for. The resolution in the invariant mass was measured using the final state interaction peak (FSI) from the $p p \rightarrow p p X$ reaction. Figure 5 shows these distributions for all three energies, vertically shifted in order to keep the figure easy to read. Here, full circles, squares, and triangles correspond respectively to results from $T_p = 1.52$ GeV, 1.805 GeV, and 2.1 GeV incident energies. The total experimental resolution is $\sigma \approx 0.9$ MeV.

The resolution of the missing mass was measured in the neutron missing mass from the $p p \rightarrow p \pi^+ X$ reaction at forward angles. Figure 6 shows the missing mass spectrum, on a logarithmic scale, when the incident proton beam was $T_p = 1.805$ GeV and the spectrometer angle $\theta = 0.75^\circ$. Here, the experimental resolution is $\sigma \approx 2.2$ MeV. The resolution of the missing mass lowers for increasing angles.

We clearly see three structures in Fig. 6, between the neutron peak and the Δ bump. They are unexpected since there is no room for new low mass and narrow baryons within the many quark models [10]. Many checks were performed to ascertain the real presence of these new physical structures and they will be discussed in detail in Sec. V.

III. CROSS SECTION DETERMINATION

Several normalizations were performed in order to extract the cross sections and several corrections were applied which take into account accidental coincidences, lost events, angular vertical acceptances,

and drift chamber and trigger efficiencies. The beam flux was calibrated with the help of two telescopes in direct view of the target and an ionisation chamber downstream of the beam. These three detectors were calibrated using ^{12}C activation measurements. The data must also be normalized to the two detected particle momenta ranges. Indeed these momentum dependant acceptances vary for different missing masses (or invariant masses), different reactions, spectrometer angles and different incident energies. Figure 7 shows these variations for the missing mass of the $p p \rightarrow p \pi^+ X$ reaction at $T_p=1.805$ GeV and $\theta=0.75^\circ$. This normalization was done for all cross sections presented. The momentum dependant acceptances were obtained from analytical relations or numerical fits to real or simulated data (see later in section V.A). We have checked that the same final cross sections were obtained independently of the choice made for this normalization. The empty line in the figure will be discussed in the next paragraph.

IV. SIMULATION

A simulation code was written in order to study the properties of the spectrometer and detectors. All experimental parameters were found to be well understood, and no narrow structures are observable in the simulated histograms. The simulation allows us to evaluate the corrections for the lost events. Vertical angular acceptance corrections were previously determined with GEANT. The main events lost are those where both particles detected have the same momentum. These events define a narrow empty valley that can be seen clearly in Fig. 7. Such a small region, where important losses occur, is without consequence when M_X from $p p \rightarrow p \pi^+ X$ is considered, but important for a narrow region in $M_{p\pi^+}$ (mainly for neutron missing masses). This region of invariant mass was eliminated from further consideration in order to avoid the introduction of fake structures via a substantial renormalization.

Figure 8 shows a comparison between the neutron missing mass data and the corresponding simulation for the $p p \rightarrow p \pi^+ X$ reaction at $T_p=1.52$ GeV and $\theta=0^\circ$. Inserts (a) and (b) show data, whereas inserts (c) and (d) show the corresponding simulated results. Inserts (a) and (c) show that these events came from the total momentum range ($0.6 \leq pc \leq 1.4$ GeV). Both neutron missing mass peaks are shown in inserts (b) and (d). They are regular and do not display any internal structures. Had there been dead wires in the detectors, we would have expected regions of varying density. This is not observed. There is no evidence either of the opposite situation of self excited wire amplifiers. In Fig. 8 the cross section variation for $p p \rightarrow p \pi^+ n$ which differs between data and simulation, explains the difference in intensity between inserts (a) and (c).

V. CHECKS

A careful internal calibration of all elements was undertaken, and all possible cross checks were carried out in order to evaluate the level of confidence that can be attributed to the existence of the observed structures. In the following we provide the description of the used procedures.

A. Selection of different momenta ranges

Several tests were performed in order to verify that the structures were not produced in a limited region of momenta. The data from the $p p \rightarrow p \pi^+ X$ reaction at $T_p=1.52$ GeV and forward angles were used. The neutron peak was removed by software cuts in order to enhance the missing mass region of interest. The statistics are consequently reduced but the figures 9, 10, and 11 show that the structures remain [11].

B. Selection of different angular ranges

Different angular cuts were performed during the analysis in order to test that our structures remain for different angular ranges inside our horizontal aperture of ± 50 mrad. Figure 12 shows that is indeed the case. The data of the $p p \rightarrow p \pi^+ X$ reaction at $T_p=1.805$ GeV and $\theta=0.75^\circ$ are presented in four different angular ranges. Here the range is defined around the mean horizontal direction of the spectrometer aperture.

C. The structures do not depend on the spin state of the incident beam

Figure 13 shows the missing mass of the $\vec{p} p \rightarrow p \pi^+ X$ reaction at $T_p=1.805$ GeV and $\theta=0.75^\circ$. The inserts (a) and (b) correspond to the two spin states of the incident particles. We observe that the structures are present in both cases.

D. Structures not present in accidental coincidences

Figure 14 shows the comparison between the real events and the accidental coincidences of the missing mass from the $p p \rightarrow p \pi^+ X$ reaction at $T_p=1.805$ GeV and $\theta=0.75^0$. The accidental coincidences are defined by software cuts in a range 12 times larger than the true $p\text{-}\pi^+$ coincidences. The corresponding histogram does not display any structure.

E. Empty target measurements

The effect of the target windows was checked by regular empty target measurements performed during the data taking. The count rates were always small, typically $\leq 5\%$. Figure 15 shows one comparison of full target to empty target measurements. The missing mass data from the $p p \rightarrow p \pi^+ X$ reaction at $T_p=1.805$ GeV and $\theta=0.75^0$ are presented. Here both spectra correspond to the same incident proton flux. We observe the absence of structures in the empty target data. We deduced that the target windows were not a source of a noticeable contamination. We also deduced that although our measurements were performed at small angles, the data were not contaminated by any hot area of incident beam which could have been scattered by some mechanical element at the entrance of the spectrometer.

F. Possible effect of particles emitted outside the spectrometer solid angle and slowed down

We consider here the possibility to attribute the narrow structures to an eventual slowing down of the detected particles (p and-or π^+). The particles could be emitted outside the solid angle and then could be partially absorbed by the lead diaphragm and-or other mechanical elements at the entrance of the spectrometer. A careful simulation of this possible effect was performed. There is no problem in the horizontal plane. But since the vertical angular magnification of the spectrometer is small (≈ 0.14), the drift chambers were not precise enough to make clear vertical cuts. The spectrometer aperture is ± 50 mrad. Trajectories emitted vertically up to ± 80 mrad were simulated and particles emitted with momenta up to 2 GeV/c were studied (the maximum detection momentum is 1.4 GeV/c). Figure 16 shows the result of the simulation normalized to the missing mass of the neutron peak (logarithmic scale). There is clearly no problem outside the $1.06 \leq M_X \leq 1.11$ GeV range for the missing mass of the $p p \rightarrow p \pi^+ X$ reaction at $T_p=2.1$ GeV and $\theta=0.7^0$. A similar result was found [12] for a comparable simulation performed under different experimental conditions, namely the $p p \rightarrow p \pi^+ X$ reaction at $T_p=1.805$ GeV and $\theta=0.75^0$. A

broad peak is observed inside the range $1.06 \leq M_X \leq 1.11$ GeV for eventual fake events slowed down by the lead diaphragm.

Trajectories for increasing angles ($|\Delta \phi| \geq 50$ mrad) are progressively cut by the magnet, the yoke and the detectors. For the detectors, this is particularly true at both extremities, since the trajectories envelope fit exactly the trigger dimensions, which correspond to $\Delta \phi = \pm 50$ mrad. Figure 11 illustrates clearly the presence of structures in these extreme momenta regions, where the fake effect discussed here cannot be present.

There are additional arguments excluding this effect which could attribute the narrow structures to particles slowed down by the slits. If the structures were produced by the neutron peak shadows, then:

- for increasing spectrometer angles, the simulation shows that:
 - the mass of the broad fake peak will increase (up to 20 MeV),
 - its width will increase (up to 75 MeV);
- the ratio of the cross sections of the structures versus the neutron missing mass cross sections should be flat;
- the analyzing powers of the structures and of the neutron missing mass peak should always be equal.

None of these characteristics are observed. We concluded therefore that this type of contamination was not present.

VI. RESULTS

All the checks described till now lead us to conclude that genuine structures are observed. Each corresponding mass and width was obtained using a polynomial distribution for the background and a gaussian one for the peak. The precision of the extracted peaks was determined by the corresponding number of standard deviations (S.D.):

$$S.D. = 1/\sqrt{2} \sum_{i=1}^n [(N_{Ti} - N_{Bi})/\Delta\sigma_i^2] / \left[\sum_{i=1}^n (1/\Delta\sigma_i^2) \right]^{1/2} \quad (1)$$

where the sum is done over the n different channels describing the peak. N_T and N_B describe the total and background count rates of each channel, $\Delta\sigma_i$ is the corresponding statistical error and the factor $1/\sqrt{2}$ comes from the assumption that the error on N_B is the same as the error on N_T .

The next step in the analysis is to try to study to what they can be connected, and understand where these structures come from. The main point will be to see if, whether or not, they appear at stable masses. The answer will be given after looking at the different results.

A. Ranges of baryonic mass studied by different reactions

Figure 17 shows the useful range of baryonic missing masses studied below $M=1.46$ GeV. The three (two) narrow strips for each reaction correspond to the three (two) different incident energies, increasing from left to right, for the reactions studied. The variations of these limits for different spectrometer angles are small and therefore not pointed out. The statistics are not regularly distributed. At both sides of each range the statistics are poor, therefore narrow structures could exist in these cases, and have not been extracted in this study. The short horizontal lines indicate the mass of the observed narrow structures to be discussed in the following paragraphs.

It is sometimes possible to observe small shoulders, or peaks, in publications of data obtained from various reactions studied for different aims. The corresponding experimental resolutions are usually lower than in our experiment. These shoulders or peaks are generally not commented on by the authors. In a few cases they are assumed (without calculation) to be the rescattering of particles in the final state. The cross sections of the $np \rightarrow pX$ reaction, measured at 0° at nine incident energies at LAMPF [13], exhibit several structures. For example in this publication a peak can be observed (at $T_n=673$ MeV, i.e. $M_X \approx 1136$ MeV and $\sigma \approx 10$ MeV).

Some other results will be discussed later in sections VI.E, F, and G, and their data will be shown.

B. The missing mass of the $p p \rightarrow p \pi^+ X$ reaction

The first results from this reaction were already published [3], [12]. Figure 18 shows the scatterplot of proton momenta against pion momenta from $T_p=2.1$ GeV and $\theta=0.7^\circ$ events. The same events, after kinematical transformations, are shown in Fig. 19 where the missing mass M_X is plotted versus the invariant $M_{p\pi^+}$ mass. In both figures, we see clearly the neutron missing mass and the intense broad $\Delta - \Delta$ region. Several narrow lines can be perceived at fixed missing masses between the neutron and Δ missing masses. The empty narrow band, as already explained in section IV, corresponds to lost events where both the p and π^+ have the same momentum. Figures 20 and 21 show the corresponding data at lower energy: $T_p=1.805$ GeV and $\theta=0.75^\circ$. The data in Fig. 21, projected onto the missing mass axis, are shown in Fig. 6. We see clearly the neutron and the Δ peaks, and also small structures between the two. In order to enhance these structures, we remove the neutron peak by applying software cuts. Figure 22 shows the result for the $p p \rightarrow p \pi^+ X$ reaction at $T_p=1.805$ GeV and $\theta=0.75^\circ$ after this selection, whereas Fig. 23 shows the cross section at the same energy but for $\theta=3.7^\circ$. A good definition of the structures with respect to the background is obtained.

For these structures to have any meaning we would expect them to appear at the same masses, independently of the spectrometer angle and independently of the incident energy. In order to see if this is true, the cross sections as a function of missing mass, are shown in figures 24 and 25 for different forward angles and at all three proton beam energies. The different results are arbitrarily separated by a translation to allow a better observation. In both figures the vertical straight lines are drawn at the same masses. We observe that the structures are present in nearly all spectra, and when present, are observed at fixed masses: 1004 MeV, 1044 MeV, and 1094 MeV. The associated number of standard deviations (S.D.) vary between 2 and 16.9 [3]. Due to the large background, the widths of the structures, and therefore their production cross sections, are inextricable. The mass of the first two structures is $M \leq M_N + M_{\pi^+}$. It is impossible to extract the widths of these structures since they are expected to be much smaller than that attainable by the experimental resolution. These widths are narrow since no strong interaction disintegrations can occur at these masses.

When all three structures at $M=1004$ MeV, 1044 MeV, and 1094 MeV are observed at nearly all angles and energies, narrow structures are also observed at higher masses, but lightly excited and therefore more rare. Consequently they may be observed with a small S.D. and so making them less certain. They are kept when observed several times at neighbouring mass values. These results are presented in the following subsections. The final mass is the mean value of the masses observed when the structures were present. The results will be presented later in section VII.A, regrouping the different spectra, from different reactions, for each narrow structure mass.

C. The invariant masses from the $p p \rightarrow p \pi^+ X$ reaction.

Only the results from the $M_{p\pi^+}$ invariant masses will be discussed. The $M_{X\pi^+}$ invariant masses are larger than $M=1.46$ GeV and the corresponding results will be presented in a forthcoming paper. The maximum mass range of the $M_{p\pi^+}$ varies with the incident proton energy (and is slightly dependent on the spectrometer angle) as indicated in Fig. 17. This upper limit is imprecise since the count rates at the upper edge of the $M_{p\pi^+}$ invariant mass are very low. Again, in this mass range several narrow structures were observed although less excited than in $M_X \leq 1.1$ GeV. They were subsequently observed in certain kinematical configurations and sometimes with a low S.D. and so are less certain. These results will be discussed later (see later Fig. 36, Fig. 37, and Fig.38).

D. The missing mass from the $\vec{d} p \rightarrow p p X$ reaction.

This reaction was studied some time ago [14]. First results on the tensor analyzing powers and vector analyzing powers of the invariant M_{pp} mass were studied with the aim of searching for narrow dibaryons. Small structures in the missing mass M_X were observed, but their low S.D. prevent us from concluding that narrow baryons were observed. The situation is different today since the masses of the narrow structures once observed, are very close to those observed now in the more recent $p p \rightarrow p \pi^+ X$ measurements. Therefore, the results from the $\vec{d} p \rightarrow p p X$ reaction are consistent with the observed structures.

These results are shown in figures 26, 27, 28, 29, 30, 31, and 32. They will be discussed in the next subsections. Figures 26 and 27 display the number of events (as opposed to cross sections), since initially corrections for inefficiencies and acceptances were not available. The migration to more modern computing systems has prevented further analysis of this data since it became impossible to read the data from the original magnetic tapes. The lack of any sharp variation in the acceptance corrections, as now observed in the $p p \rightarrow p \pi^+ X$ data analysis, allows us to consider these spectra.

E. Invariant mass distributions of the $\gamma n \rightarrow p \pi^- \pi^0$ reaction.

Different reactions of double-pion photoproduction on a nucleon were studied experimentally and analyzed theoretically [15]. The multitude of baryonic resonances which must be considered in the intermediate states produce different channels which can interfere, and consequently an oscillatory cross section shape can be observed. However, these oscillations are broad [15] in comparison to the widths considered in the present work and cannot be the cause of eventual structures having $\sigma \approx 10$ MeV. The data from such measurements, performed in order to study the reaction mechanism in double-pion photoproduction, cannot generally be used for the present study because of the large spacing between adjacent $N\pi$ invariant masses. This is the case for the total cross sections of the following reactions: $\gamma p \rightarrow p \pi^- \pi^+$, $\gamma p \rightarrow n \pi^+ \pi^0$, and $\gamma p \rightarrow p \pi^0 \pi^0$ measured at MAMI [16]. This is also the case for the Compton scattering by the proton [17] measured at MAMI, and references therein.

An exception to this is the $\gamma n \rightarrow p \pi^- \pi^0$ reaction. This reaction was studied by Zabrodin *et al.* [18] at MAMI in the photon energy range $500 \leq T_\gamma \leq 800$ MeV. The $(p\pi^0 + p\pi^-)$ spectra were integrated over 50 MeV bins of the incident photon energy. The experiment was clearly not performed with the purpose of looking for eventual narrow baryons, and therefore the statistics for this purpose are poor. However, some structures can be observed which were not discussed by the authors. With the aim of seeing where they lie with respect to the other narrow structures, we extracted these peak values. Figure

33 shows a selection of the results of [18], and table III describes the range of integration of the incident photon energy, the mass extracted and the corresponding S.D. Each peak will be discussed separately in this text in subsections I to P.

F. Cross section of the $\gamma p \rightarrow \pi^+ n$ reaction

This reaction was studied at the Bonn 2.5 GeV electron synchrotron, using a photon incident energy of $0.3 \leq T_\gamma \leq 2.1$ GeV [19]. The experiment was performed in order to study the electromagnetic structure of the nucleon resonances formed in the s-channel. The excitation functions were measured at six different backward angles. At all angles the cross sections decrease quickly up to a total energy of $W=1.3$ GeV, and some narrow structures can be observed at larger masses. The cross sections were integrated over two channels, and fits of these narrow structures in the range $1.3 \leq W \leq 1.44$ GeV were performed. Figure 34 shows some of the results obtained and correspond to four angles, whereas table IV describes the quantitative values extracted from the previous fits. The result for each peak will be discussed separately in this text in subsections I to P.

G. The $pd \rightarrow ppX$ reaction

This reaction was studied with the 305 MeV proton beam of the Moscow Linear Accelerator [20]. The authors observed narrow dibaryons in the pX system and narrow baryonic peaks at 966 MeV, 986 MeV, and 1003 MeV in the missing mass M_X . They suggest that the narrow baryons observed at masses below the pion disintegration threshold mass, “are not excited states of the nucleon, but resonancelike states caused by possible existence and decay of narrow dibaryons. They cannot give contribution to the Compton scattering on the nucleon”. Their largest mass: 1003 MeV, corresponds to our lightest narrow exotic structure at $M=1004$ MeV. Their two lightest masses correspond to a range not studied in the present work.

H. Structure at $M=1004$ MeV

A structure at this mass can be perceived with varying clarity in the missing mass of the $p p \rightarrow p \pi^+ X$ reaction at the three energies (Figs. 22, 23, 24, and 25). This low mass is outside the range of the invari-

ant $M_{p\pi^+}$ mass of the $p p \rightarrow p \pi^+ X$ and also outside the range of the missing mass of the $\vec{d} p \rightarrow p p X$ reaction at $T_d=1722$ and 2100 MeV.

Two shoulders were observed in the missing mass M_n of the $p_d p_i \rightarrow \pi^+ p n$ reaction (deuteron vertex) in an experiment performed at Dubna using 3.34 GeV/c deuterons [21]. The masses of these shoulders: $M \approx 1.0$ GeV and $M \approx 1.05$ GeV are close to the masses of our two first narrow baryons. A peak at the same mass was observed in the $p d \rightarrow p p X$ reaction [20] (see previous subsection VI G.).

I. Structure at M=1044 MeV

A small structure at this mass was observed in the missing mass of the $p p \rightarrow p \pi^+ X$ reaction at all three incident energies studied (Fig. 22, 23, 24, and 25). This low mass is also outside the range of the invariant $M_{p\pi^+}$ mass of the $p p \rightarrow p \pi^+ X$. There is an indication (with a small S.D.) of the presence of a structure in the missing mass M_X of the $\vec{d} p \rightarrow p p X$ reaction. This can be seen in insert(a) of Fig. 26, and in the tensor analyzing power (Fig. 29) and in the vector analyzing power (Fig. 31).

A shoulder at this mass was also observed in the missing mass M_n of the previously cited Dubna experiment, namely the $p_d p_i \rightarrow \pi^+ p n$ reaction [21].

J. Structure at M=1094 MeV

A structure at this mass is clearly observed in the missing mass of the $p p \rightarrow p \pi^+ X$ reaction (figures 22, 23, 24, and 25). As an example, let us consider some quantitative information concerning this missing mass peak. At $T_p=1.805$ GeV and $\theta=90^\circ$, we have $M_X=1092.3$, $\sigma=10.7$ MeV, and S.D.=8.1. This low mass is also outside the useful range of the invariant $M_{p\pi^+}$ mass of the $p p \rightarrow p \pi^+ X$ since it is too close to threshold. There are some small indications of the presence of a different amplitude around this mass in several analyzing powers of the $\vec{d} p \rightarrow p p X$ reaction. They appear in Fig. 28 and in inserts (c) and (d) of Fig. 29.

Figure 33 shows two structures in this mass region, extracted from the $\gamma n \rightarrow \pi^- \pi^0 n$ reaction studied at MAMI [18]. The invariant $p\pi$ masses found (1086.5 MeV and 1080.6 MeV and in table III) are too small and imprecise since they are close to threshold (≈ 1075.5 MeV). The $\gamma p \rightarrow \pi^+ \pi^0 n$ reaction was also studied at MAMI [22]. Although the authors said that “deviations of the experimental data from the phase space distribution are evidence for resonant or meson intermediate states in the $\pi^+ \pi^0$ production”, it is useful to point out that in $M_{n\pi^0}$ and $M_{n\pi^+}$ invariant masses, a narrow peak at $M \approx 1.095$ GeV is

observed at low incident photon energies (their Fig. 2). The virtual Compton scattering in the nucleon resonance region was studied at JLAB (Hall A) [23]. A small peak ($\sigma \approx 12$ MeV) was observed (insert (a) of their Fig. 3) at $W \approx 1.098$ GeV. The $pp \rightarrow pp\pi^0$ reaction was studied at Uppsala [24]. In this work the $p\pi^0$ invariant mass displays a good agreement between measured and Monte-Carlo simulations, except in the 1090-1100 MeV mass region (their Fig. 18). So all these combined, independent observations point to the same conclusion, namely an unidentified state at 1094 MeV.

K. Structure at M=1136 MeV

This was observed in the $M_{p\pi}$ invariant mass at $T_p=1805$ MeV and 2100 MeV (see Table V). Figure 35 shows four inserts where a small peak was extracted from the data in this mass region. Table V indicates the masses found, the corresponding experimental widths, the number of S.D., the incident energy, and the spectrometer angle.

A small structure at $M_X=1140$ MeV was observed in the $\vec{d} p \rightarrow p p X$ reaction (insert (c) of Fig. 26). Small structures in this mass region were extracted at $M \approx 1129$ MeV and 1146 MeV, from the $\gamma n \rightarrow p \pi^- \pi^+$ reaction (inserts (a) and (b) of Fig. 33, and Table III).

L. Structure at M=1173 MeV

Figure 36 shows four inserts showing a shoulder at this mass in the invariant $M_{p\pi^+}$ spectrum. Table VI describes the corresponding results. This structure is not observed in the missing mass. Only at $T_p=1805$ MeV and $\theta = 3.7^\circ$ is there a very small peak at 1162 MeV, but with a very low S.D. (S.D.=1).

A small structure at $M_X=1178$ MeV was observed in $\vec{d} p \rightarrow p p X$ reaction at $T_d=1722$ MeV (insert (d) of Fig. 26). In the same reaction at $T_d=2100$ MeV, a structure was extracted at 1171 MeV (insert (c) of Fig. 26).

A small peak was observed at 1184 MeV (insert (d) of Fig. 33), in the $\gamma p \rightarrow p\pi^+\pi^-$ reaction studied at MAMI [18].

There is an indication of a small and narrow structure at $W \approx 1168$ MeV, in the total π^0 electro-production cross section studied at JLAB (Hall A) [23] (see σ_{Tot} in their Fig. 1). In the same paper there is also a small indication at the same mass observed in the virtual Compton scattering excitation curve (at $\Phi = 0^\circ$).

M. Structure at M=1249 MeV

Figure 37 is comprised of four inserts showing a shoulder in the invariant $M_{p\pi^+}$ mass from the $p p \rightarrow p \pi^+ X$ reaction at $T_p=1.52$ GeV. Table VII describes these results.

A shoulder was also observed in the missing mass of the $\vec{d} p \rightarrow p p X$ reaction (insert (a) of Fig. 27 and Table II).

There is a very small indication of a structure at a mass close to 1246 MeV in the total π^0 electro-production cross section studied at JLAB (Hall A) [23].

N. Structure at M=1277 MeV

Figure 38 shows three inserts where a shoulder in the invariant $M_{p\pi^+}$ mass and in the missing mass of the $p p \rightarrow p \pi^+ X$ reaction is observed. Table VIII regroups these results.

A shoulder was extracted at 1272 MeV in the $\gamma p \rightarrow p\pi^+\pi^-$ reaction studied at MAMI [18]. Figure 33 (insert (c)) and Table III show the associated values.

O. Structure at M=1339 MeV

A small structure in the missing mass $M_X=1327.1$ MeV was observed at $T_p=2.1$ GeV and $\theta = 9^\circ$ (Fig. 38 (d)). This mass should normally not be mentioned from this single result, but peaks at nearby masses were observed in previously published data from other experiments. Two structures were extracted from the $np \rightarrow pX$ cross section [19] at $M=1337$ MeV for $\theta = 120^\circ$ and at 1345 MeV for $\theta = 135^\circ$ (see Fig. 34). A peak was extracted from the $\gamma p \rightarrow \pi^+ n$ reaction [18] at $M=1347$ MeV (see Fig. 34).

P. Structure at M=1384 MeV

Figure 39 shows two inserts where a shoulder in the missing mass of the $p p \rightarrow p \pi^+ X$ and $d p \rightarrow p p X$ reactions is observed. Table IX describes the results. A structure at $M=1369$ MeV, $\sigma=14.5$ MeV, and $S.D.=3.6$ was already observed in Fig. 38 (d).

A shoulder was extracted at 1392 MeV from the $\vec{d} p \rightarrow p p X$ reaction (insert (b) of Fig. 27 and Table II).

A peak at the same mass was extracted from the cross sections of the $\gamma p \rightarrow \pi^+ n$ reaction studied at

Bonn [19]. It was observed at four angles. Table IV and Fig. 34 show the results extracted after an integration over two channels. The mean mass value from that experiment is $M=1385.8$ MeV, very close to the mass 1384 MeV extracted from our data.

In the chiral constituent quark model, the calculated spectrum of N-like $qqq\bar{q}$ states [25] exhibits two states $J^P=1/2+$ and $3/2+$, ($T=1/2$) at $M \approx 1366$ MeV. This mass is not very far from our experimentally observed state at 1384 MeV. There is no indication concerning the width of this calculated state. Since there are no lower calculated masses, an identification between this calculated state and the one found experimentally at $M=1384$ MeV, is rather improbable.

VII. DISCUSSION

A. General discussion

Three strongly excited structures were observed in the missing mass spectra at $M_X=1004$ MeV, 1044 MeV, and 1094 MeV. Several lightly excited structures were observed at heavier masses. They were considered when observed several times at the same mass to within a few MeV. Their non-observation in other spectra is associated with their small cross section, making them difficult to extract or observe. The existence of these structures is strengthened by the fact that they are usually observed in invariant masses. Indeed the confidence on small peaks observed in missing masses may be smaller. Moreover these structures are observed in various independent experiments. Some peaks were not considered since they were not observed several times in our data. A good example of such a case is the spectrum of $M_{p\pi}$ invariant mass at $T_p=1.805$ GeV and $\theta = 0.75^0$, where a structure was extracted at 1232 MeV.

Figure 40 shows all masses discussed previously along with those presented from our measurements as well as those extracted from previously published data from different experiments. The horizontal bands correspond to the mean mass ± 3 MeV. Table X allows to connect the different experiments to the marker plot on Fig. 40. It is worth noting that very few mass structures lie outside the range defined by the horizontal bands of Fig. 40.

The only high precision experiment previously dedicated to looking for narrow baryons was performed at TRIUMF [26]. The reaction studied was $p p \rightarrow B^{++} n$ (in fact $p + CH_2 \rightarrow B^{++} X$) at 460 MeV. In this experiment a hypothetical doubly charged baryon B^{++} was looked for behind a spectrometer and was not observed in the limit of 0.75 pb/sr. There were two reasons to look for a doubly charged baryon: - if it exists, it would be easier to identify among a large flux of singly charged protons and pions, - since only a weak decay would be possible ($B^{++} \rightarrow p e^+ \nu_e$) its lifetime should be long enough, at least 10^{-2} s on the basis of the hyperon lifetime, making it possible to detect behind a spectrometer [26].

Since this hypothetical doubly charged baryon was not observed, we concluded on the isospin 1/2 for our first exotic baryons observed. Such an isospin attribution agrees with our quark cluster mass formula (see later, section VII.B) and with the diquark model of Konno [27] (see later, section VII.C).

Another experiment was studied before [28] at KEK, using a 12 GeV proton beam, with the aim of looking for long lived exotic hadrons with charge ± 2 or $-5/3$. Once again no candidate was found. This experiment was performed in somewhat unfavorable experimental conditions: composite target (platinum), very long detection line (36 m), rather small solid angle ($\Delta\Omega \approx 1$ msr), and a small momentum dependent acceptance ($\Delta p/p \approx \pm 3\%$). The negative result again agrees with the isospin attribution ($T=1/2$) of our narrow, low mass exotic baryons. Below $M=1.2$ GeV, only one calculated mass (at 1139 MeV) can have $T=1/2$ or $3/2$ (see next subsection).

Figure 17 shows the masses of the narrow structures observed in this work. We note that there are only a few cases where a structure could be observed and was not.

Since we have not observed the structures in excitation spectra with slowly increasing incident energy, we are sheltered from any possible cusp effect (threshold energy for the production of any heavier meson). Moreover the threshold energy for these cusp effects would be different for different reactions, such as $p p \rightarrow p \pi^+ X$ and $d p \rightarrow p p X$. This effect is the only one sometimes advocated to explain the experimentally observed narrow structures.

As already discussed, there is no room for new, low mass and narrow baryons within the many quark models [10]. These models use several parameters, and the baryonic masses calculated depend on the set of parameters chosen (see for example [29]). Within the mass range discussed in this work, the number of baryons found is equal to the number of experimental baryons for each T and J^P even if the calculated masses are sometimes much lower. For example, in the calculation of [29], the lowest $N 1/2^-$ and $N 3/2^-$ states are found at masses close to 1360 MeV when their first set of parameters is used.

The experimental determination of the quantum numbers of the observed exotic baryons is outside the scope of the present work. This requires the knowledge of the angular distributions. Also knowing the parity would be very useful, since it would allow the verification of the assumption concerning the number of quarks (anti-quarks) involved.

B. Quark cluster mass formula

In our previous papers, dedicated to narrow dibaryon [1] and meson [5] searches, it was shown that the masses of the experimentally observed narrow structures were in good agreement with those obtained through a simple phenomenological mass formula using two-cluster $q^n \bar{q}^m - q^p \bar{q}^r$ configurations:

$$M = M_0 + M_1[i_1(i_1 + 1) + i_2(i_2 + 1) + (1/3)s_1(s_1 + 1) + (1/3)s_2(s_2 + 1)] \quad (2)$$

where $s_1(s_2)$ and $i_1(i_2)$ are the first (second) cluster spin and isospin values. This formula was derived some years ago [30] for two clusters of quarks at the ends of a stretched bag in terms of color magnetic interactions.

The same approach is employed here. Equation (1) involves a large degeneracy. We made the assumption that the simplest configuration is preferred, otherwise the possible spin and isospin will increase and the parity will be degenerate since additional $q\bar{q}$ configurations will always be possible. The two parameters, described in [3], were adjusted in order to find the mass, spin, and isospin values of the nucleon and the Roper $N^*(1440)$ baryons. Such assumptions lead to the values $M_0=838.2$ MeV and $M_1=100.3$ MeV. This does not mean that we consider our new exotic baryons to be excited states of the nucleon. Indeed there is no simple overlap between q^3 and $q\bar{q} - q^3$, or $q^2 - q$ wave functions.

Figure 41 shows the masses, spins, and isospins obtained using equation (1). We observe the surprisingly good agreement between the experimental masses and the masses calculated without any adjustable parameter, for the four first states. The agreement is in fact excellent for all masses, except two states at $M=1173$ MeV and $M=1384$ MeV. The absence of several masses, predicted by the previous formula, can be related to the fact that they are weakly excited. It is not excluded that more precise experiments will, in the future, observe these states. Below the pion emission threshold at 1075 MeV, the only possible decay channel is the radiative one, and the observed width is due to the experimental resolution.

C. The diquark cluster model

The diquark cluster model was developed over many years [27]. It was used to calculate the masses of the narrow mesonic resonances, the masses of narrow dibaryons, the mass of the exotic $I=2$ meson, and the masses of narrow baryonic states. The model does not assume the existence of colored quark clusters. Different parameters were used which were all determined previously using the data of baryon masses and the ETH group πd phase shifts. The model assumes that these baryons consist of a diquark and a quark, and that the residual interaction between them is negligibly weak. Figure 42 shows the masses of the exotic baryons calculated within this model, the isospin and spin of the levels, and the comparison with the experimental masses observed in this work. With the exception of the levels at $M=1173$ MeV and $M=1249$ MeV, we see that the masses calculated are close to the masses observed experimentally. Once again, there are levels predicted but not observed, and it is not excluded that they exist and could be measured in dedicated experiments in the future.

D. The metastable levels model

It was assumed [31] that the first narrow baryons (with masses lower than 1075 MeV), are metastable levels in the three quark system, as a member of a total antisymmetric representation of the spin-flavor group (20-plet of the $SU(6)_{FS}$). Since such states cannot be excited by one photon or decay to γN , the simplest decay channel is assumed to be $2\gamma N$. In that case, they will not contribute to Compton scattering.

E. Excitation of collective states of the quark condensate

A model was proposed by T. Walcher, which associates the narrow baryonic states below the π threshold production to multiproduction of a genuine virtual Goldstone Boson with a mass close to 20 MeV [32]. This model explains not only the combined experimental results for the narrow nucleon states presented above, but also the states observed in the missing mass M_X of the $pd \rightarrow ppX$ reaction [20] and the rather equidistant level spacing of the narrow dibaryons observed experimentally [1].

F. The chiral-scale bag model

This (CSB) model [33] deals with chiral and scale symmetries of QCD and their violations. It predicts small radii color confinement, and found that the ground states of $SU(3)$ hadrons could be treated as predominantly multi bag states ($Bag\overline{Bag}Bag$ for baryons). This picture allows low mass, narrow excitations with a mean distance ≈ 50 MeV between the almost degenerated spin-isospin states that appear in strongly bound systems dealing with Bag and \overline{Bag} . These narrow excitations are expected for all stable or narrow $SU(3)$ hadrons.

VIII. CONCLUSION

Narrow baryonic structures were observed in the missing mass and in the invariant mass of the $p p \rightarrow p \pi^+ X$ and $d p \rightarrow p p X$ reactions. All final data (missing masses or invariant masses) were the results of two-particle detection. Consequently, it is deduced that any inefficiency or hot point in any detector is unable to produce a narrow peak. If we leave aside the states with masses $1.0 \leq M \leq 1.1$ GeV, the ratio of peak to background is small. However, there is no structure without at least one peak extraction with a number of S.D. ≥ 3.1 (see tables I to IX). Many checks were undertaken which allowed to

conclude that these structures are genuine and not produced by experimental artifacts. Their masses and widths were extracted using polynomials for the background and gaussians for peaks. The widths found are not of a high precision since these peaks are usually much smaller than the physical background. The production cross sections are therefore not precise, and are not discussed further.

The possibility of associating these peaks with dynamical rescattering among final particles, was eliminated for two reasons:

- the structures are narrow,
- they are not spread but they are observed at stable masses for different scattering angles and different incident energies.

We concluded that these peaks correspond to new baryons. There is no room for them within the many theoretical constituent quark models. Indeed the chiral constituent quark model is known [34] to yield a spectrum for the qqq states which agrees well with the empirical baryon spectrum up to $M \approx 1700$ MeV. Moreover, there is no reason for calculations, performed within the qqq assumption, to explain the relatively narrow widths observed in our data. Indeed, a calculation performed within a chiral quark model, investigated the hadronic π and η decay modes of N and Δ resonances [35]. The authors found various decay widths which were dependent on several calculation assumptions. However, for the only baryon that they considered in the mass range of the present study, the Roper resonance $N_{1440} 1/2+$, they calculated a width of the order of several hundreds of MeV for the $\Gamma(N^* \rightarrow N\pi)$ decay mode.

Therefore, we tentatively associate our narrow baryons with exotic baryons made of two colored-quark clusters. The experimental masses agree well with the masses calculated within a phenomenological relation derived twenty years ago for two colored clusters in a spherical MIT type bag. The formula is used as a phenomenological one, but allows to determine the two parameters leading to the masses, spins, and isospin of the nucleon and the Roper resonance. This does not mean that we consider them to be excited states of the nucleon. Indeed, there is no simple overlap between q^3 and $q\bar{q} - q^3$, or $q^2 - q$ wave functions.

Even if the hadronic picture dominated by the baryonic resonances is the relevant degree of freedom, quarks are also relevant at energies as low as the ones considered in this work, and at low momenta transfer. Therefore, the belief of well separated regions, one for the quark-gluon picture and the other for the hadronic picture appears to be too simple.

ACKNOWLEDGMENTS

We are grateful to Dr. M. MacCormick for stimulating comments and help in writing our manuscript in English. We thank Dr. P. Pedroni who provided to us the numerical values of the cross sections from the $\gamma n \rightarrow p \pi^- \pi^0$ reaction studied at MAMI.

-
- [1] B. Tatischeff, J. Yonnet, M. Boivin, M. P. Comets, P. Courtat, R. Gacougnolle, Y. Le Bornec, E. Loireleux, F. Reide, and N. Willis, *Phys. Rev.* **C59**, 1878 (1999).
- [2] Yu.A. Troyan, V.N. Pechenov, E.B. Plekhanov, A.Yu. Troyan, S.G. Arakelian, V.I. Moroz, and A.P. Ierusalimov, Proceedings of the XIII International Seminar on High Energy Physics Problems, Dubna 1998, A. M. Baldin and V. V. Burav editors, Vol.II, p 10; *Phys. At. Nucl.* **63**, 1562 (2000).
- [3] B. Tatischeff, J. Yonnet, N. Willis, M. Boivin, M. P. Comets, P. Courtat, R. Gacougnolle, Y. Le Bornec, E. Loireleux, and F. Reide, *Phys. Rev. Lett.* **79**, 601 (1997).
- [4] J. Yonnet, B. Tatischeff, M. Boivin, M. P. Comets, P. Courtat, R. Gacougnolle, Y. Le Bornec, E. Loireleux, F. Reide, and N. Willis, *Phys. Rev.* **C63**, 014001 (2000).
- [5] B. Tatischeff, J. Yonnet, M. P. Rekalo, M. Boivin, M. P. Comets, P. Courtat, R. Gacougnolle, Y. Le Bornec, E. Loireleux, F. Reide, and N. Willis, *Phys. Rev.* **C62**, 054001 (2000).
- [6] Yu.A. Troyan, E.B. Plekhanov, V.N. Pechenov, A.Yu. Troyan, A.V. Beljaev, A.P. Ierusalimov, and S.G. Arakelian, *Particles and Nuclei Letters* **6[103]**, 25 (2000); *ibid* JINR Rapid Communications **5[91]**, 33 (1998); M.A. Ananjeva *et al.* JINR preprint P1-98-378 (in russian).
- [7] M. Koll, R. Ricken, D.Merten, B.C. Metsch, and H.R. Petry, *Eur. Phys. Journal*, **A9**, 73 (2000).
- [8] CERN Program Library Long Writeup W5013.
- [9] W. Bertozzi *et al.*, *N.I.M.* **141**, 457 (1977).
- [10] S. Capstick and W. Roberts, *Prog. Part. Nucl. Phys.* **45**, 0S241 (2000).
- [11] The structure at $M=1.044$ GeV is rather weakly excited at $T_p=1.52$ GeV, $\theta=2^0$.
- [12] B. Tatischeff and J. Yonnet, Proceedings of the XIII International Seminar on High Energy Physics Problems, Dubna 1998, A. M. Baldin and V. V. Burav editors, Vol.II, p 29.
- [13] B.E. Bonner, C.L. Hollas, C.R. Newsom, P.J. Riley, G. Glass, M. Jain, and B.J. VerWest, *Phys. Rev.* **D27**, 497 (1983).
- [14] B.Tatischeff, M.P. Combes-Comets, P. Courtat, R. Gacougnolle, Y. Le Bornec, E. Loireleux, F. Reide, and N. Willis, *Phys. Rev.* **C45**, 2005 (1992).
- [15] L.Y. Murphy and J.M. Laget, Internal Report (1996), DAPNIA-SPhN-96-10.

- [16] A. Braghieri *et al.*, Phys. Lett. **B 363**, 46 (1995).
- [17] S. Wolf *et al.*, Eur. Phys. J. **A 12**, 231, (2001).
- [18] A. Zabrodin *et al.*, Phys. Rev. **C60**, 055201, (1999).
- [19] H.W. Dannhausen, E.J. Durwen, H.M. Fisher, M. Leneke, W. Niehaus, and F. Takasaki Eur. Phys. J. **A 11**, 441 (2001).
- [20] L.V. Fil'kov, V.L. Kashevarov, E.S. Konobeevski, M.V. Mordovskoy, S.I. Potashev, V.A.Simonov, V.M. Skorkin, and S.V. Zuev, nucl-th/0101021; R. Beck, S.N. Cherepnya, L.V. Fil'kov, V.L. Kashevarov, M. Rost, and Th. Walcher, nucl-th/0104070.
- [21] J. Hlaváčova, V.V. Glagolev, A.K.Kacharova, S.A. Kushpil, N.B. Ladygina, R.M. Lebedev, A.G. Mamulashvili, G. Martinská, M.S. Nioradze, B. Pastirčák, T. Siemiarczuk, J. Urbán, K.U. Khairtdnikov, and M.S.Khvastunov, Phys. of Atom. Nucl. **D60**, 391 (1997).
- [22] W. Langgärtner *et al.*, Phys. ReV. Lett. **87**, 052001, (2001).
- [23] G. Laveissiere *et al.*, Proceedings of the NSTAR 2001 Workshop on the Physics of Excited Nucleons, Mainz 2001, World Scientific, edited by D. Drechsel and L. Tiator, p 271.
- [24] R. Bilger *et al.*, Nucl. Phys. **A693**, 633 (2001).
- [25] C. Helminen and D.O. Riska, Proceedings of the Workshop on The Physics of Excited Nucleons, NSTAR 2001, Mainz, World Scientific, edited by D. Drechsel and L. Tiator, p 217.
- [26] S. Ram, R. Abegg, D. Ashery, D. Frekers, R. Helmer, R.S. Henderson, K.P. Jackson, C.A. Miller, S. Nussinov, E. Piasezky, A. Rahav, A.I. Yavin, and S. Yen, Phys. Rev. **D49**, 3120 (1994).
- [27] N. Konno and H. Nakamura, Lett. Nuovo Cimento, **34**, 313 (1982); N. Konno, H. Nakamura, and H. Noya Phys. Rev. **D35**, 239 (1987); N. Konno, Il Nuovo Cimento **111**, 1393 (1998); H. Noya and H. Nakamura, Proceedings of the IX International Conference on Hadron Spectroscopy, Protvino, Russia, 2001, edited by D. Amelin, to be edited.
- [28] T.T. Nakamura, H. Kobayashi, A. Konaka, K. Imai, A. Masaike, K. Miyake, T. Nagamine, N. Sasao, and Y. Yamada, Phys. Rev. **C39**, 1261, (1989).
- [29] H. Garcilazo, A. Valrace, and F. Fernandez, Phys. Rev. **C64**, 058201, (2001).
- [30] P.J. Mulders, A.T. Aerts, and J.J. de Swart, Phys. Rev. **D19**, 2635 (1979).
- [31] A.P. Kobushkin, nucl-th/9804069.

- [32] T. Walcher, hep-ph/0111279.
- [33] Y.E. Pokrovsky, Proceedings of the 7th Int. Conf. on Hadron Spectroscopy “Hadron’97”, Edited by S.U. Chung and H.J. Wilutzky, AIP, Upton, NY, 1997, p409; Proceedings of the XXXIII Int. Winter Meeting on Nucl. Phys., Edited by I. Iory, Bormio (Italy), 1995, Suppl. N101, 540 (1995).
- [34] S. Simula, Proceedings of the Workshop on The Physics of Excited Nucleons, NSTAR 2001, Mainz, World Scientific, edited by D. Drechsel and L. Tiator, p 135.
- [35] L. Theussl, R. F. Wagenbrunn, B. Desplanques, and W. Plessas, Eur. Phys. J. A. **12**, 91 (2001).

FIG. 1. The SPES3 spectrometer and the associated detection system.

FIG. 2. The MIT drift chamber efficiency. The triangles correspond to the one-particle detection efficiency, whereas the circles correspond to the double hit detection efficiency.

FIG. 3. Time of flight spectra for four $A_i B_j$ combinations consisting of the number of events versus the channel number (125 ps/channel). The four inserts (a), (b), (c), and (d) correspond respectively to the following mean momenta: 1.36 GeV/c, 1.25 GeV/c, 1.00 GeV/c, and 0.83 GeV/c.

FIG. 4. Spectra of the second time of flight comprised of the number of events versus the channel number (250 ps/channel) for all 190 $A_i A_j$ combinations (see text) of the $p p \rightarrow p p X$ reaction at $T_p=2.1$ GeV and $\theta=3^0$.

FIG. 5. Invariant mass of the $p p$ FSI peaks from the $p p \rightarrow p p X$ reaction. Full circles, squares, and triangles correspond respectively to data (vertically shifted) obtained at $T_p=1.52$ GeV, 1.805 GeV, and 2.1 GeV.

FIG. 6. Missing mass spectrum for the $p p \rightarrow p \pi^+ X$ reaction at $T_p=1.805$ GeV and $\theta=0.75^0$.

FIG. 7. Scatter plot of the missing mass versus the proton momenta (insert (a)), and the missing mass versus the pion momenta (insert (b)) from the $p p \rightarrow p \pi^+ X$ reaction at $T_p=1.805$ GeV and $\theta=0.75^0$.

FIG. 8. Neutron missing mass peak from the $p p \rightarrow p \pi^+ X$ reaction at $T_p=1.52$ GeV, $\theta=0^0$. Inserts (a) and (b) correspond to data, inserts (c) and (d) are from simulation.

FIG. 9. The $p p \rightarrow p \pi^+ X$ reaction at $T_p=1.52$ GeV and $\theta=0^0$. Selection of several momenta ranges in inserts (a), (b), (c), and (d) respectively: $p_\pi \geq 1$ GeV/c, $p_\pi \leq 1$ GeV/c, $p_p \geq 1$ GeV/c, and $p_p \leq 1$ GeV/c.

FIG. 10. Missing mass of the $p p \rightarrow p \pi^+ X$ reaction at $T_p=1.52$ GeV and $\theta=2^0$. The four inserts (a), (b), (c), and (d) correspond to events selected by software analysis cuts in the following momenta ranges $0.6 \leq pc \leq 1.4$ GeV (total range), $0.8 \leq pc \leq 1.4$ GeV, $0.6 \leq pc \leq 1.2$ GeV, and $0.8 \leq pc \leq 1.2$ GeV respectively.

FIG. 11. Missing mass of the $p p \rightarrow p \pi^+ X$ reaction at $T_p=1.52$ GeV. In both inserts (a) and (b), a selection on detected particle momenta is made in order to keep only momenta where: $p \leq 0.8$ GeV/c or $p \geq 1.2$ GeV/c. Both inserts (a) and (b) correspond to $\theta=2^0$ and $\theta=5^0$ measurements respectively.

FIG. 12. Missing mass of the $p p \rightarrow p \pi^+ X$ reaction at $T_p=1.805$ GeV, $\theta=0.75^\circ$. The four inserts (a), (b), (c), and (d) correspond to events selected by software cuts in the following angular ranges respectively: $\theta_p \geq 0^\circ$ and $\theta_{\pi^+} \geq 0^\circ$, $\theta_p \leq 0^\circ$ and $\theta_{\pi^+} \leq 0^\circ$, $\theta_p \geq 0^\circ$ and $\theta_{\pi^+} \leq 0^\circ$, and $\theta_p \leq 0^\circ$ and $\theta_{\pi^+} \geq 0^\circ$. Here the range is defined around the mean horizontal direction of the spectrometer aperture.

FIG. 13. Missing mass of the $p p \rightarrow p \pi^+ X$ reaction at $T_p=1.805$ GeV and $\theta=0.75^\circ$. Inserts (a) and (b) correspond to both spin states of the incident proton beam.

FIG. 14. Missing mass of the $p p \rightarrow p \pi^+ X$ reaction at $T_p=1.805$ GeV and $\theta=0.75^\circ$. True coincidences (full circles) are compared to random coincidences (empty squares) defined over a range 12 times greater.

FIG. 15. Missing mass of the $p p \rightarrow p \pi^+ X$ reaction at $T_p=1.805$ GeV and $\theta=0.75^\circ$. Comparison of full (squares) and empty (circles) target data, normalized to the same incident proton beam flux.

FIG. 16. Effect of a possible slowing down of p and π^+ through lead slits and stainless steel rings at the entrance of the spectrometer. $p p \rightarrow p \pi^+ X$ reaction at $T_p=2.1$ GeV and $\theta=0.7^\circ$. Squares correspond to data whereas circles correspond to simulated slower particles, normalized by the same neutron missing mass peak.

FIG. 17. Range of baryonic masses studied in different reactions. The narrow strips correspond to the different incident energies (increasing from left to right for each observed variable and each reaction). The full horizontal lines indicate the masses of the observed narrow structures.

FIG. 18. Scatterplot of p_p versus p_{π^+} events from the $p p \rightarrow p \pi^+ X$ reaction at $T_p=2.1$ GeV and $\theta=0.7^\circ$.

FIG. 19. Scatterplot of missing mass M_X versus invariant mass $M_{p\pi^+}$ from the $p p \rightarrow p \pi^+ X$ reaction at $T_p=2.1$ GeV and $\theta=0.7^\circ$.

FIG. 20. Scatterplot of p_p versus p_{π^+} from the $p p \rightarrow p \pi^+ X$ reaction at $T_p=1.805$ GeV and $\theta=0.75^\circ$.

FIG. 21. Scatterplot of missing mass M_X versus invariant mass $M_{p\pi^+}$ from the $p p \rightarrow p \pi^+ X$ reaction at $T_p=1.805$ GeV and $\theta=0.75^\circ$.

FIG. 22. Cross section of the missing mass of the $p p \rightarrow p \pi^+ X$ reaction at $T_p=1.805$ GeV and $\theta=0.75^\circ$.

FIG. 23. Cross section of the missing mass of the $p p \rightarrow p \pi^+ X$ reaction at $T_p=1.805$ GeV and $\theta=3.7^\circ$.

FIG. 24. Missing mass spectra of the $p p \rightarrow p \pi^+ X$ reaction at $T_p=1520$ MeV and 1805 MeV and at the three smallest angles for both energies.

FIG. 25. Missing mass spectra of the $p p \rightarrow p \pi^+ X$ reaction at $T_p=2100$ MeV at the three measured angles. From top to bottom: $\theta=0.7^\circ$, 3° , and 9° lab.

FIG. 26. Number of events in the missing mass spectra from the $\vec{d} p \rightarrow p p X$ reaction. The experimental conditions corresponding to the inserts (a), (b), (c), and (d) are specified in Table I.

FIG. 27. The $\vec{d} p \rightarrow p p X$ reaction at $T_d=2.1$ GeV and $\theta=17^\circ$. The experimental conditions corresponding to the inserts (a) and (b) are specified in Table II.

FIG. 28. Tensor analyzing power of the missing mass of the $\vec{d} p \rightarrow p p X$ reaction at $T_d=2.1$ GeV and $\theta=17^\circ$.

FIG. 29. Tensor analyzing power of the $\vec{d} p \rightarrow p p X$ reaction at $T_d=2.1$ GeV and $\theta=17^\circ$. The four inserts (a), (b), (c), and (d) correspond respectively to the following cuts applied on M_{pp} : $1876 \leq M_{pp} \leq 1880$ MeV (1S_0) pp state, $1880 \leq M_{pp} \leq 1883$ MeV, $1883 \leq M_{pp} \leq 1886$ MeV, and $1886 \leq M_{pp} \leq 1889$ MeV.

FIG. 30. Vector analyzing power of the $\vec{d} p \rightarrow p p X$ reaction at $T_d=2.1$ GeV and $\theta=17^\circ$.

FIG. 31. Vector analyzing power of the $\vec{d} p \rightarrow p p X$ reaction at $T_d=2.1$ GeV and $\theta=17^\circ$. The inserts have the same definition as those in Fig. 29.

FIG. 32. Tensor and vector analyzing powers of the missing mass of the $\vec{d} p \rightarrow p p X$ reaction at $T_d=1.722$ GeV and $\theta=0^\circ$.

FIG. 33. Invariant mass distributions of the $\gamma n \rightarrow p \pi^- \pi^0$ reaction [17] showing a selection of cross sections where small narrow structures were extracted. The experimental conditions corresponding to the inserts (a), (b), (c), and (d) are specified in Table III.

FIG. 34. Excitation functions of $\gamma p \rightarrow \pi^+ n$ cross sections measured at Bonn [18], after a two-channel integration. The experimental conditions corresponding to the inserts (a), (b), (c), and (d) are described in Table IV.

FIG. 35. A selection of cross sections where a narrow structure at $M_X=1136$ MeV was observed. The experimental conditions corresponding to the inserts (a), (b), (c), and (d) are described in Table V.

FIG. 36. A selection of cross sections where a narrow structure at $M_{p\pi}=1173$ MeV was observed. The experimental conditions corresponding to the inserts (a), (b), (c), and (d) are described in Table VI.

FIG. 37. A selection of cross sections where a narrow structure at $M_X=1249$ MeV was observed. The experimental conditions corresponding to the inserts (a), (b), (c), and (d) are described in Table VII.

FIG. 38. A selection of cross sections where a narrow structure at $M_X=1277$ MeV was observed. The experimental conditions corresponding to the inserts (a), (b), and (c), are described in Table VIII.

FIG. 39. A selection of cross sections where a narrow structure at $M_X=1384$ MeV was observed. The experimental conditions corresponding to the inserts (a) and (b) are described in Table IX.

FIG. 40. Narrow structure baryonic masses observed in cross sections from different reactions. These reactions are described in Table X.

FIG. 41. Narrow baryonic experimental and calculated masses. Equation (1) was used (see text for more details).

FIG. 42. Narrow baryonic experimental and calculated masses. The calculation corresponds to the diquark cluster model [27].

TABLE I. A selection of five missing mass cross sections from the $\bar{d} p \rightarrow p p X$ reaction, showing narrow structures. The columns describe each insert, the mass found, the experimental width, the number of standard deviations of the structure, the incident energy, the spectrometer angle, and the cuts performed in the software analysis.

Figure 26	Mass (MeV)	width (MeV)	S.D.	T_p (GeV)	θ (MeV)	cuts on M_{pp}
(a)	1041	8.0	3.05	2.1	17^0	$1876 \leq M_{pp} \leq 1889$
(b)	1094.7	17.4	3.0	2.1	17^0	$1876 \leq M_{pp} \leq 1880$
(c)	1140.3	11.5	3.0	2.1	17^0	$1876 \leq M_{pp} \leq 1880$
(c)	1171.2	10.3	3.95	2.1	17^0	$1876 \leq M_{pp} \leq 1880$
(d)	1178.1	1.5	1.85	1.72	0^0	no cuts on M_{pp}

TABLE II. A selection of two missing mass cross sections from the $\bar{d} p \rightarrow p p X$ reaction, showing narrow structures. The columns describe each insert, the mass found, the experimental width, the number of standard deviations of this structure, the incident energy, the spectrometer angle, and the cuts performed with the software.

Figure 27	Mass (MeV)	width (MeV)	S.D.	T_p (GeV)	θ (MeV)	cuts on M_{pp}
(a)	1243.8	6.0	3.2	2.1	17^0	$1876 \leq M_{pp} \leq 1880$
(b)	1391.9	2.8	2.6	2.1	17^0	$1876 \leq M_{pp} \leq 1880$

TABLE III. The $\gamma n \rightarrow p \pi^- \pi^0$ reaction studied at MAMI [18] (see section VI.E). Cross sections of the invariant $p\pi^0+p\pi^-$ mass. A selection of cross sections where small narrow structures were extracted are presented and related to the four inserts (a), (b), (c), and (d) of Fig. 33.

Figure 33	Mass (MeV)	width (MeV)	S.D.	Energy range (GeV)
(a)	1086.5	6	3.1	$500 \leq T_\gamma \leq 600$
(a)	1128.8	4.5	3.	$500 \leq T_\gamma \leq 600$
(b)	1080.6	2.5	2.5	$700 \leq T_\gamma \leq 750$
(b)	1145.9	4.0	1.6	$700 \leq T_\gamma \leq 750$
(c)	1272.3	6.6	2.9	$700 \leq T_\gamma \leq 750$
(c)	1347.2	4.7	1.9	$700 \leq T_\gamma \leq 750$
(d)	1184	2.7	2.9	$500 \leq T_\gamma \leq 800$

TABLE IV. Excitation function of the $\gamma p \rightarrow \pi^+ n$ reaction studied at the Bonn electron synchrotron [19].

θ (degrees)	Mass (MeV)	width (MeV)	S.D.
95	1390.3	25.4	12.4
120	1336.9	8.7	6.5
120	1383.1	24.3	15.3
135	1345.0	11.3	7.7
135	1383.2	17.5	12.2
180	1386.6	19.1	4.7

TABLE V. Cross sections of the invariant $M_{p\pi^+}$ mass from the $p p \rightarrow p \pi^+ X$ reaction. The extracted values are given and are related to the four inserts of Fig. 35, justifying the extraction of a narrow structure at $M=1136$ MeV.

Figure 35	Mass (MeV)	width (MeV)	S.D.	T_p (GeV)	θ
(a)	1143	7.9	6.3	2.1	0.7^0
(b)	1133.7	10.6	11	2.1	3^0
(c)	1130.4	11.3	4.9	1.805	3.7^0
(d)	1130.8	8.6	3.6	1.805	9^0

TABLE VI. Cross sections of the invariant $M_{p\pi^+}$ mass from the $p p \rightarrow p \pi^+ X$ reaction. The extracted values are given and are related to the four inserts of Fig. 36 justifying the extraction of a narrow structure at $M=1173$ MeV.

Figure 36	Mass (MeV)	width (MeV)	S.D.	T_p (GeV)	θ
(a)	1173.4	8.1	7	1.52	13^0
(b)	1166.9	4.2	3.4	1.52	0^0
(c)	1170.4	5.9	2.8	1.52	2^0
(d)	1176.6	7.8	3.1	1.805	6.7^0

TABLE VII. Cross sections of the invariant $M_{p\pi^+}$ mass from the $p p \rightarrow p \pi^+ X$ reaction. The extracted values are given and are related to the four inserts of Fig. 37 justifying the extraction of a narrow structure at $M=1249$ MeV.

Figure 37	Mass (MeV)	width (MeV)	S.D.	T_p (GeV)	θ
(a)	1247.3	13.9	10.4	1.52	0^0
(b)	1251.1	9.5	8.3	1.52	2^0
(c)	1250.7	10.8	7.3	1.52	5^0
(d)	1250.2	5.0	3.0	1.52	9^0

TABLE VIII. Cross sections of the invariant $M_{p\pi^+}$ mass and of the missing mass M_X from the $p p \rightarrow p \pi^+ X$ reaction. The extracted values are given and are related to the three inserts of Fig. 38 justifying the extraction of a narrow structure at $M=1277$ MeV. Insert (d) illustrates the observation of a structure close to $M=1330$ MeV.

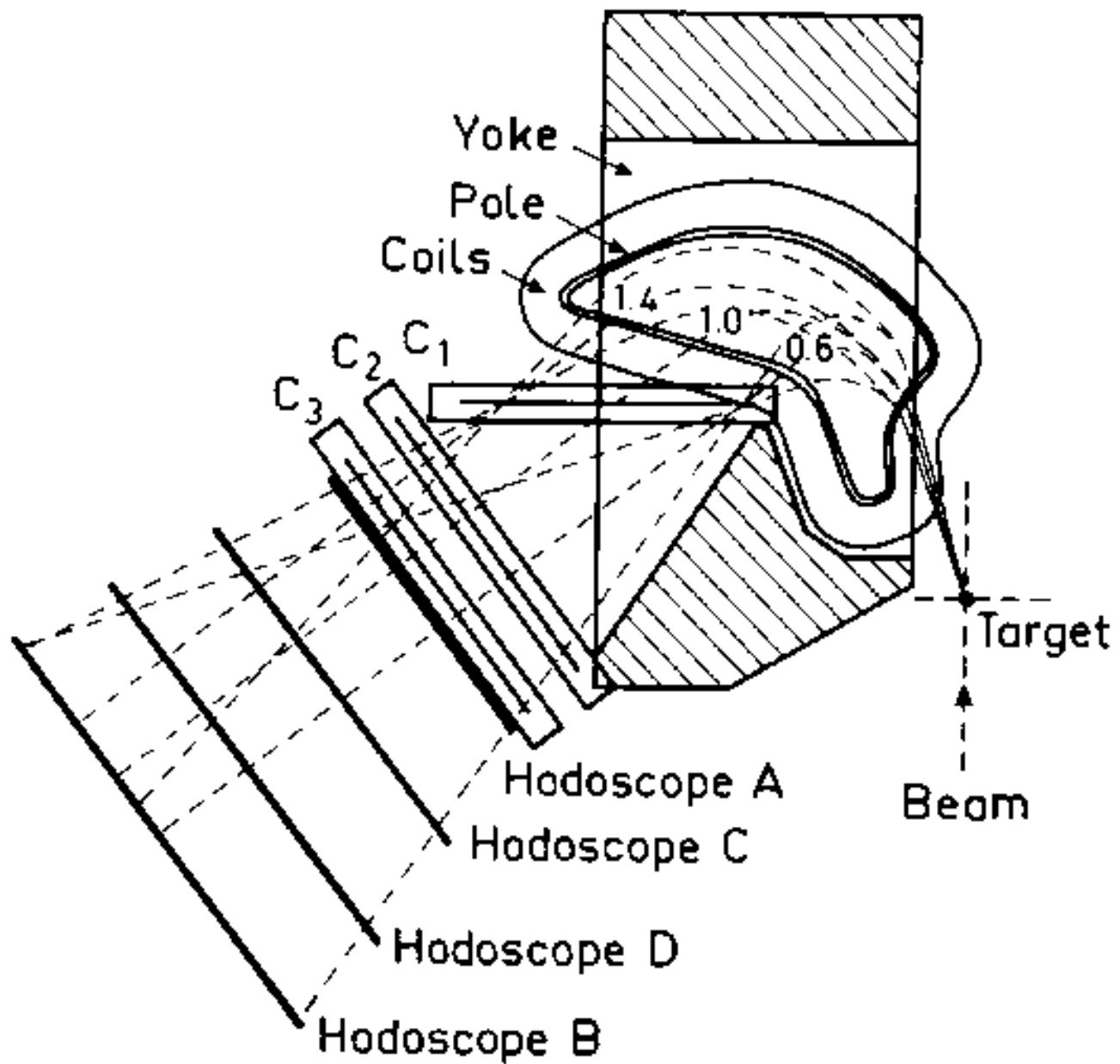
Figure 38	Mass (MeV)	width (MeV)	S.D.	T_p (GeV)	θ	observable
(a)	1282.8	8.3	3.5	1.805	6.7^0	$M_{p\pi^+}$
(b)	1270.0	8.1	3.2	1.805	3.7^0	M_X
(c)	1277.0	6.6	2.4	2.1	9^0	$M_{p\pi^+}$
(d)	1327.1	5.3	2.7	2.1	9^0	M_X

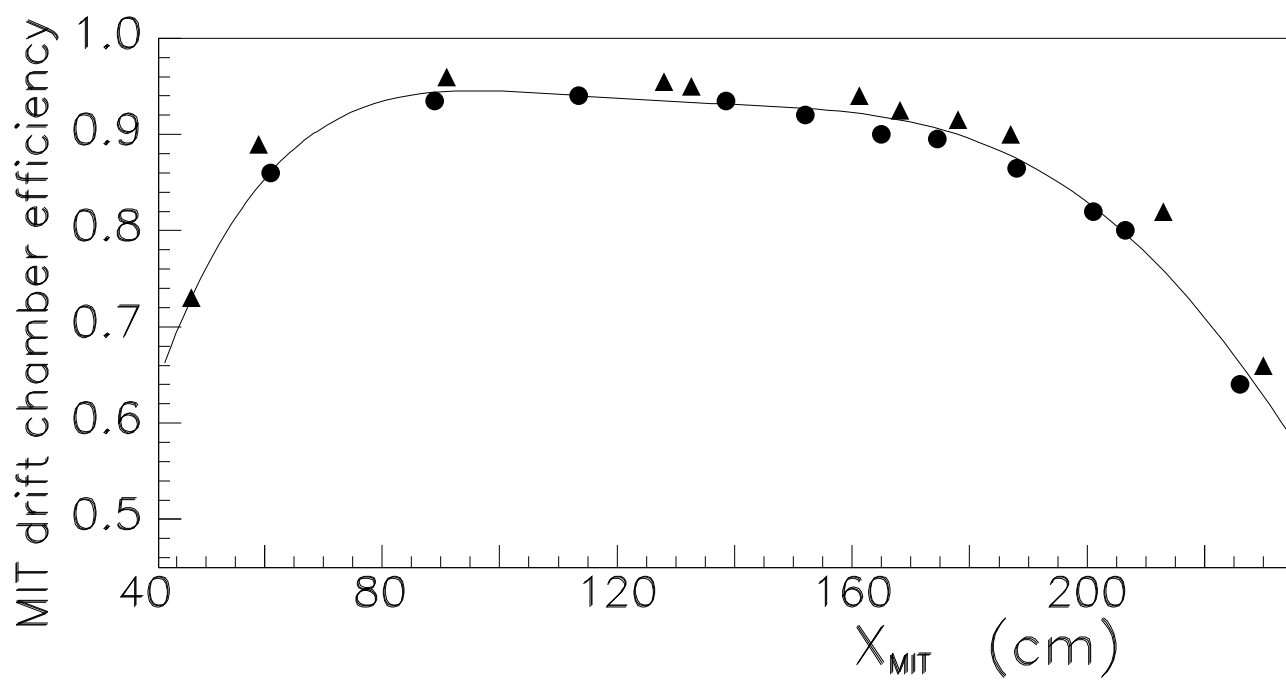
TABLE IX. Cross sections of the missing mass M_X from the $p p \rightarrow p \pi^+ X$ and $d p \rightarrow p p X$ reactions. The extracted values are given and are related to the two inserts of Fig. 39 justifying the possibility of the extraction of a narrow structure close to $M=1384$ MeV.

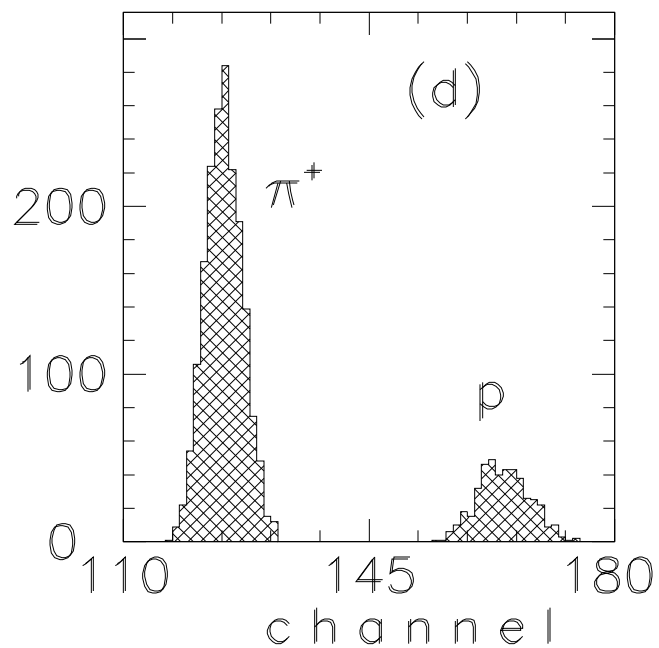
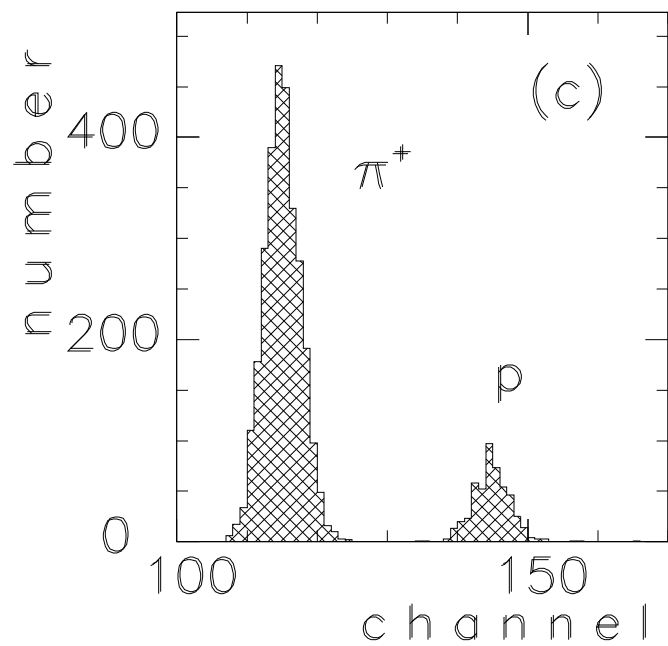
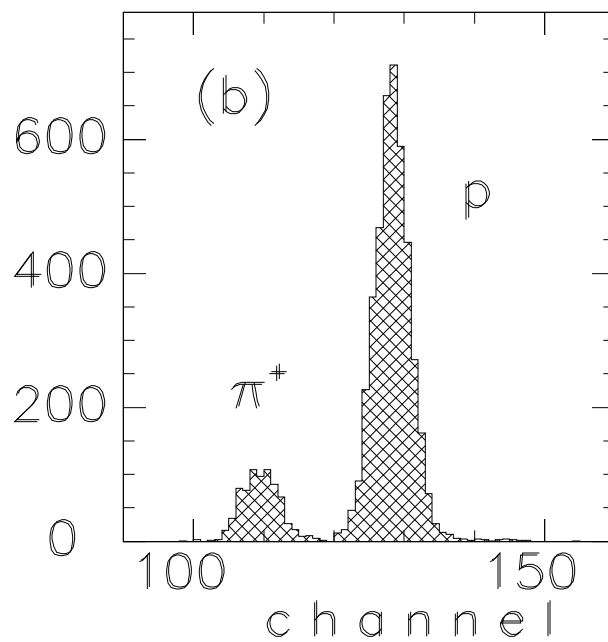
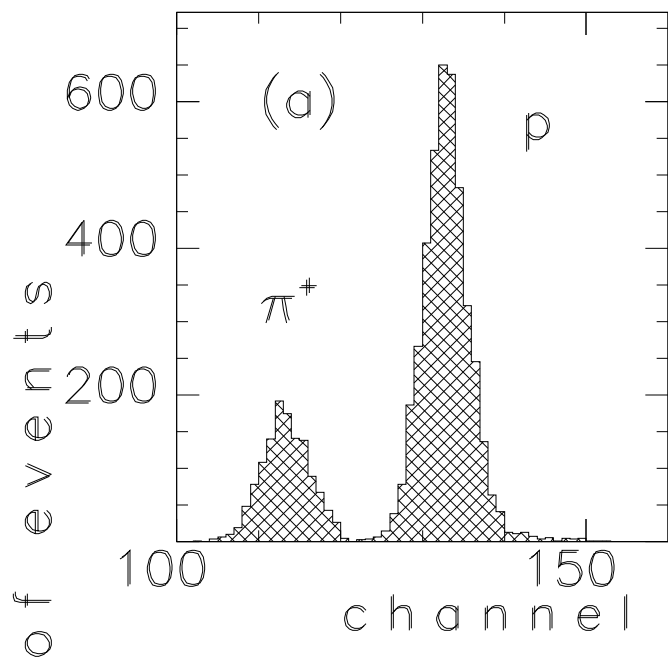
Figure 39	Mass (MeV)	reaction	width (MeV)	S.D.	T_p (GeV)	θ
(a)	1375.3	$p p \rightarrow p \pi^+ X$	12.1	3.7	1.805	6.7°
(b)	1391.9	$d p \rightarrow p p X$	2.8	2.6	2.1	17°

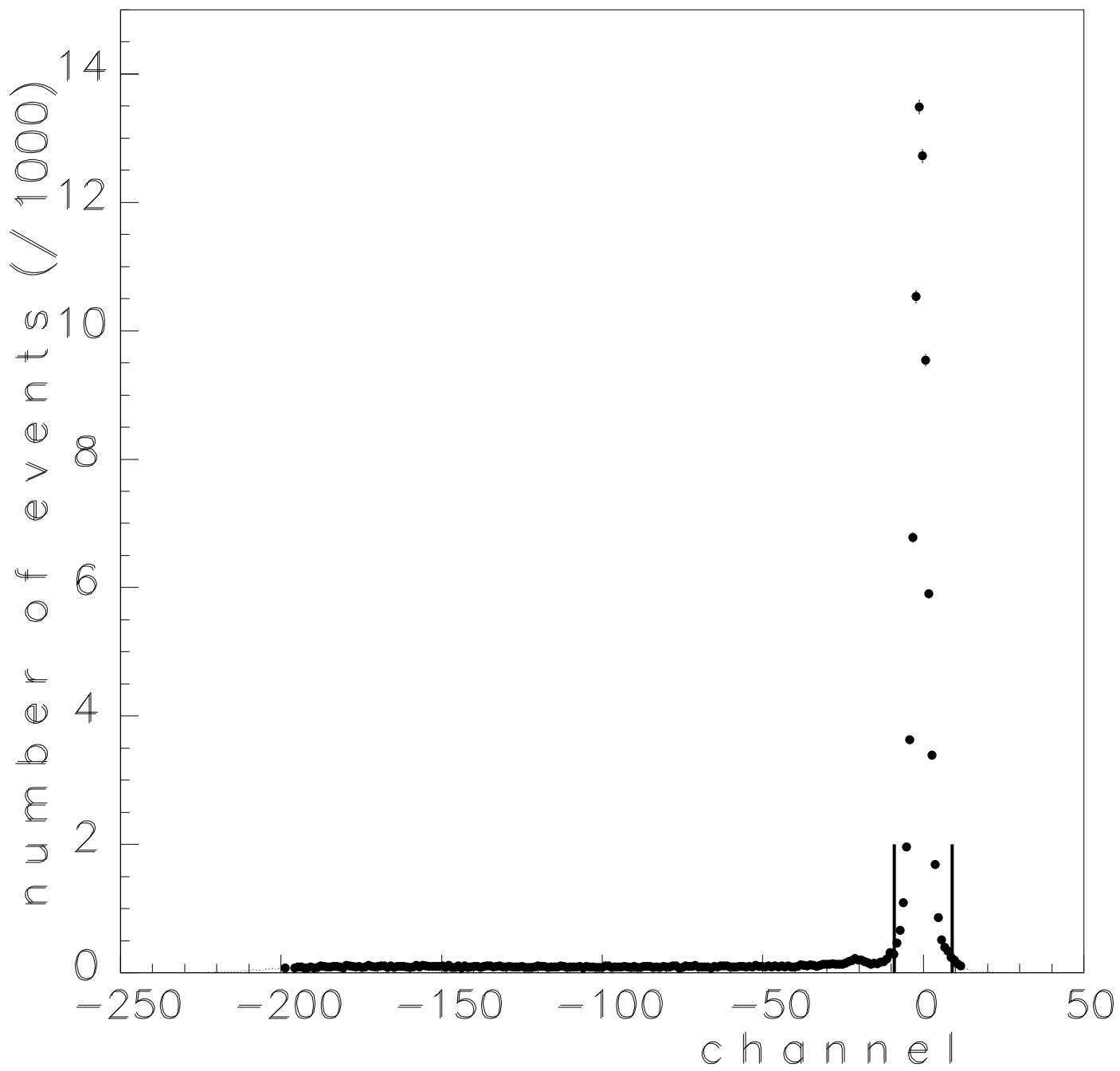
TABLE X. Experiments whose results are displayed in Fig. 40. The last column (j) of Fig. 40 shows also one mass ($M=1136$ MeV) extracted from the $np \rightarrow pX$ experiment from LAMPF [13].

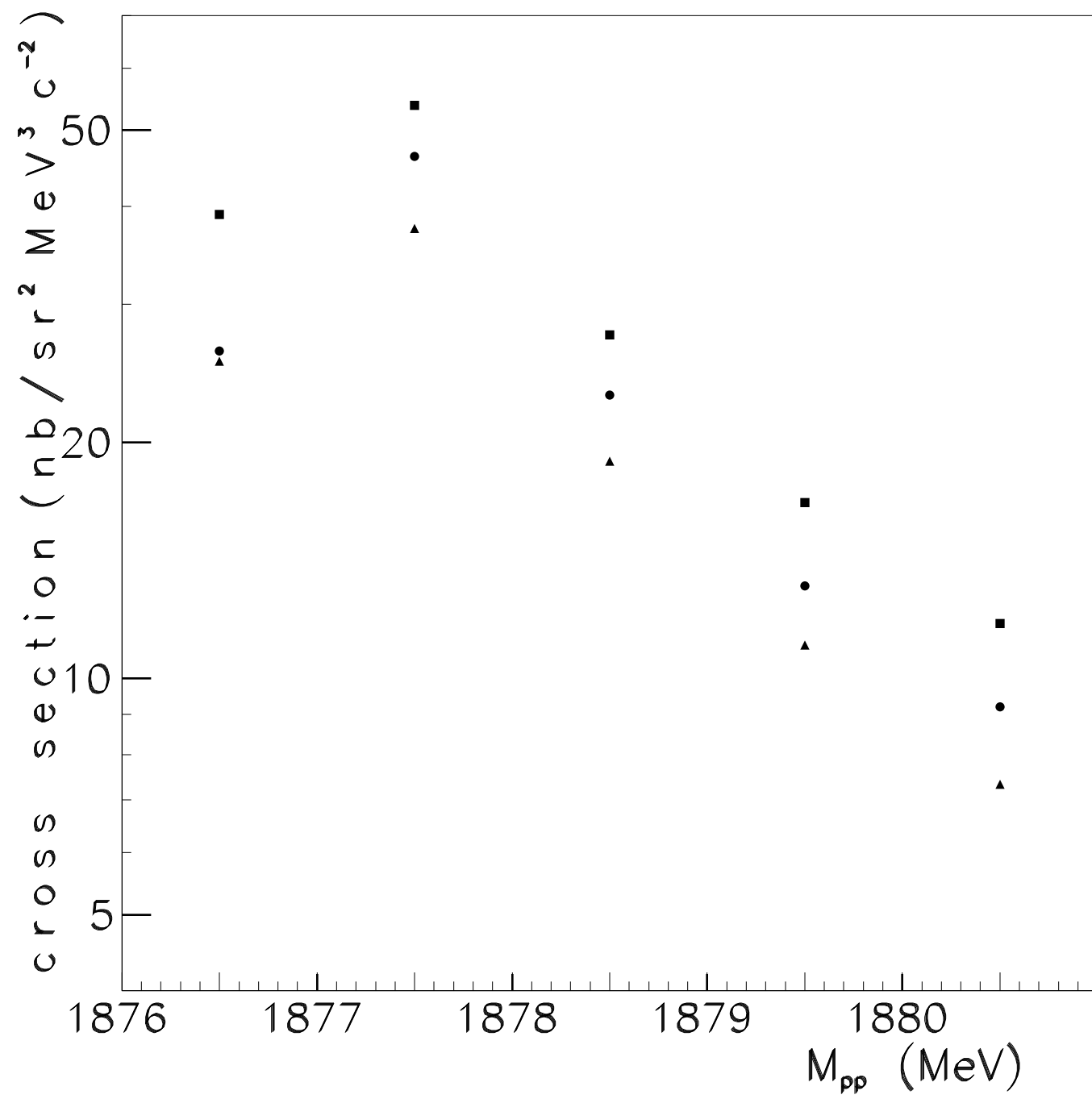
column	reaction	variable	incident energy (MeV)	reference
(a)	$pp \rightarrow \pi^+ pX$	M_X	1520	this work
(b)	$pp \rightarrow \pi^+ pX$	M_X	1805	this work
(c)	$pp \rightarrow \pi^+ pX$	M_X	2100	this work
(d)	$pp \rightarrow \pi^+ pX$	$M_{p\pi}$	1520	this work
(e)	$pp \rightarrow \pi^+ pX$	$M_{p\pi}$	1805	this work
(f)	$pp \rightarrow \pi^+ pX$	$M_{p\pi}$	2100	this work
(g)	$dp \rightarrow ppX$	M_X	1722	this work
(h)	$dp \rightarrow ppX$	M_X	2100	this work
(i)	$\gamma n \rightarrow p\pi^+\pi^0$	$M_{p\pi}$	500-800	[18] (MAMI)
(j)	$\gamma p \rightarrow \pi^+ n$	W_{CM}	300-2000	[19] (Bonn)

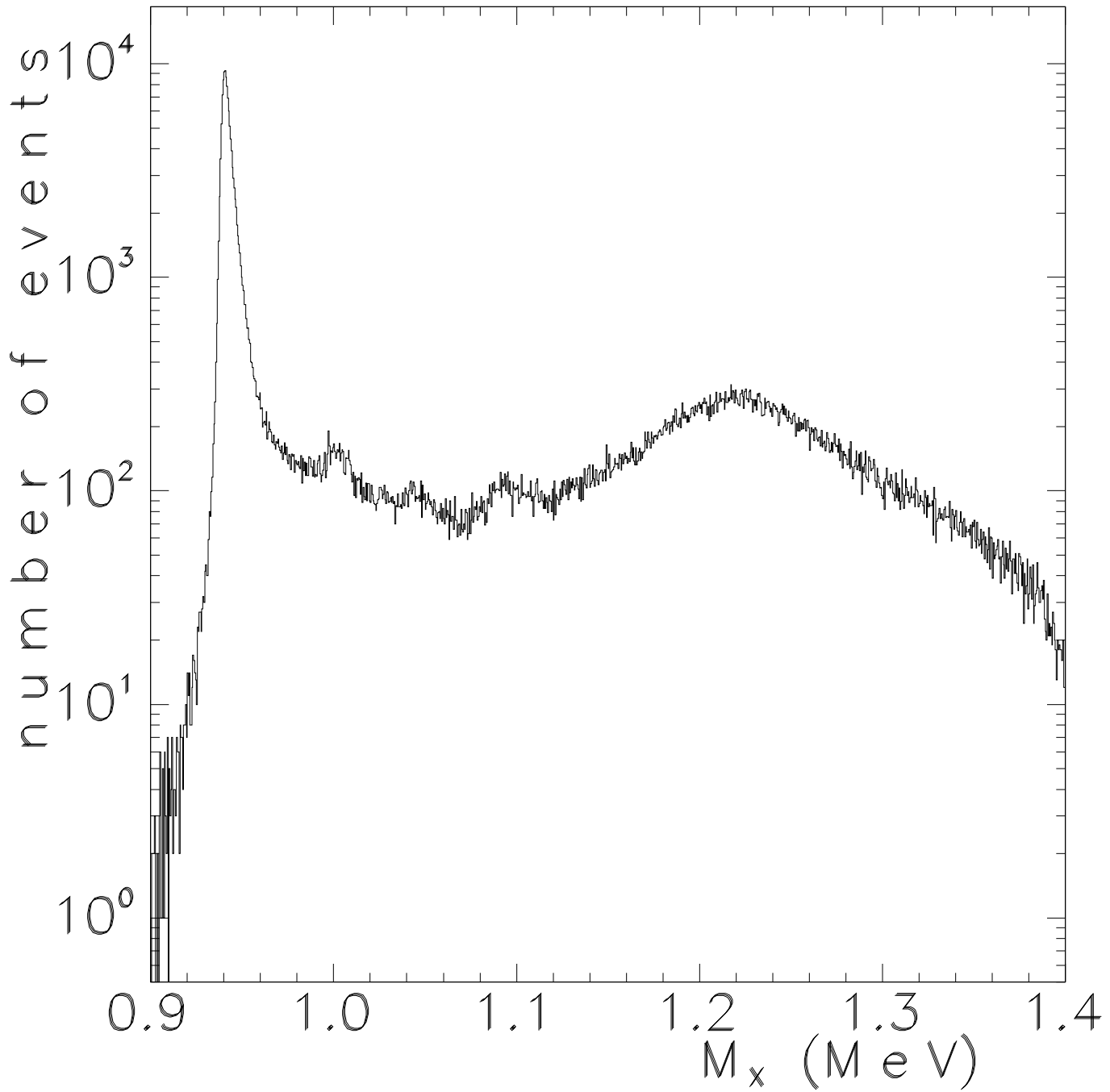


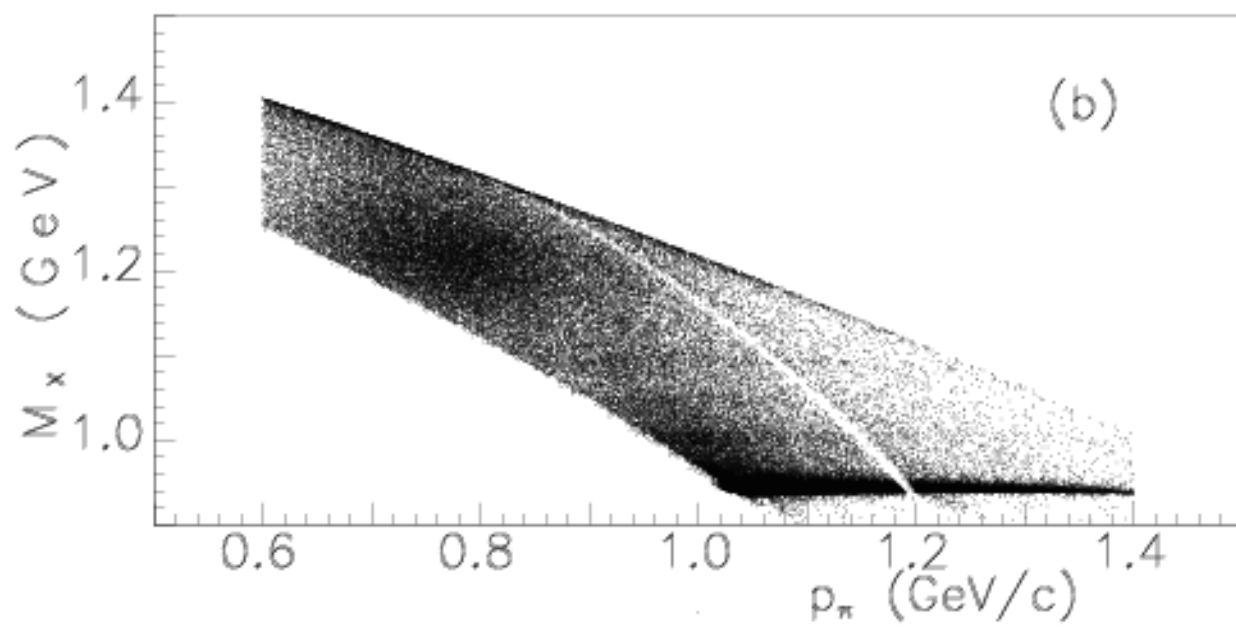
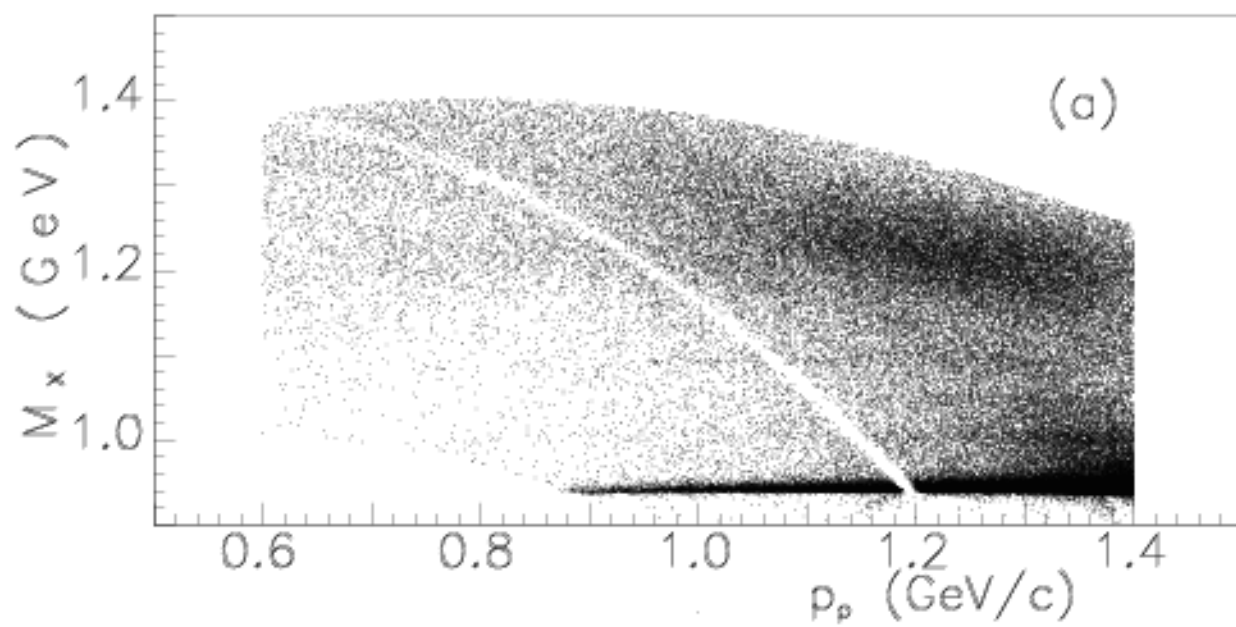


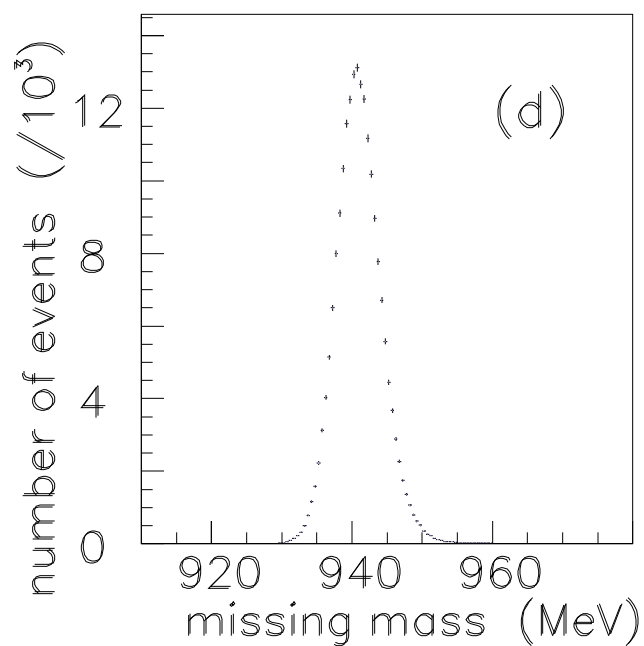
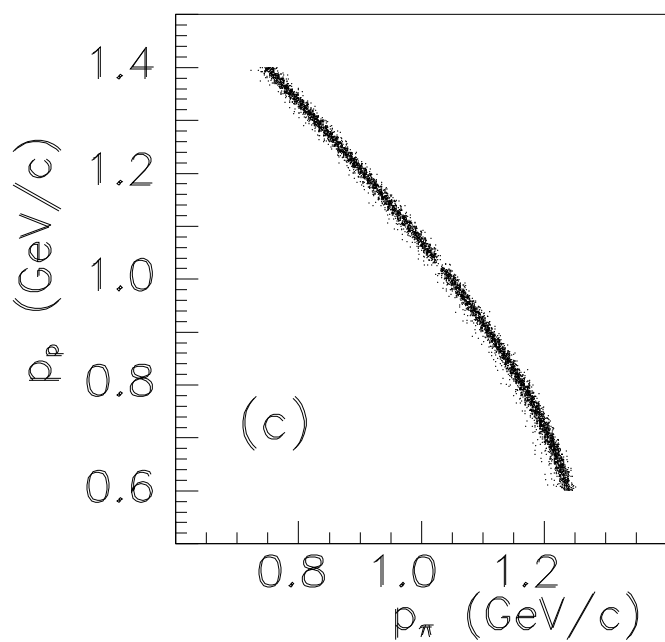
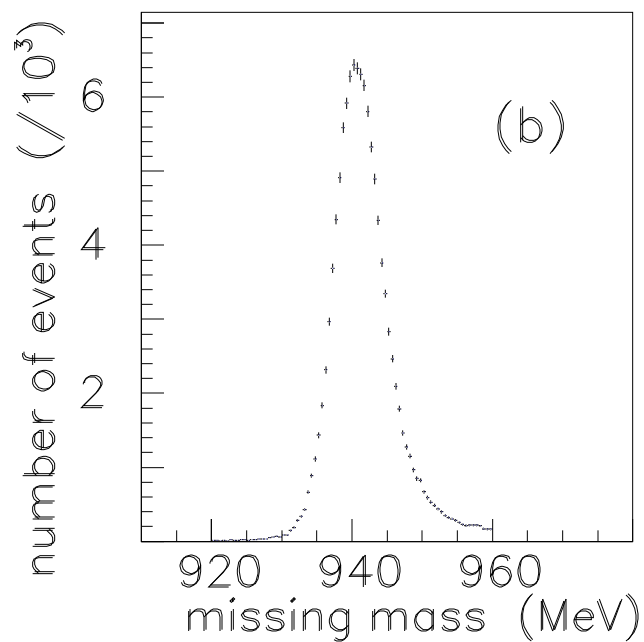
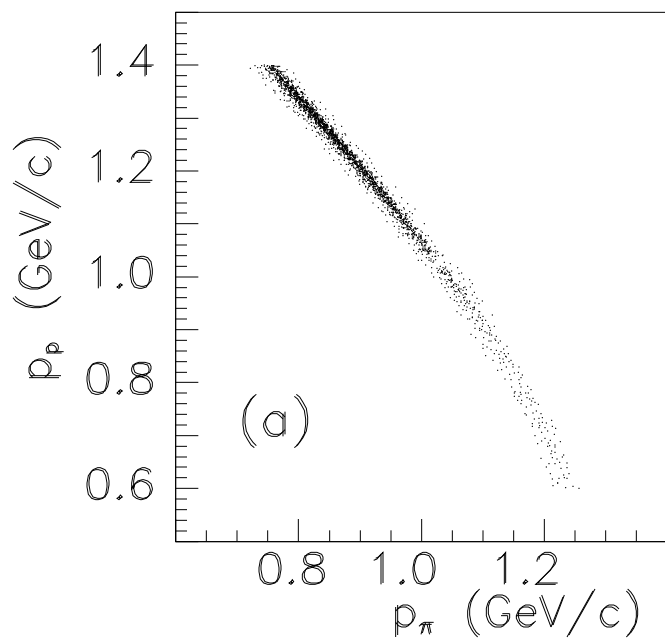


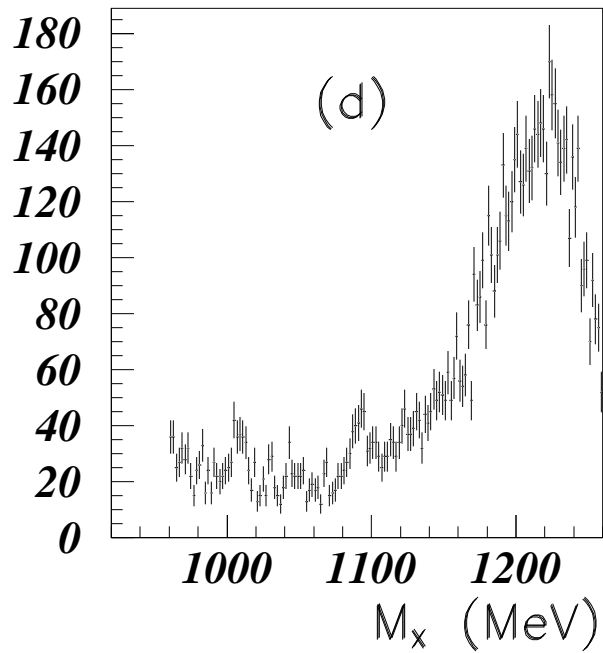
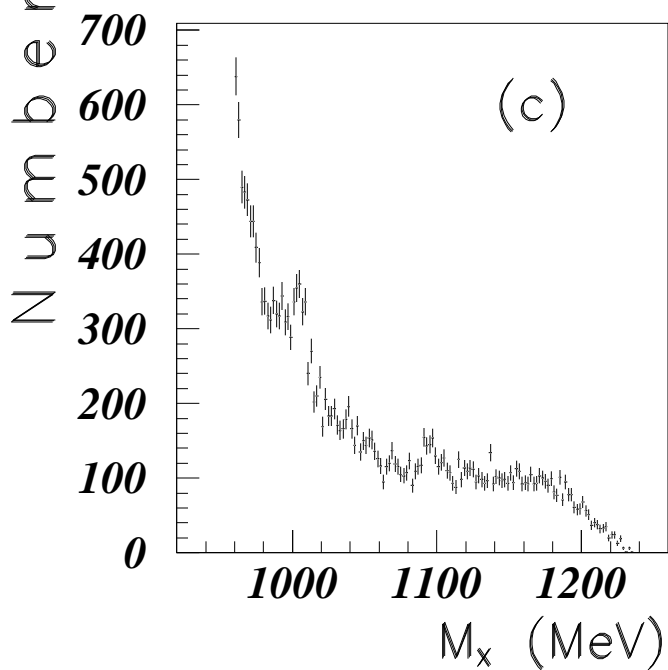
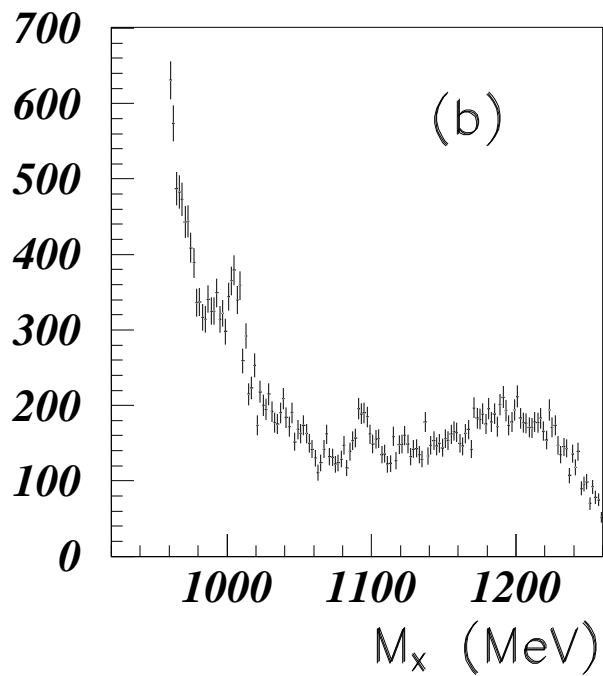
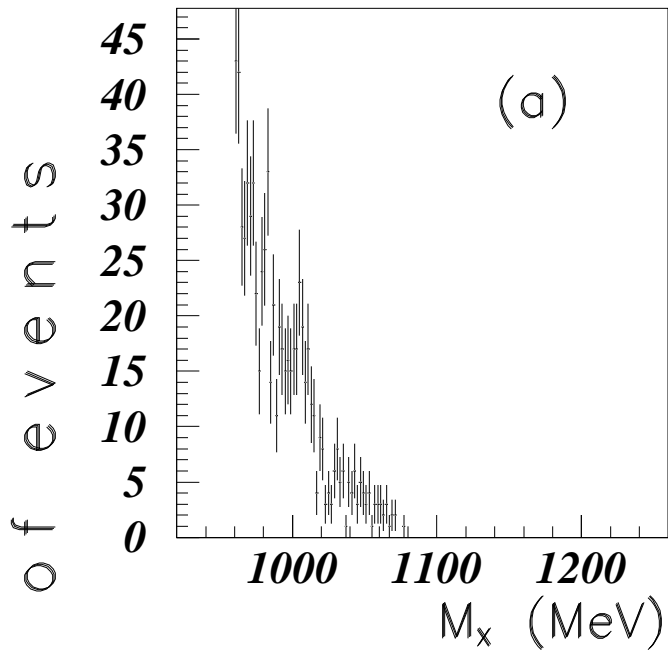


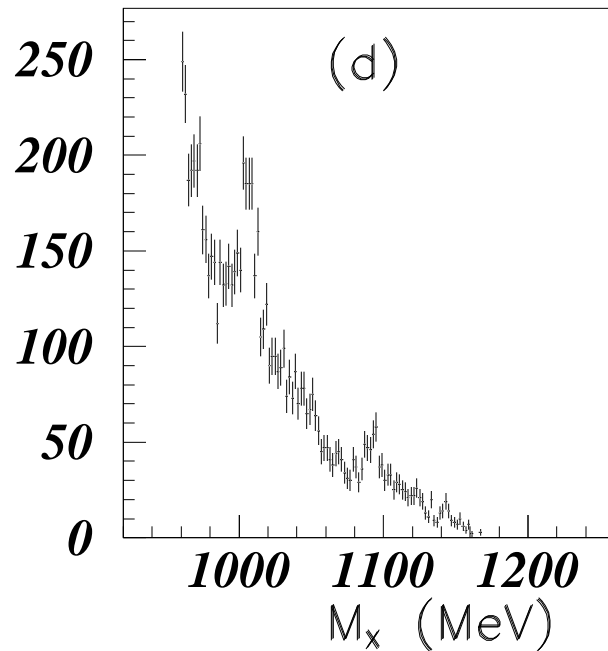
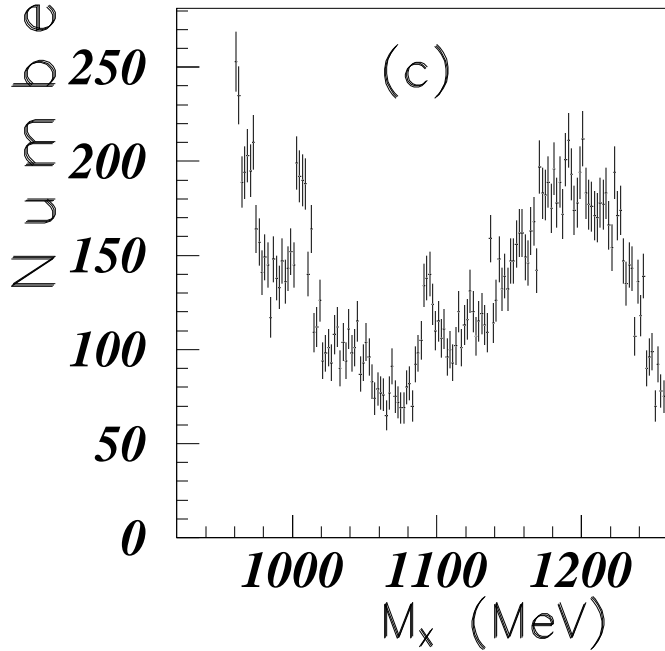
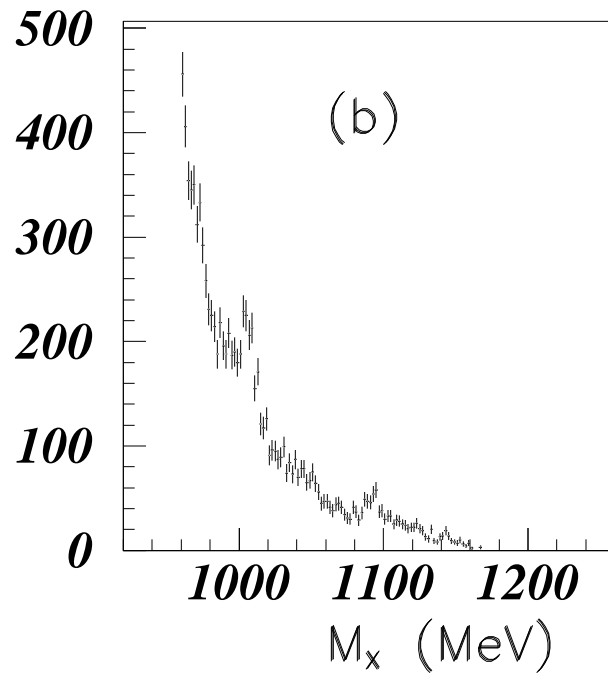
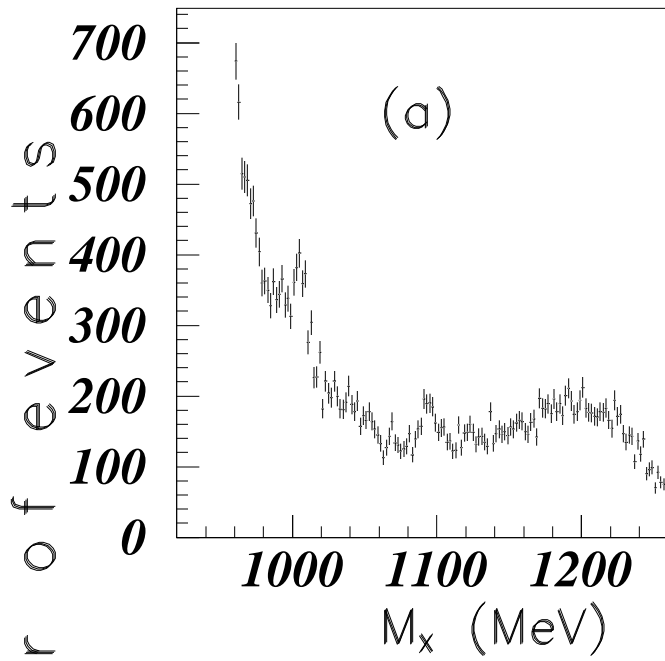


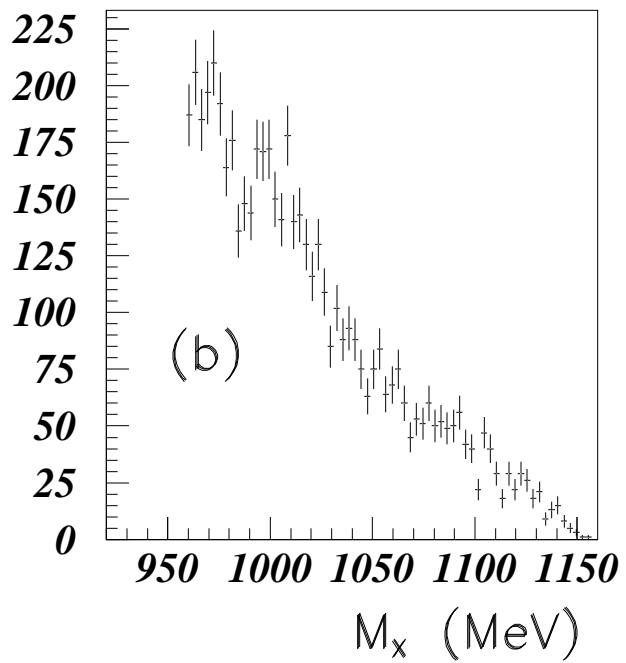
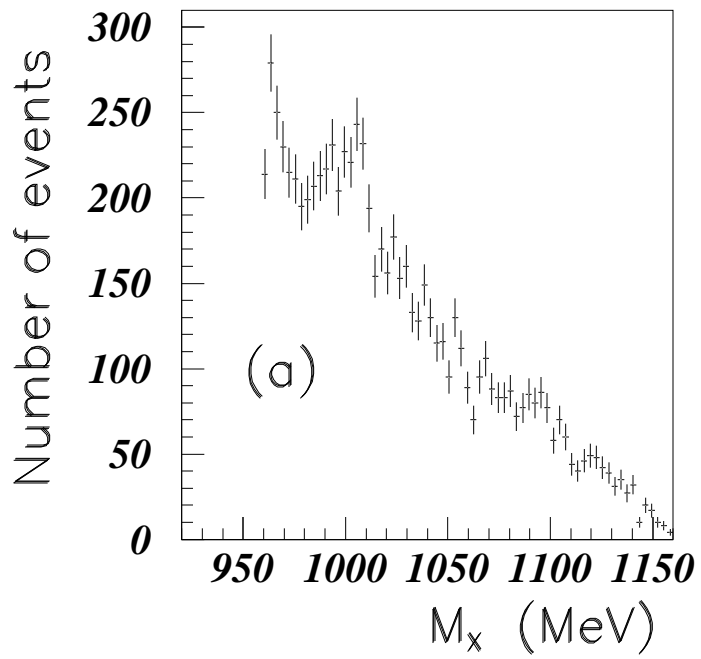


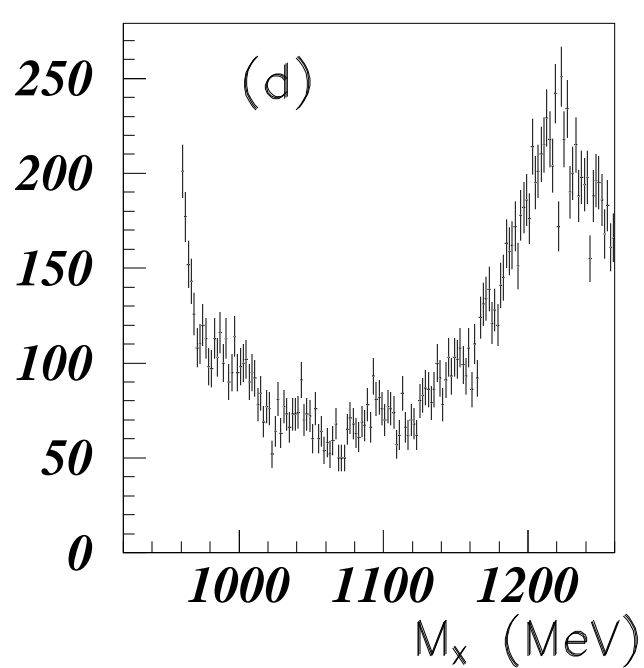
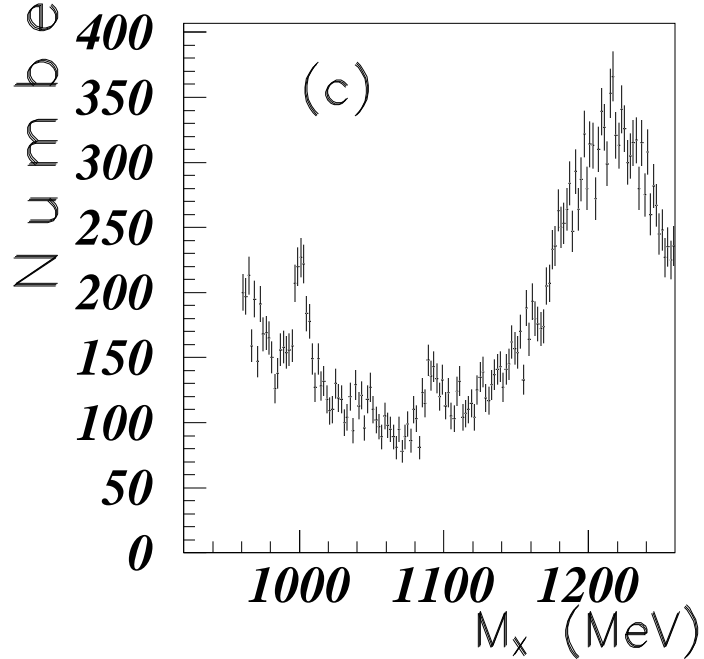
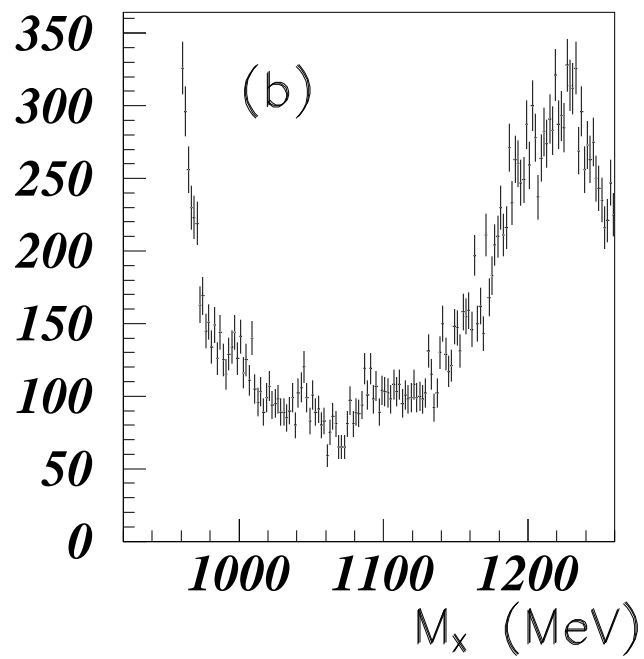
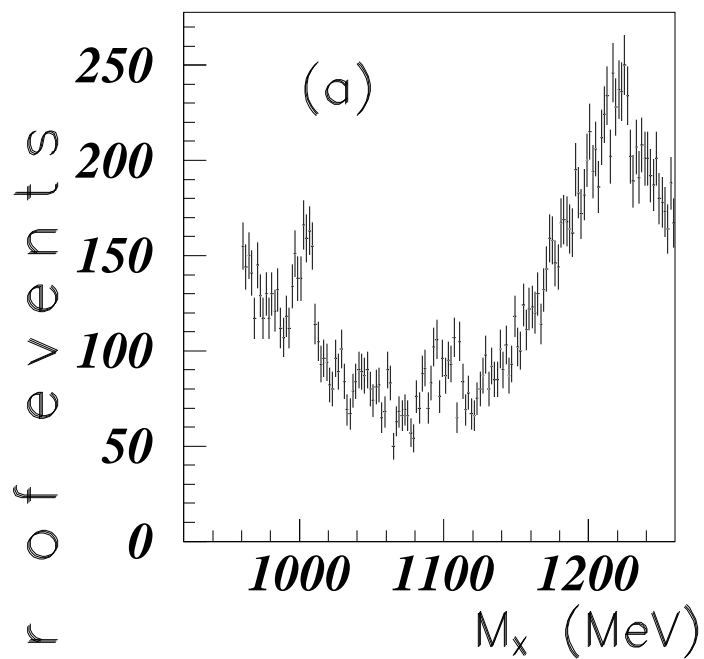


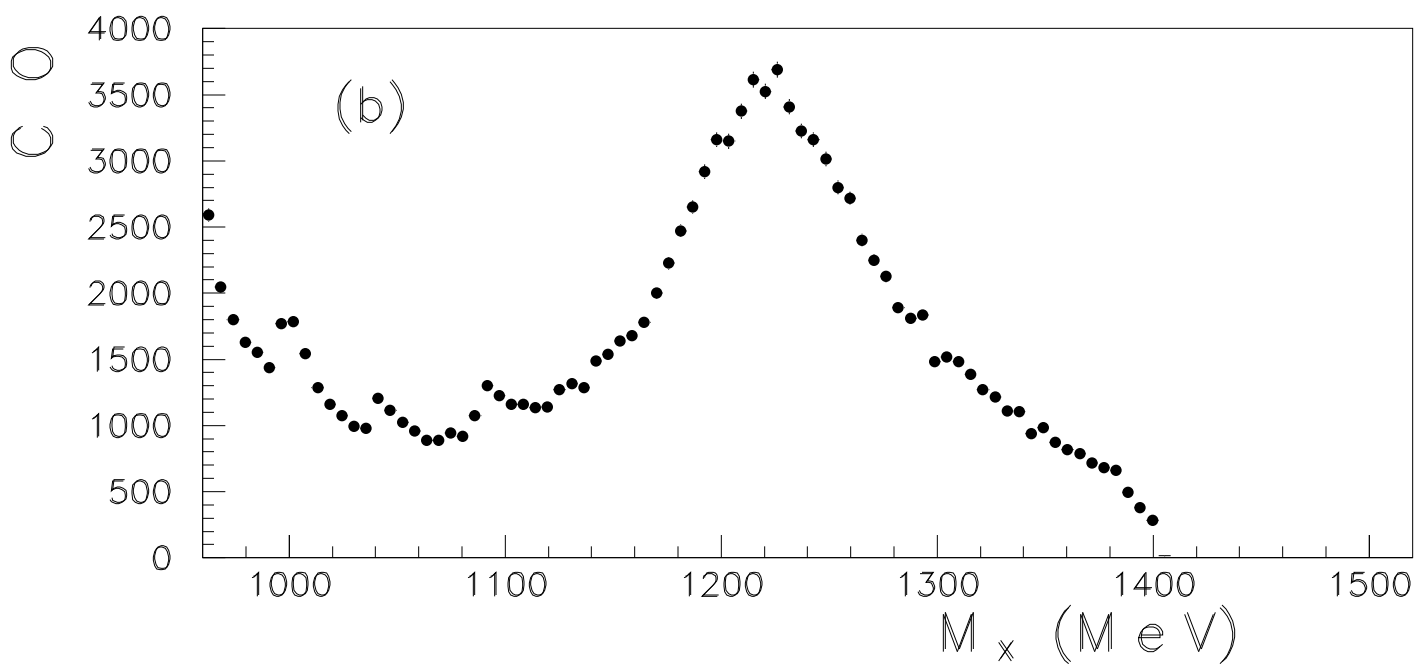
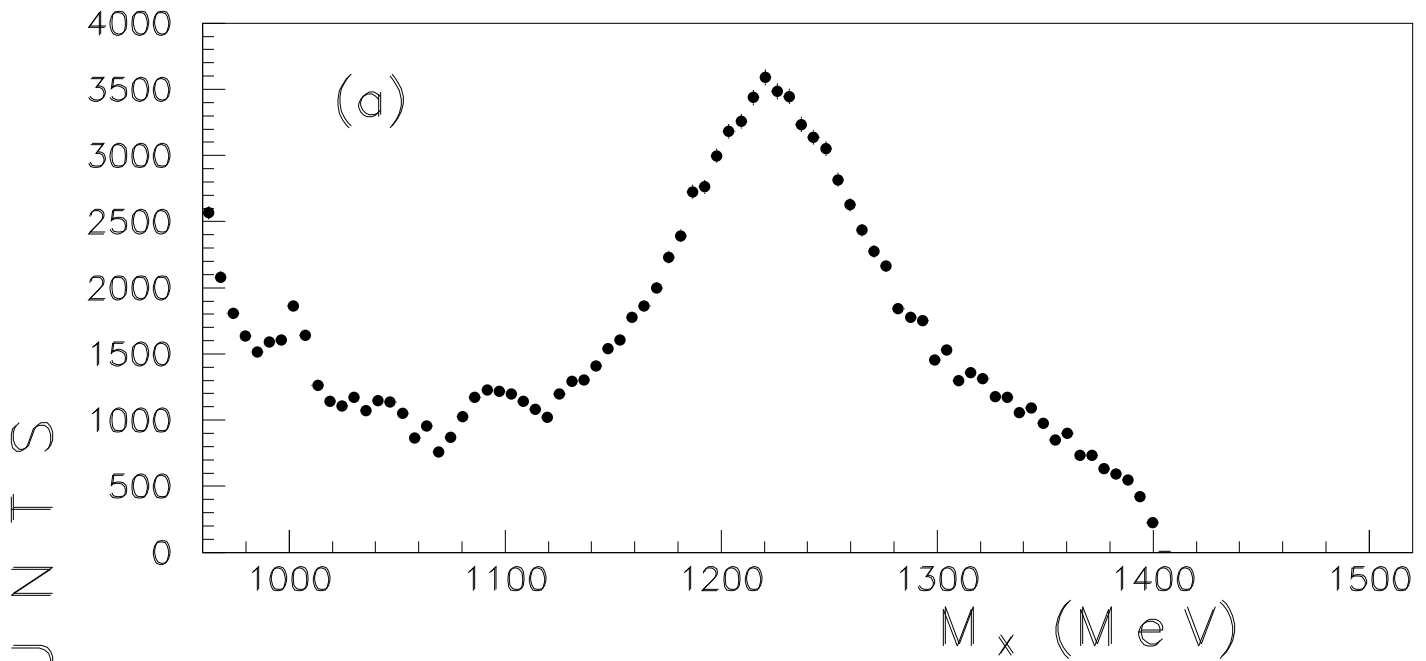


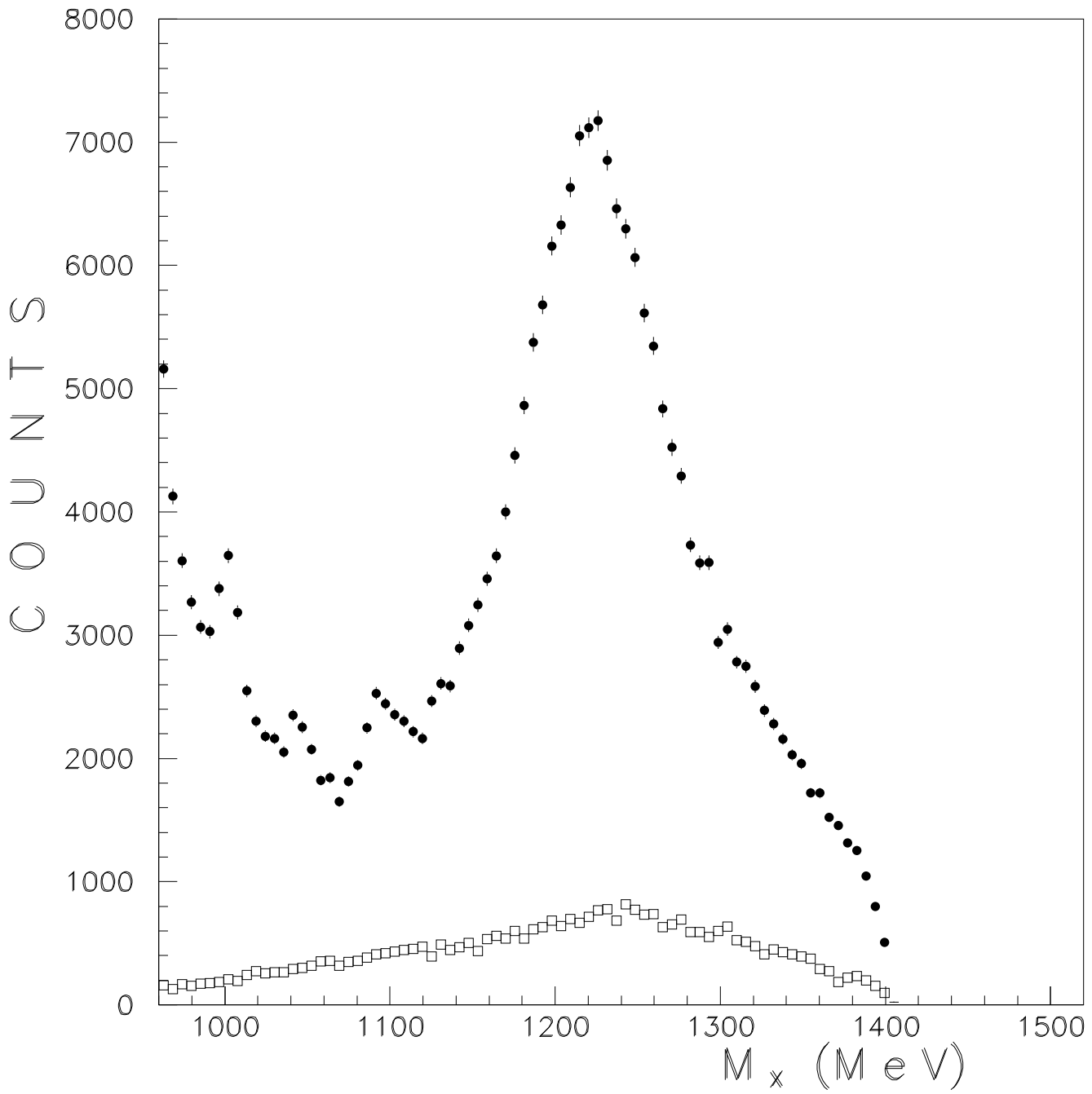


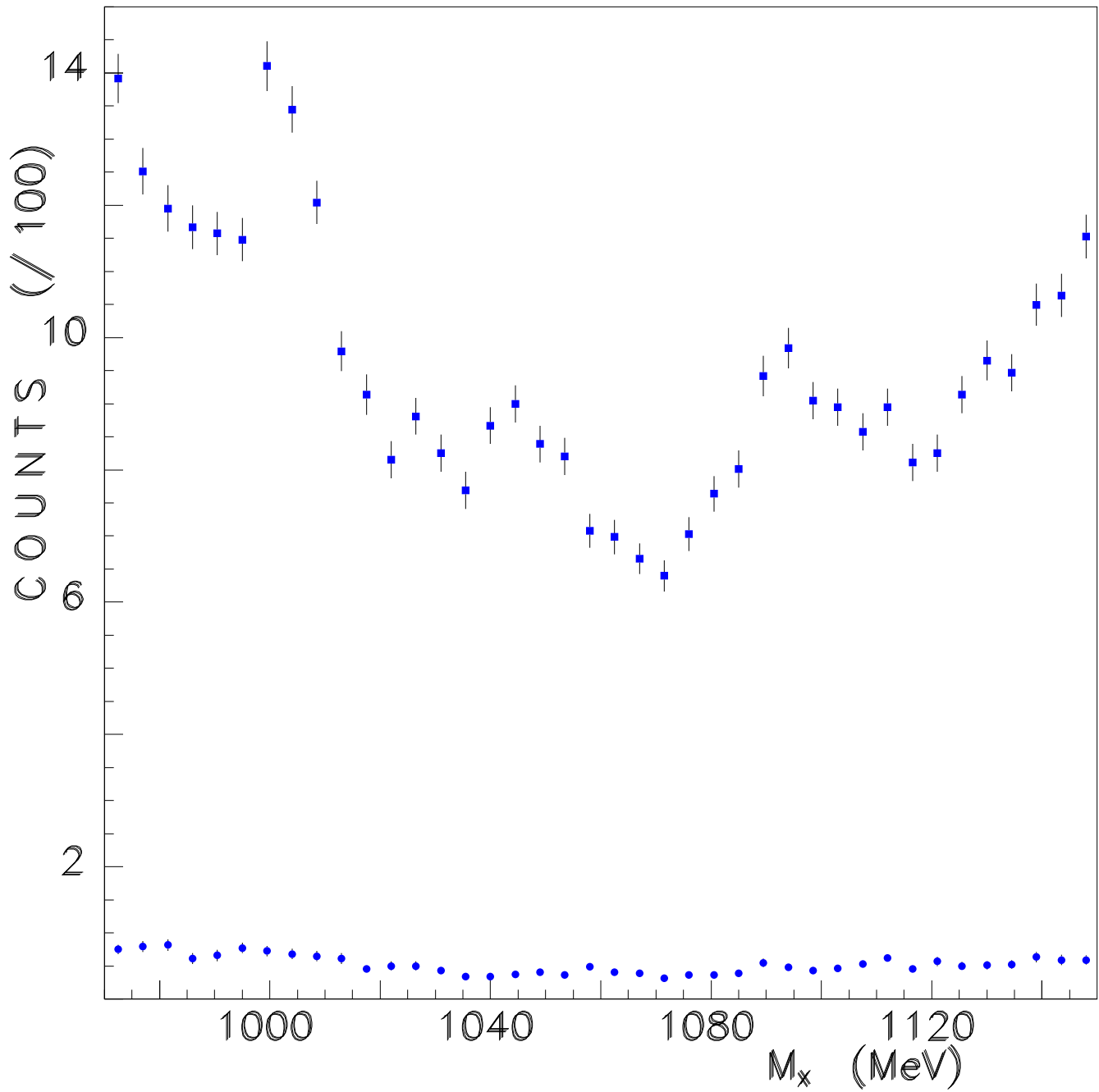


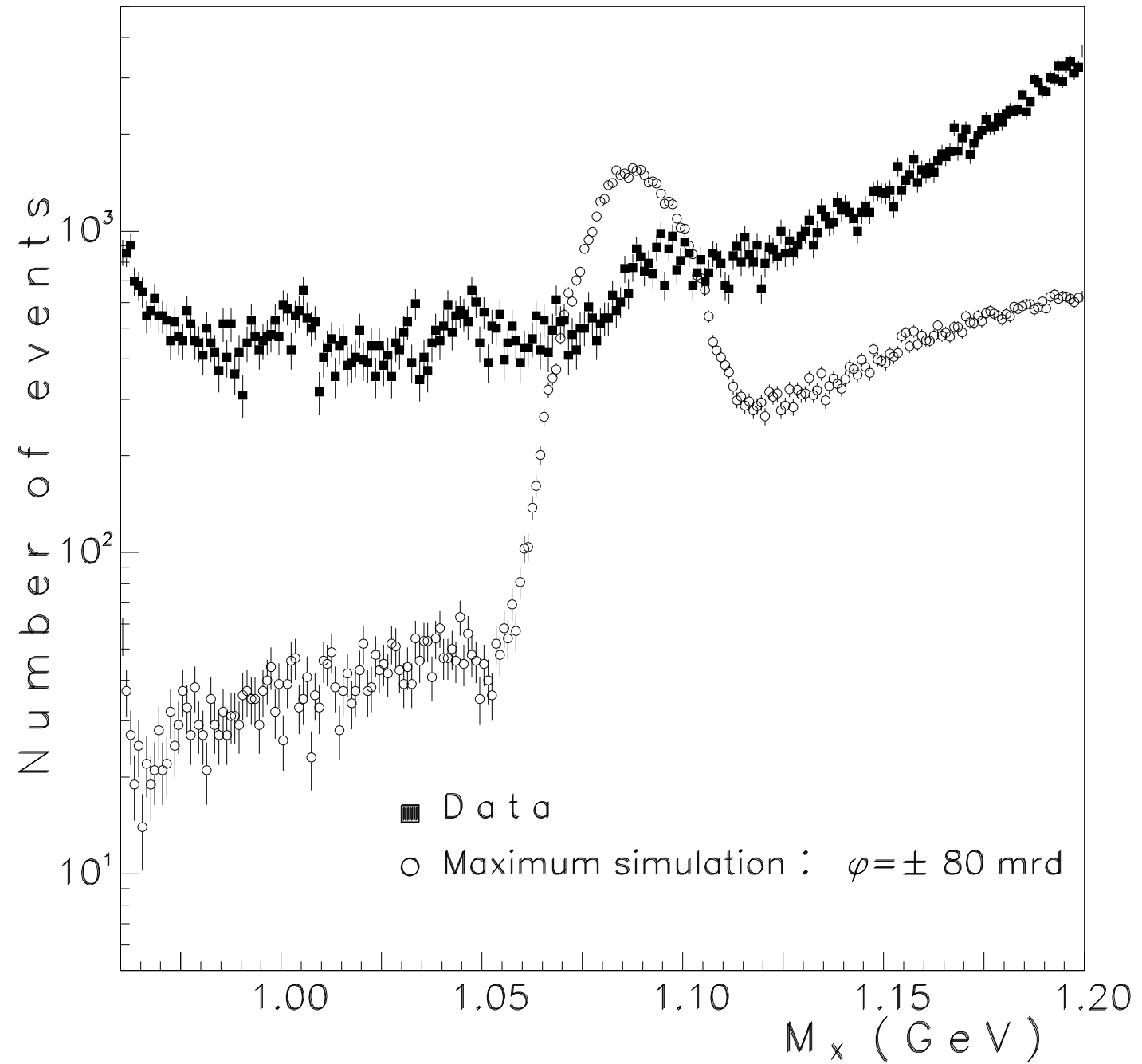


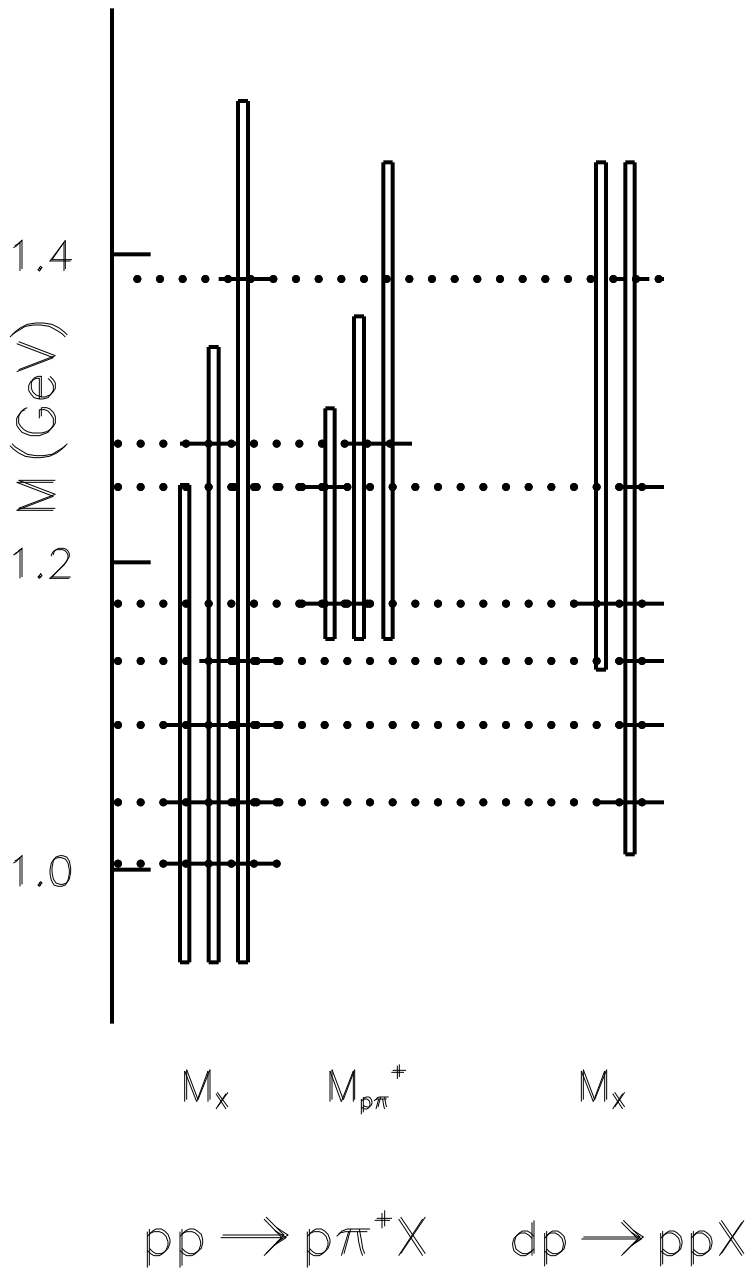


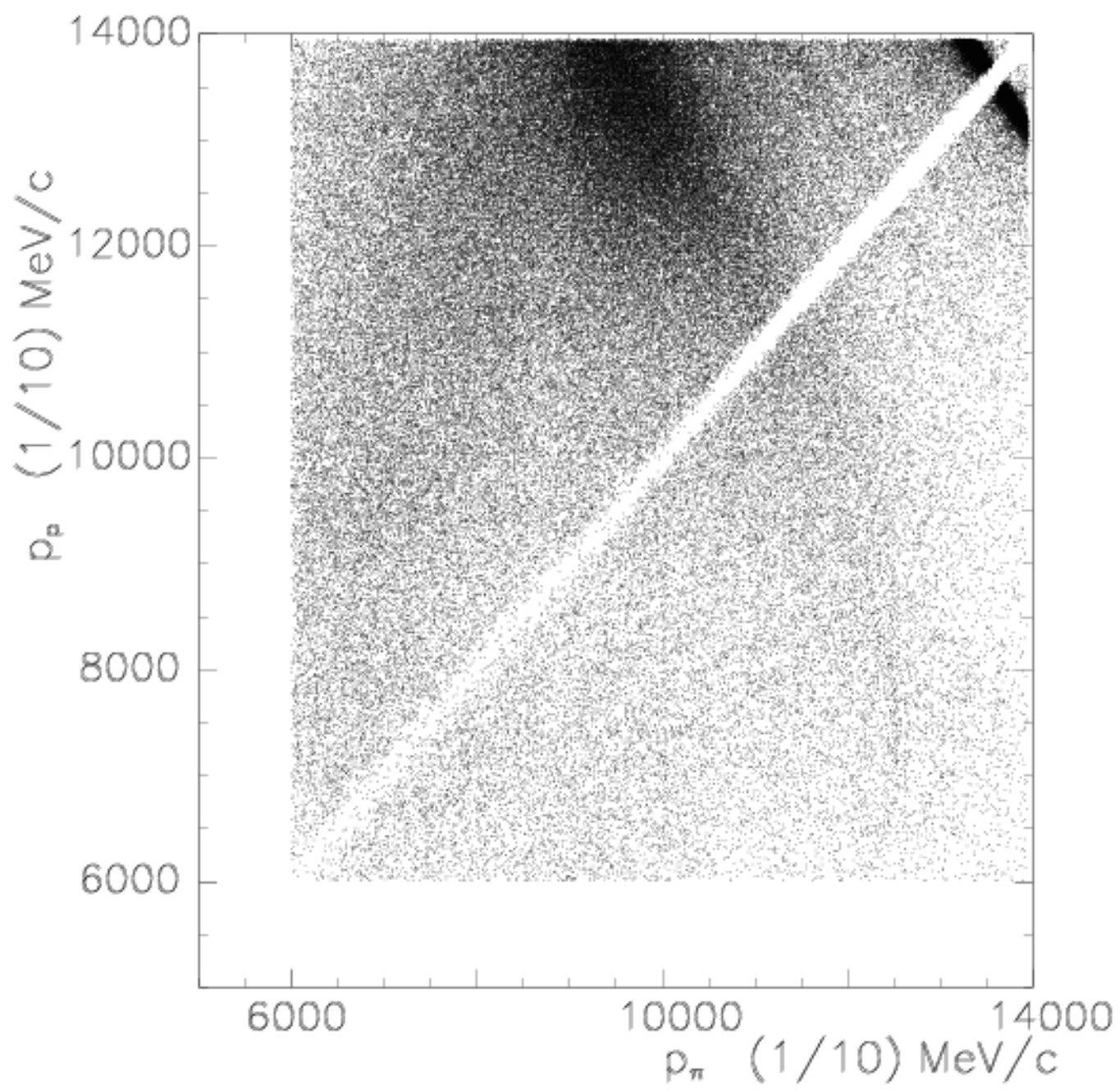


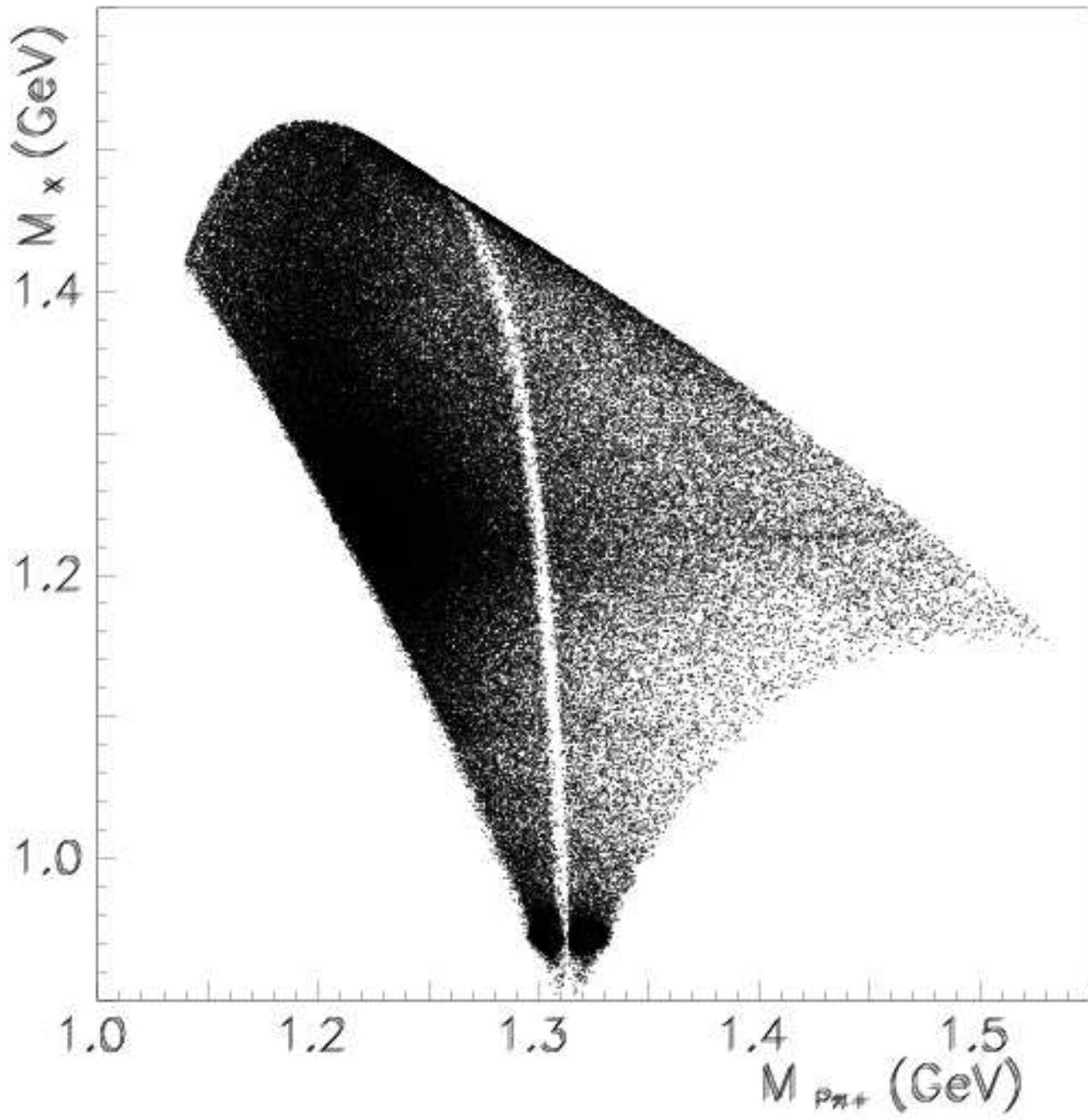


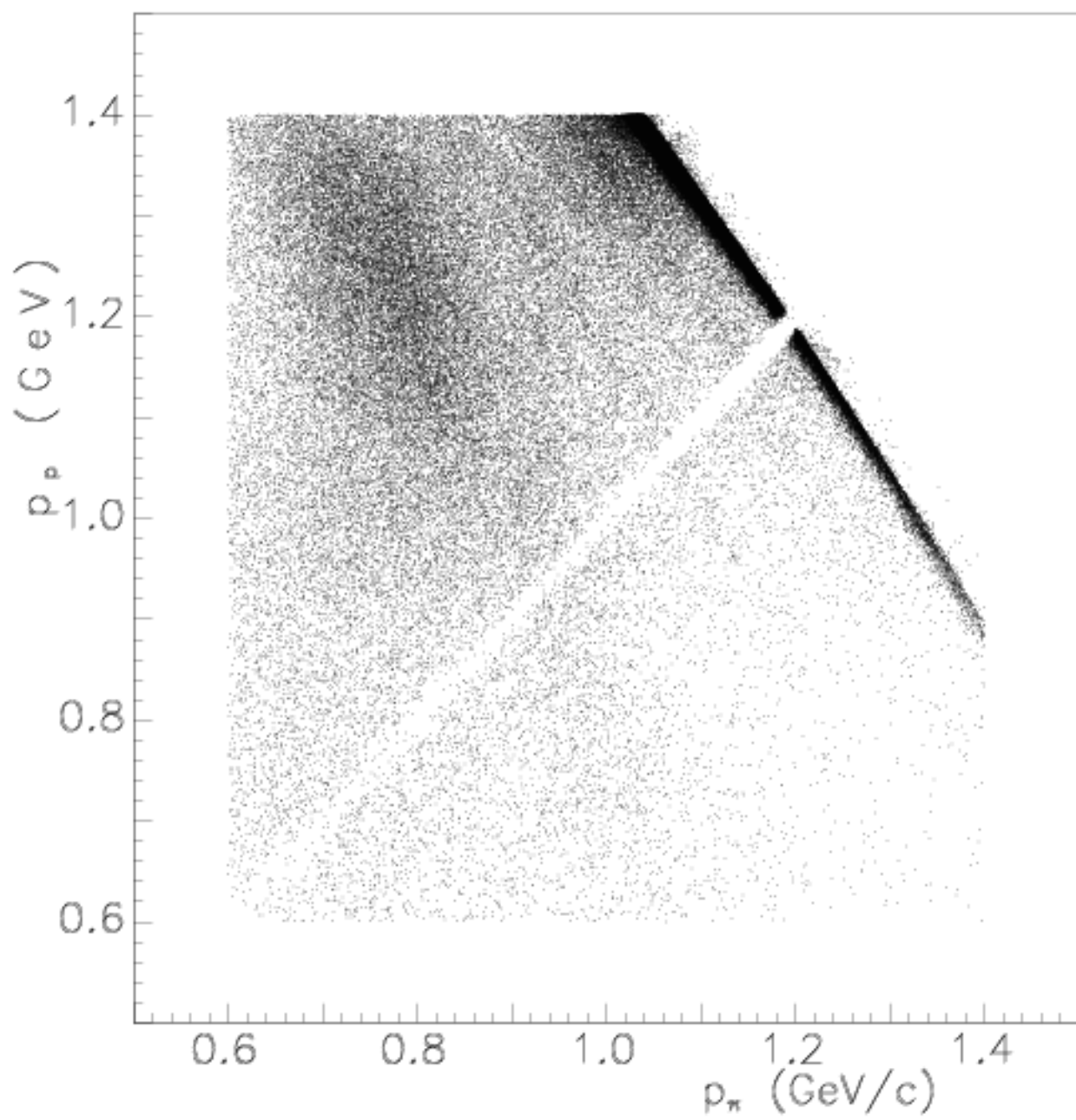


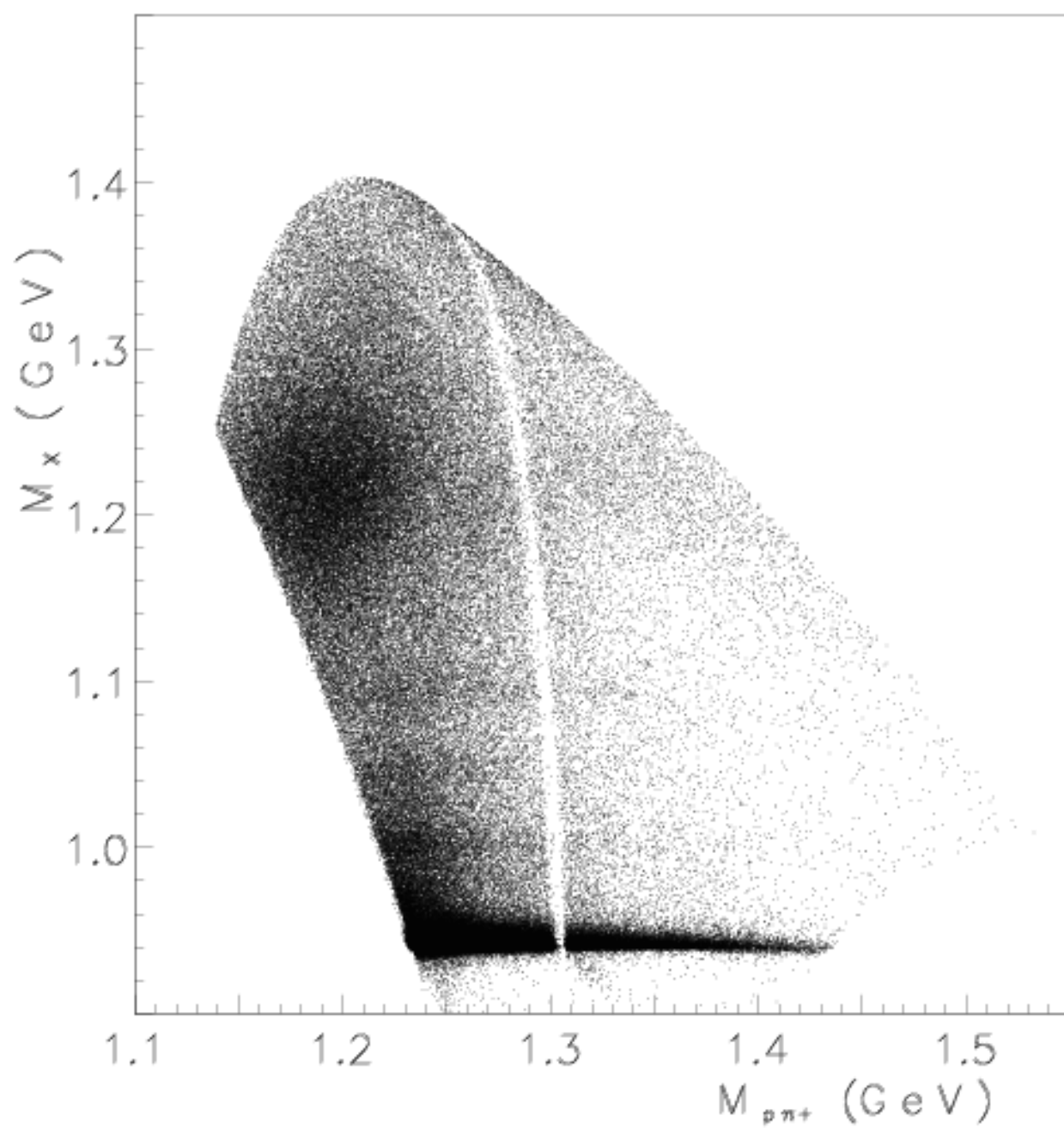


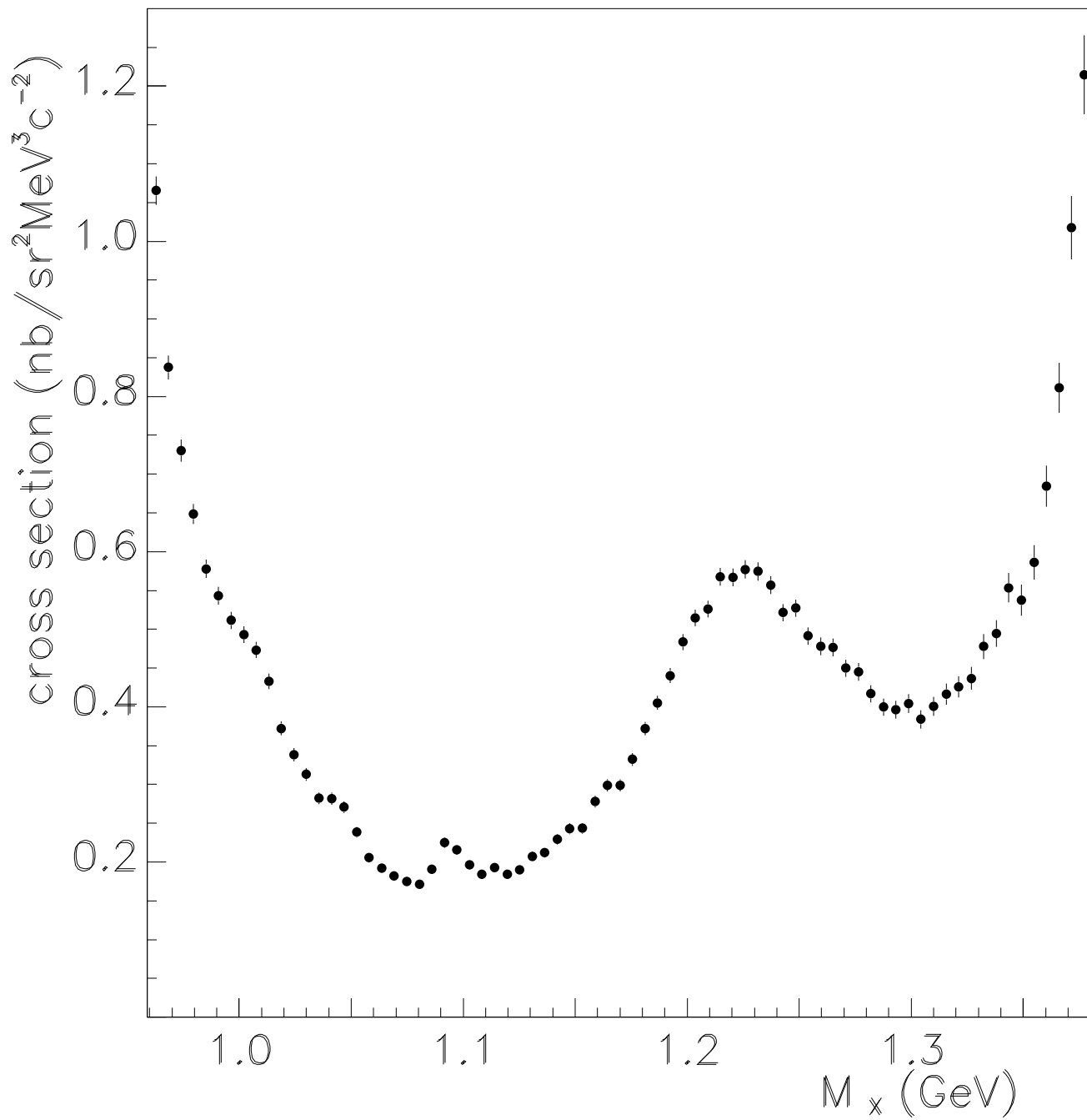


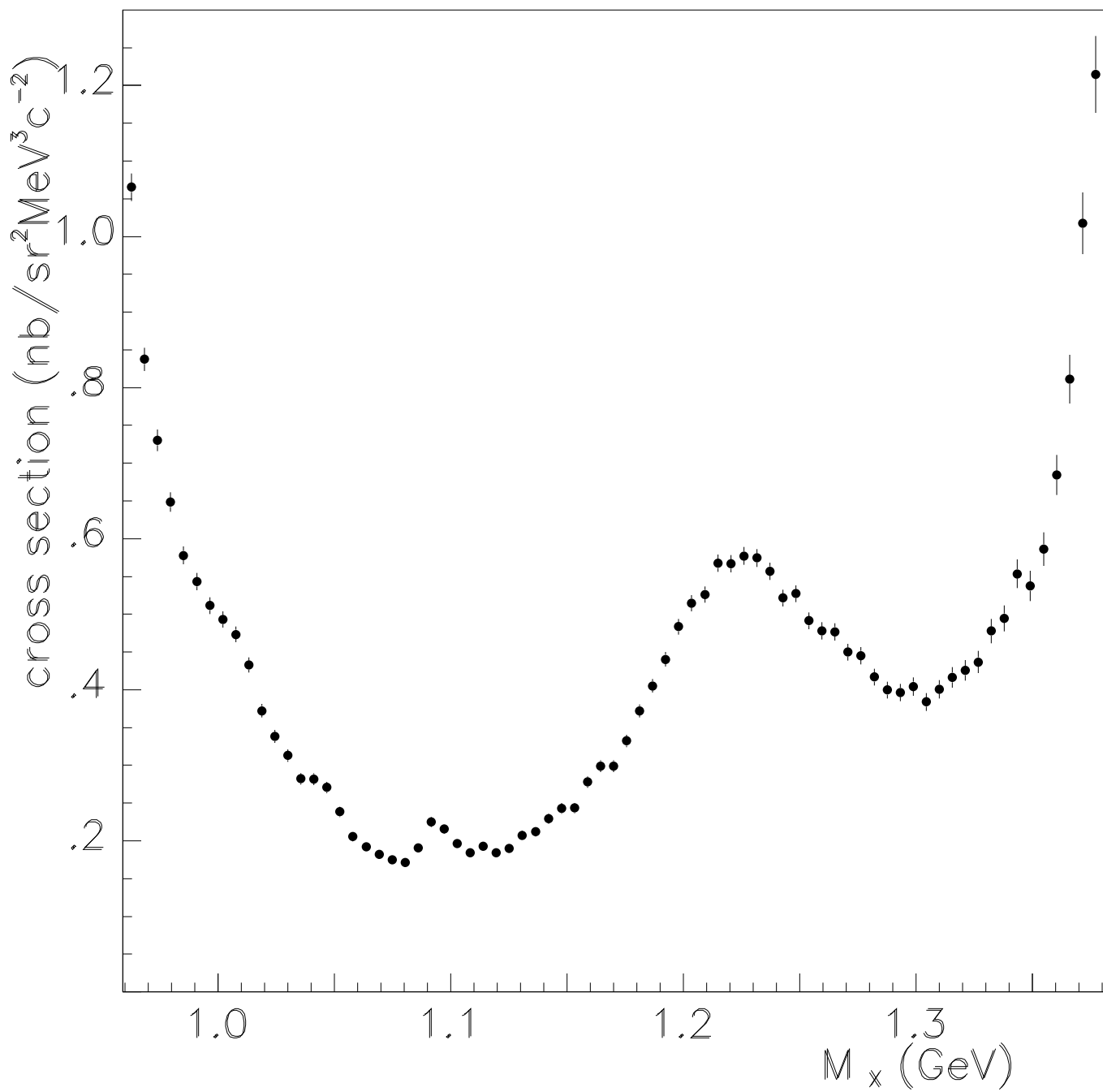


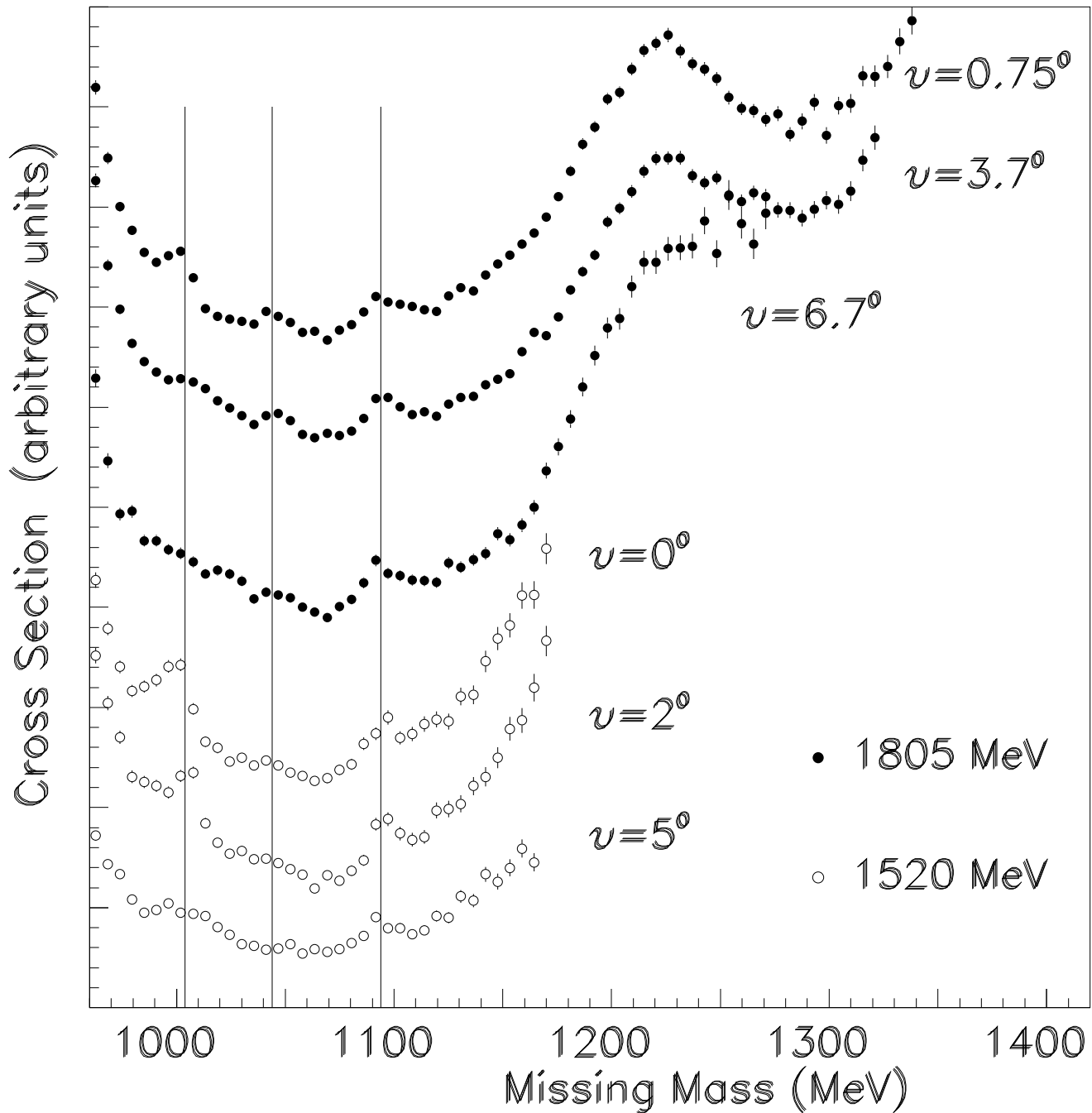


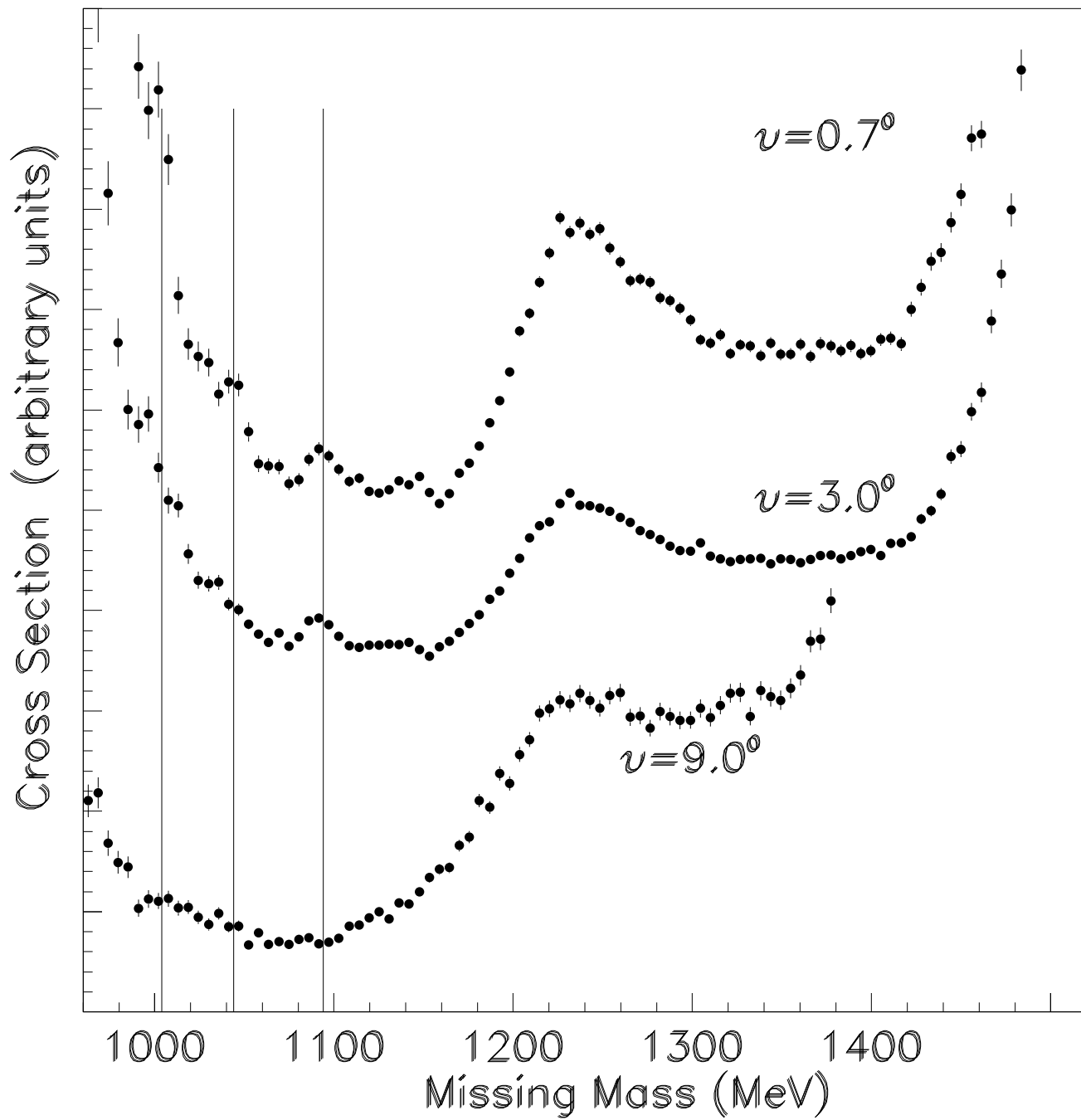


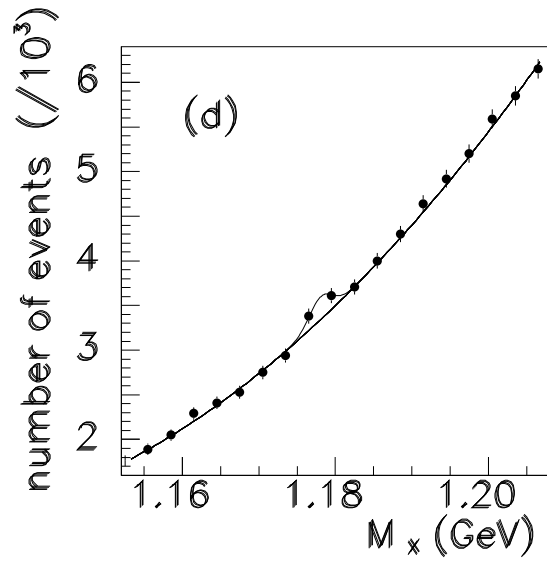
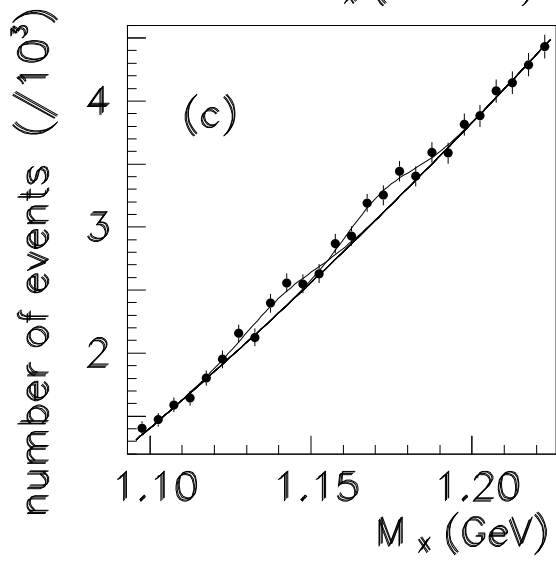
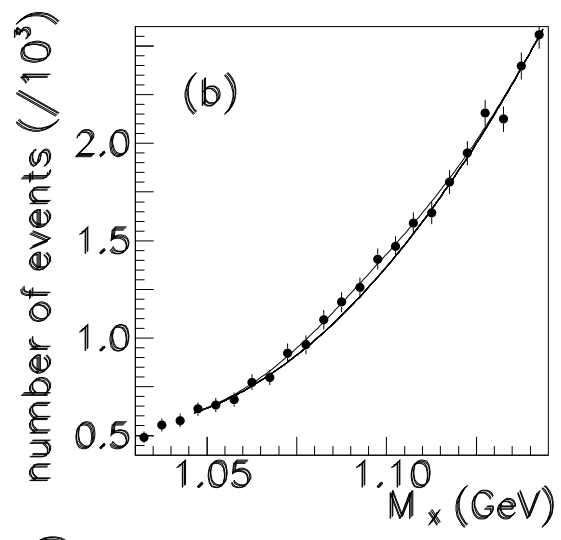
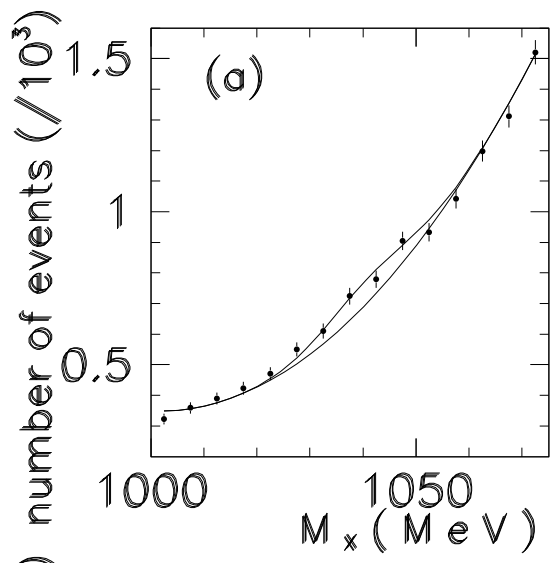


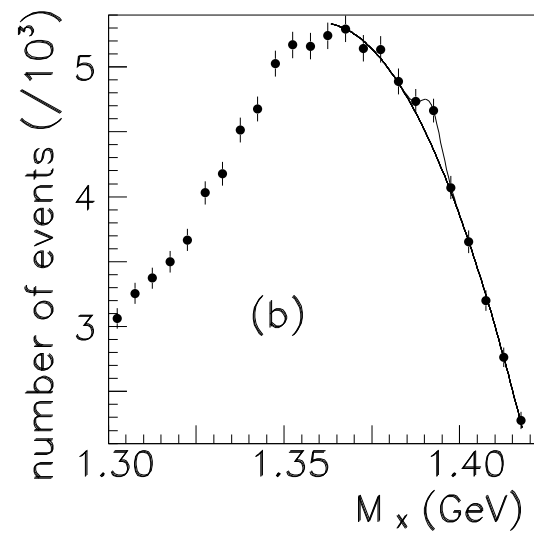
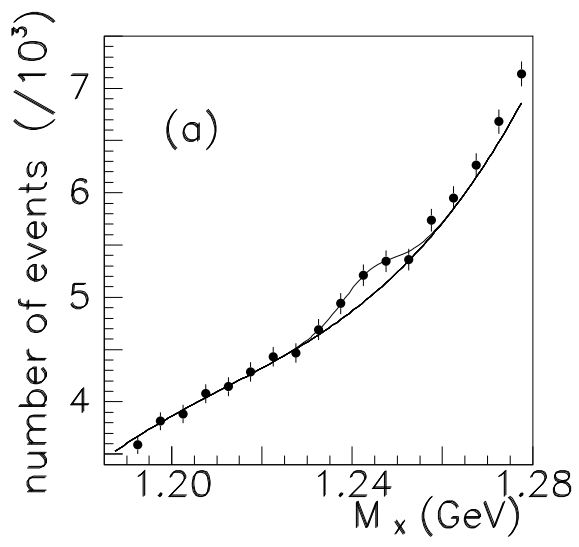


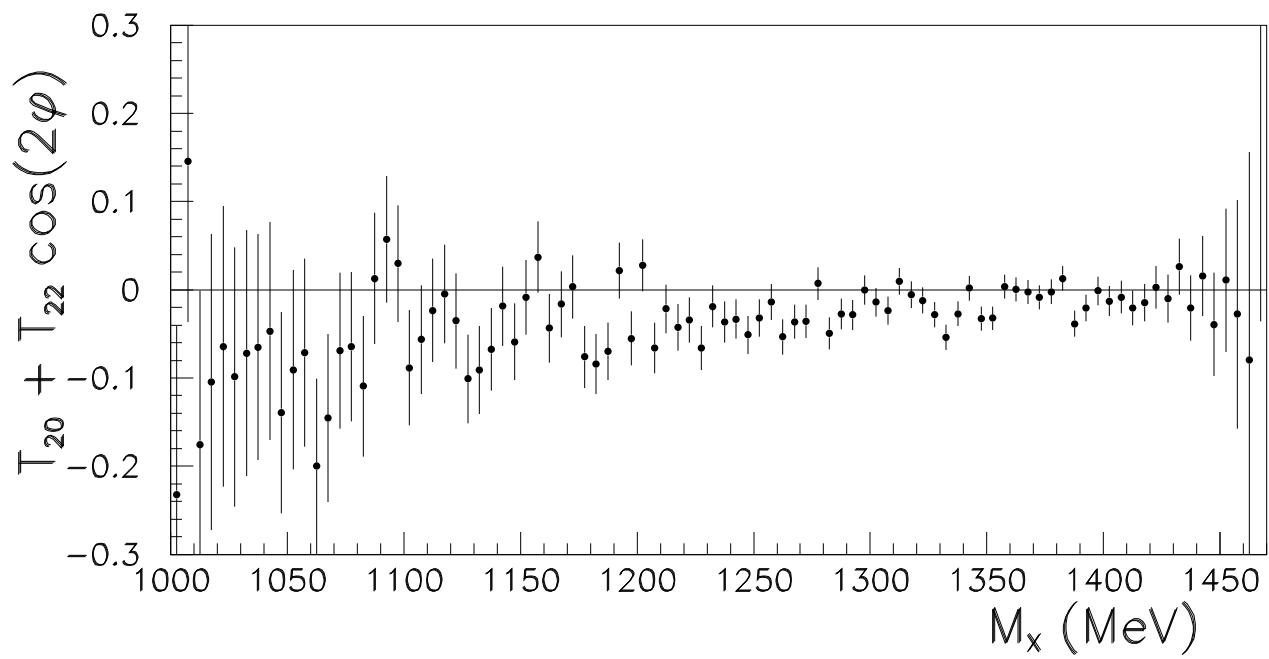


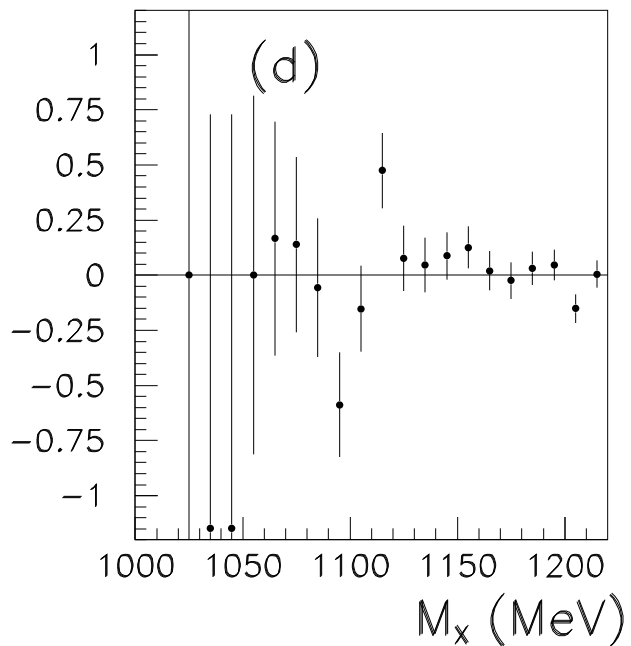
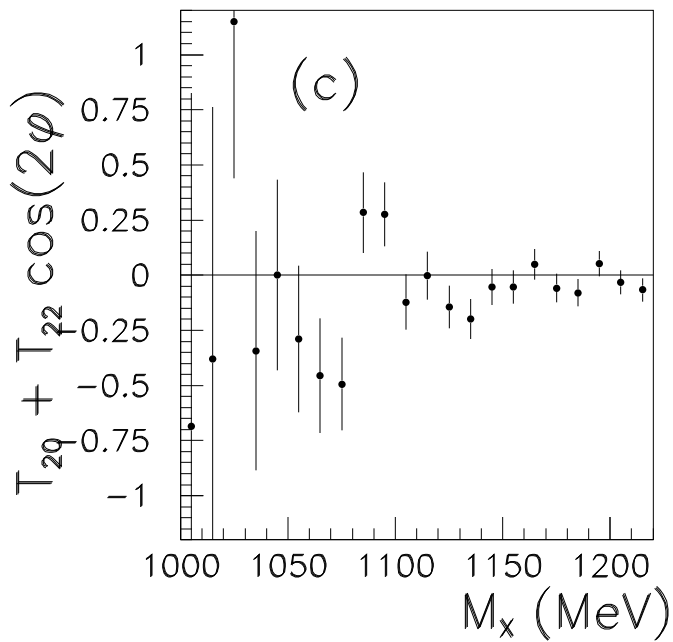
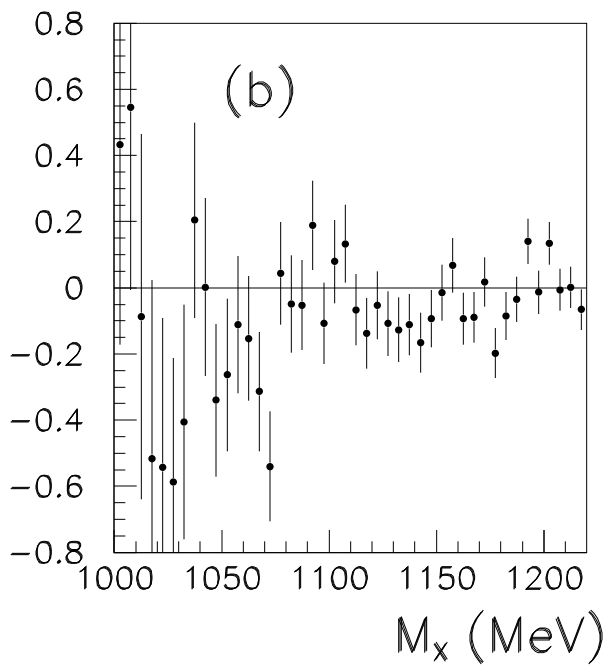
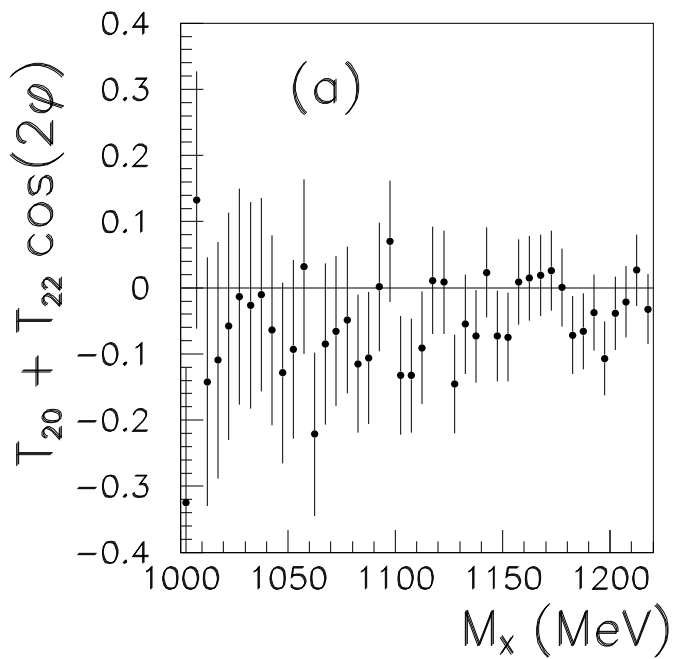


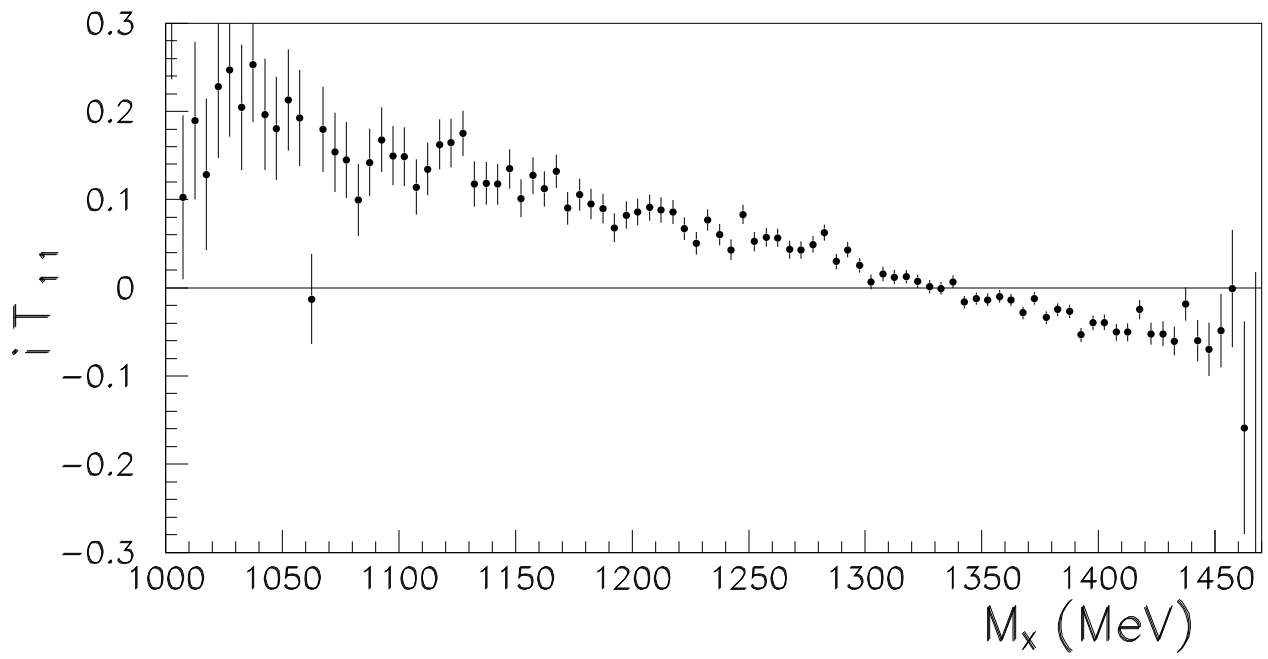


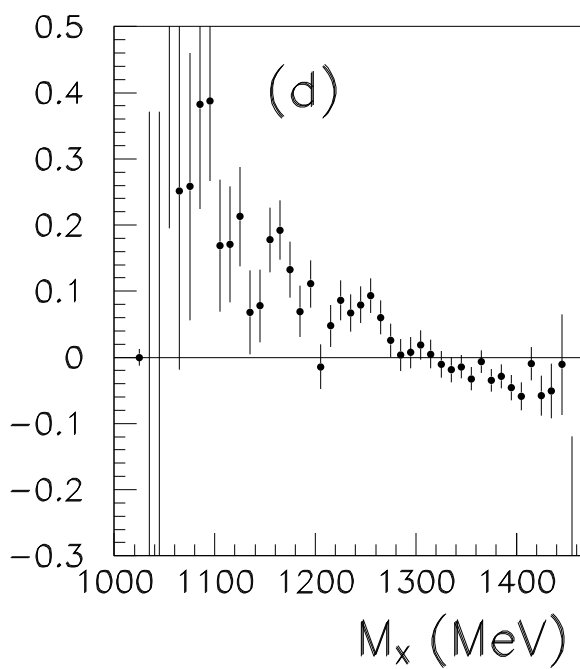
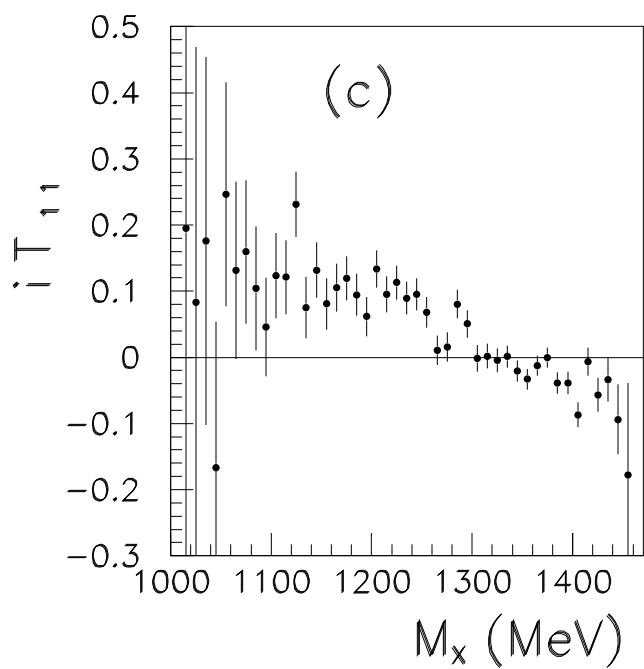
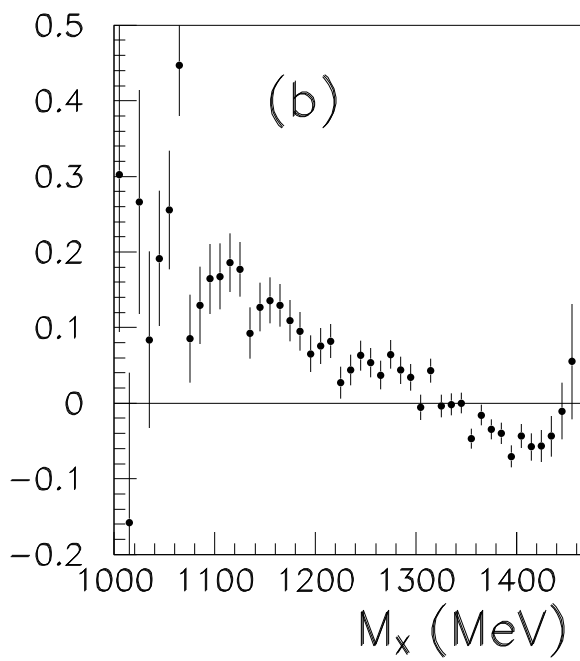
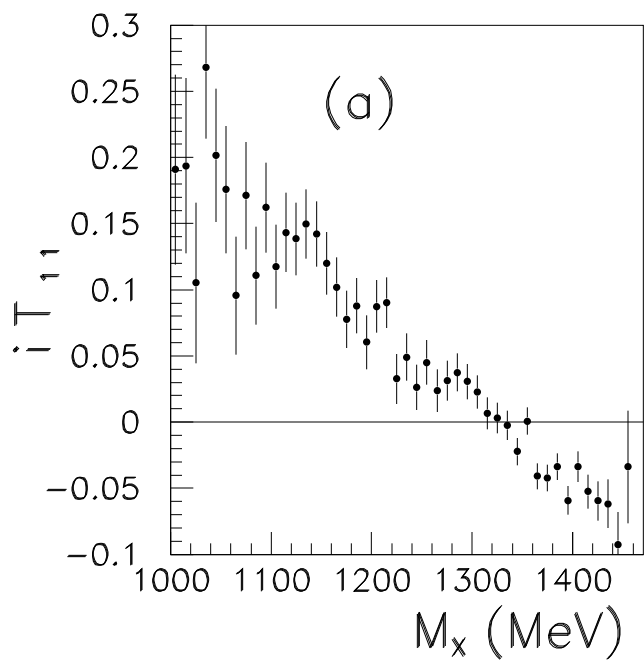


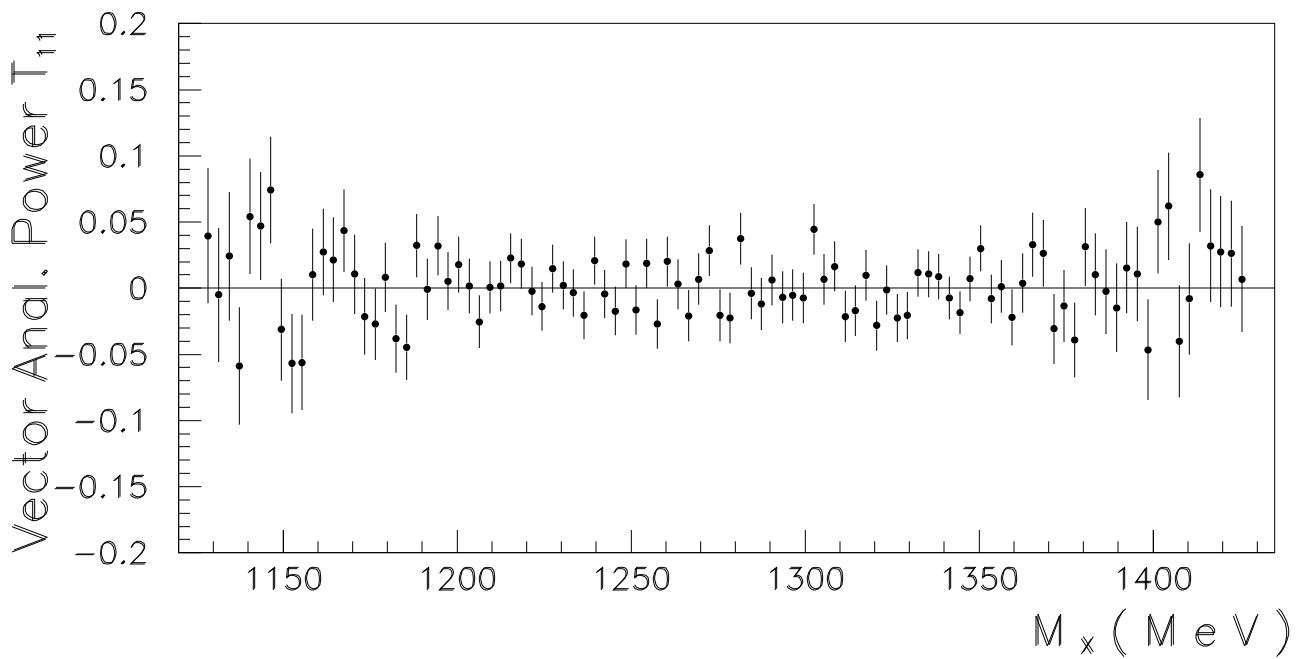
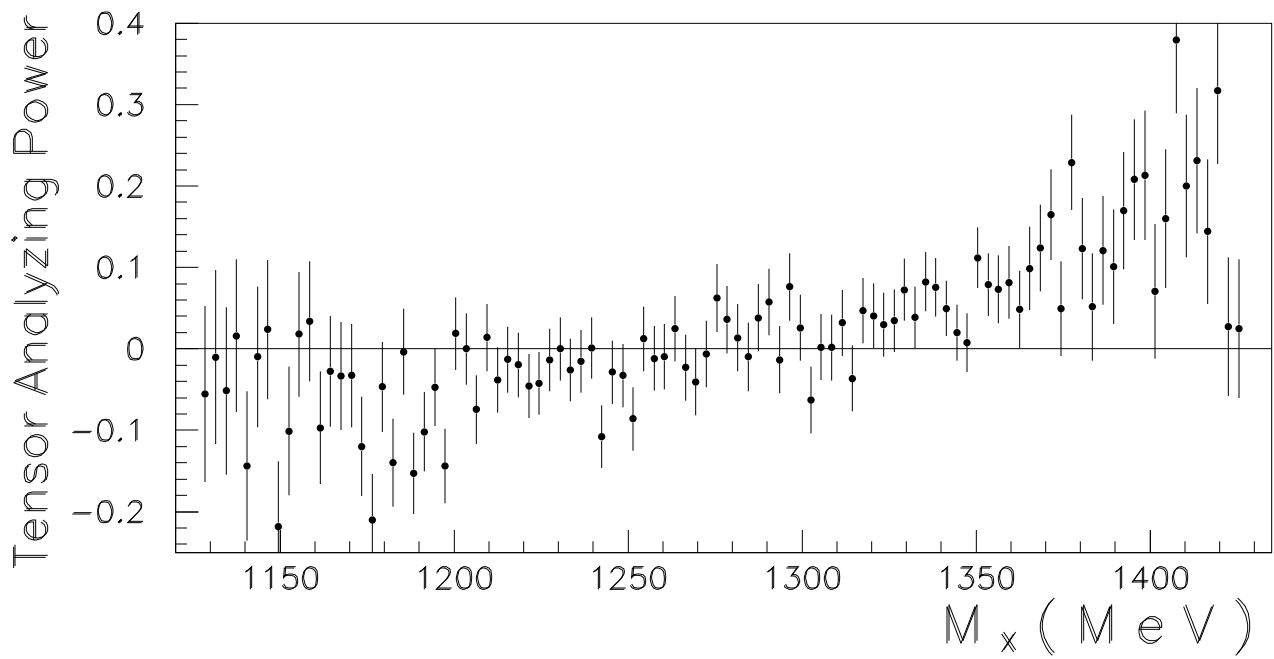


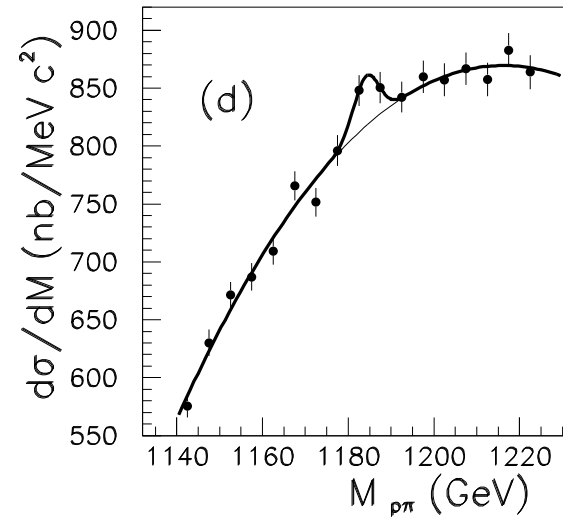
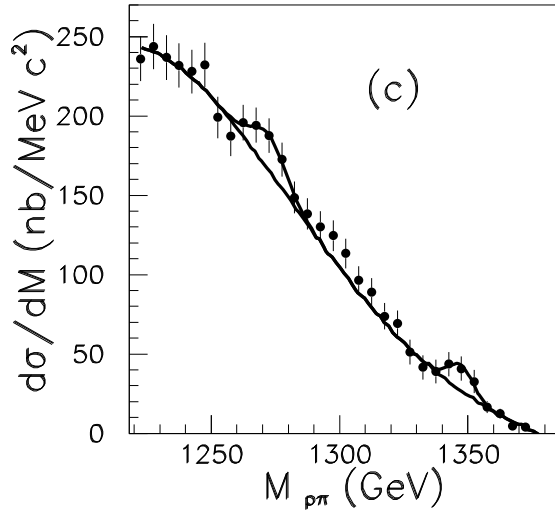
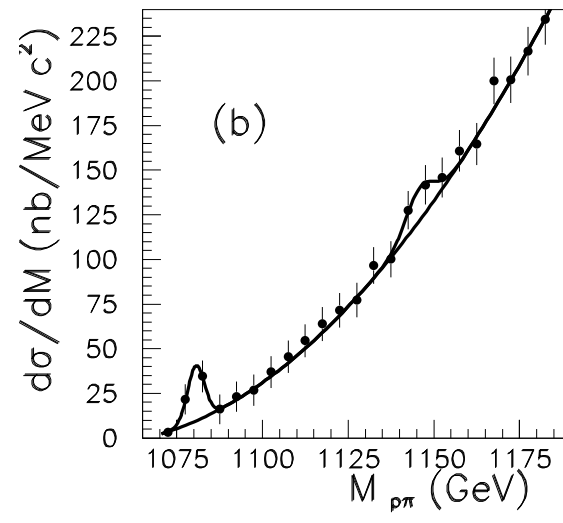
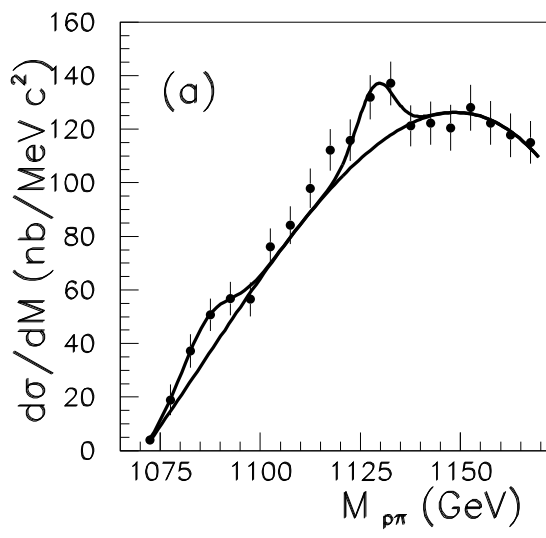


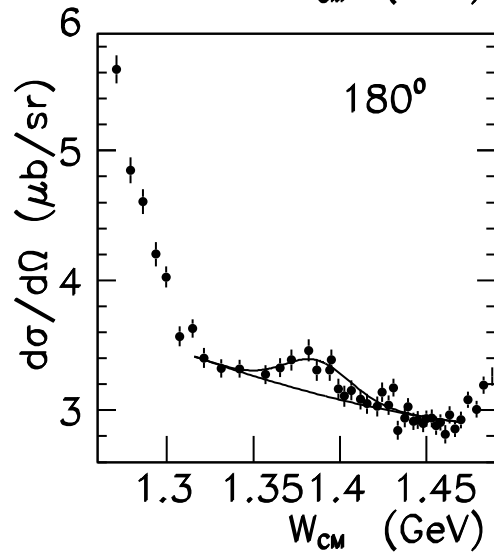
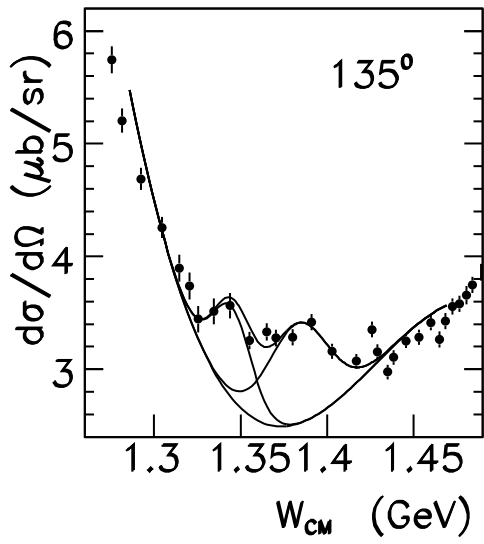
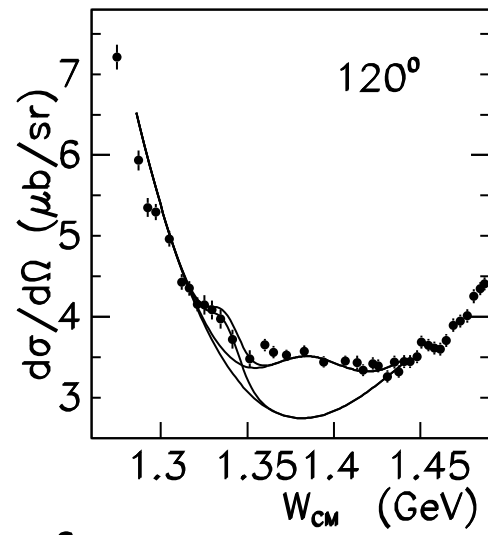
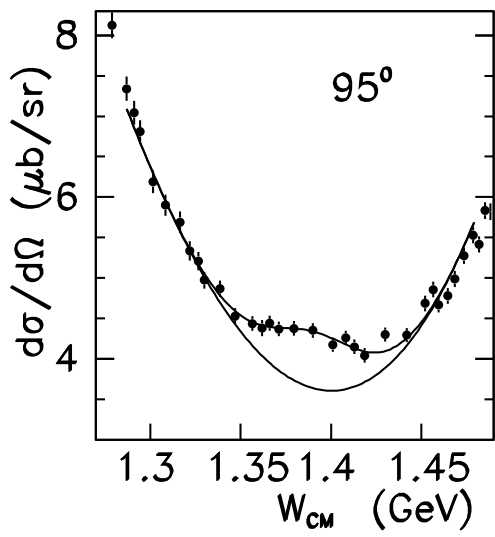


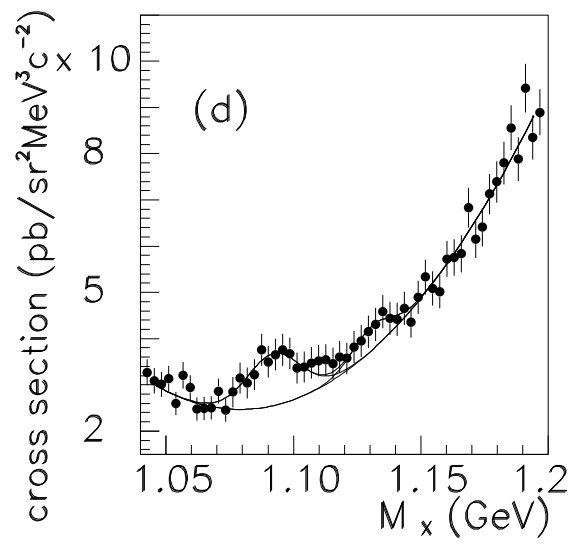
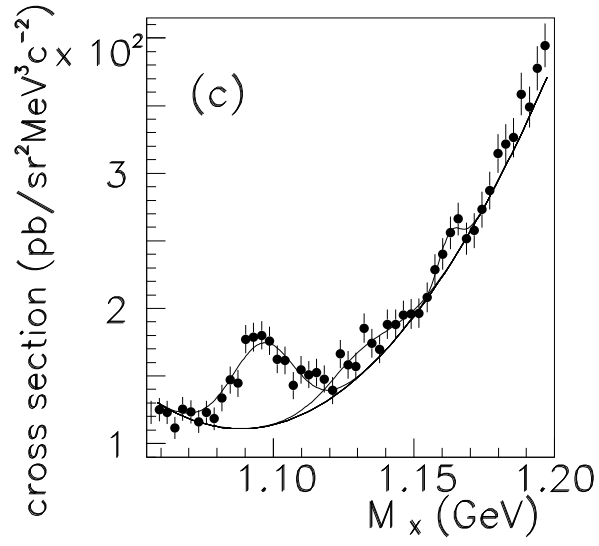
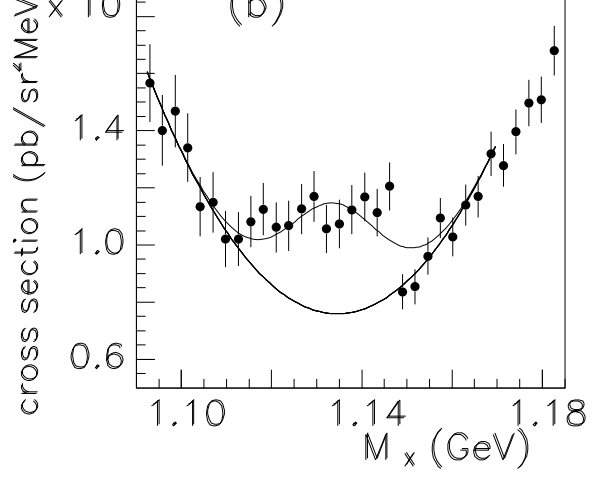
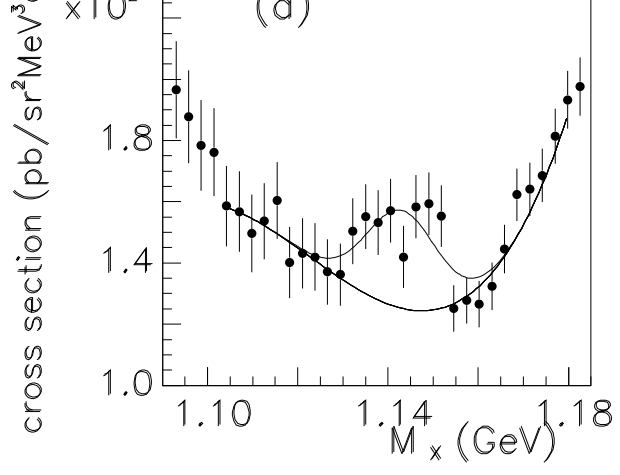


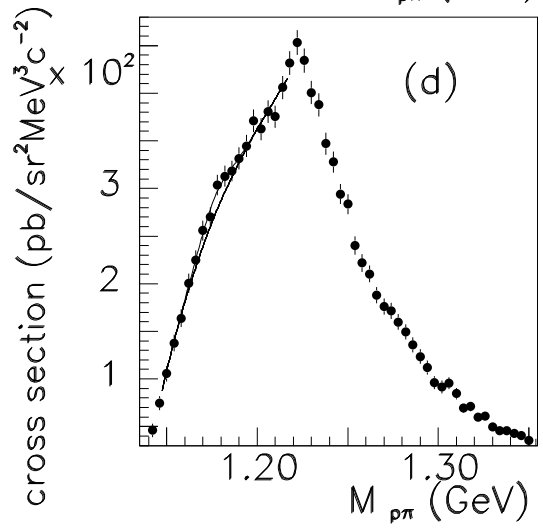
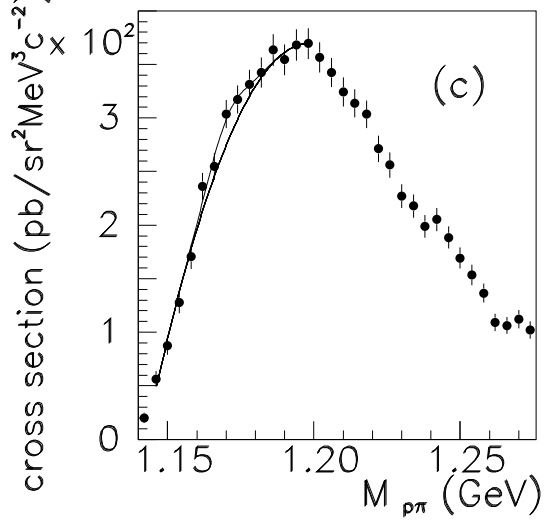
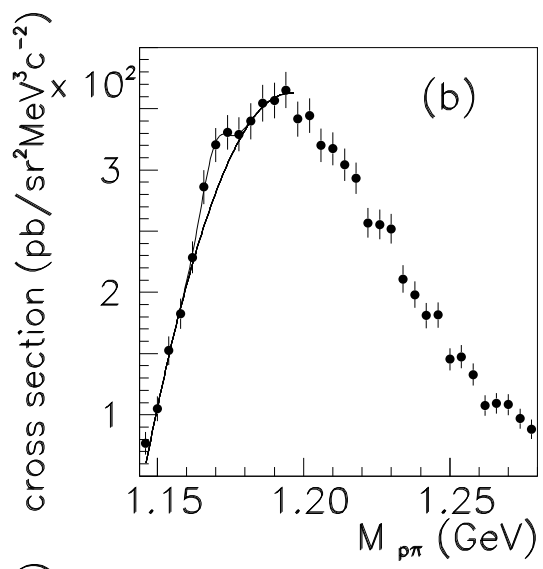
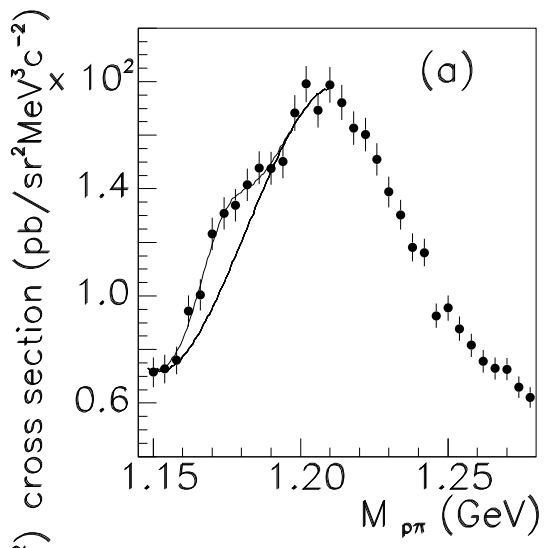


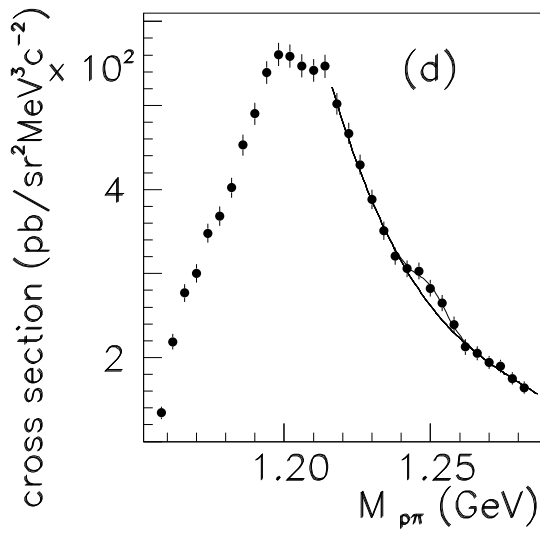
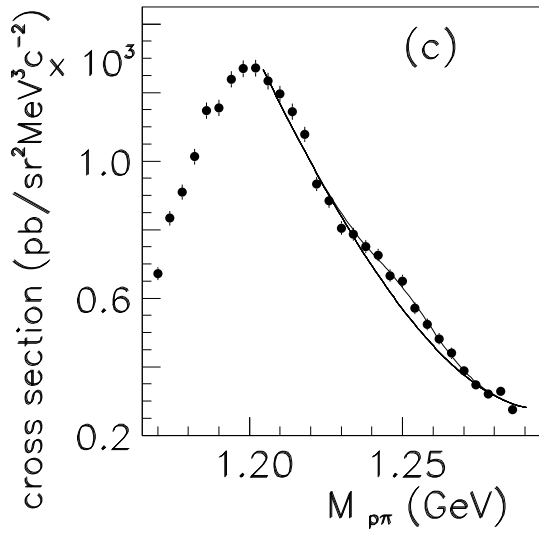
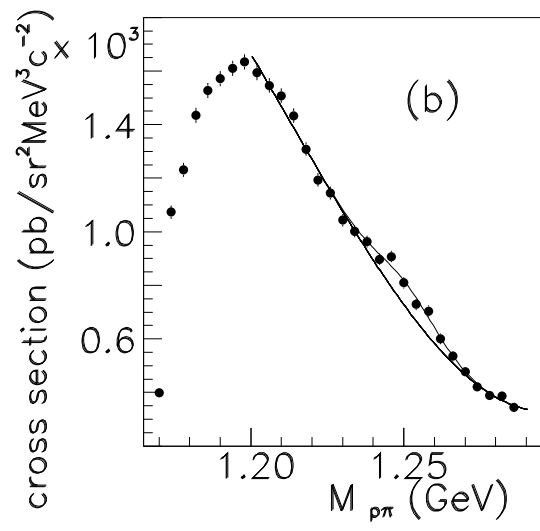
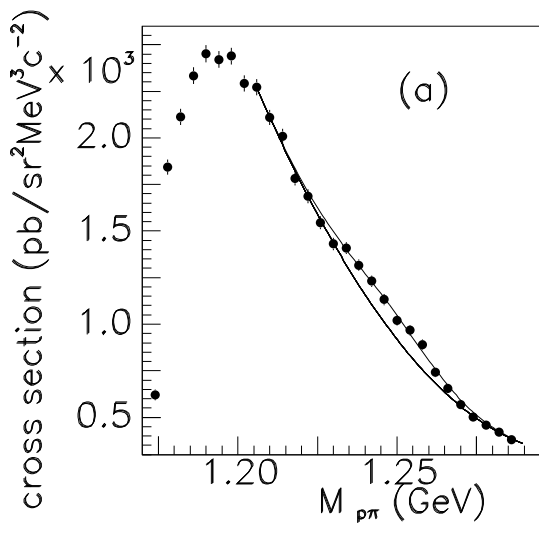


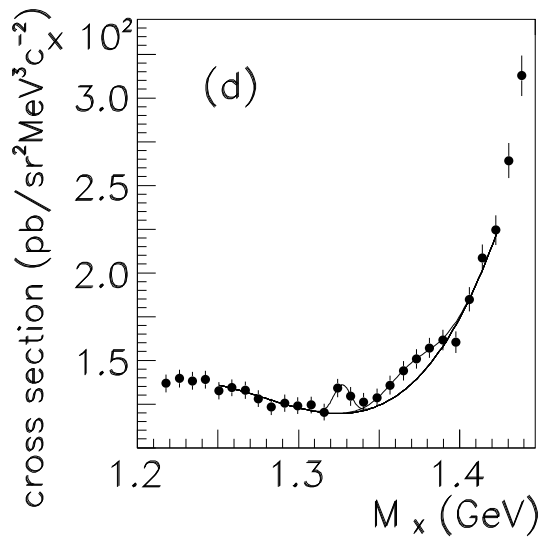
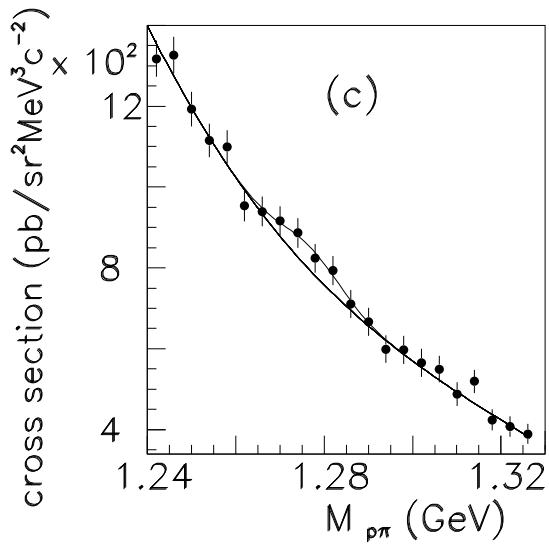
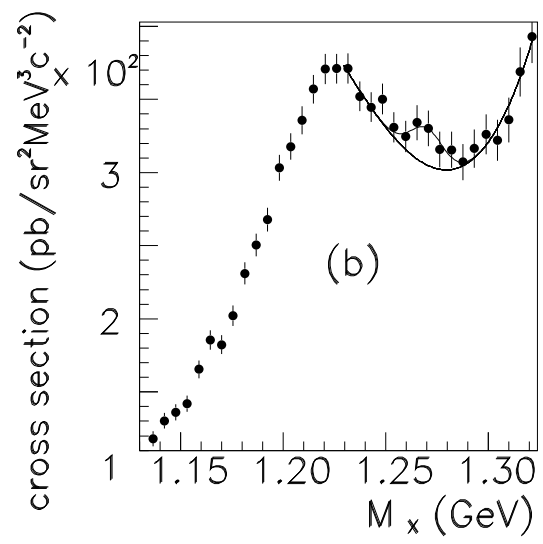
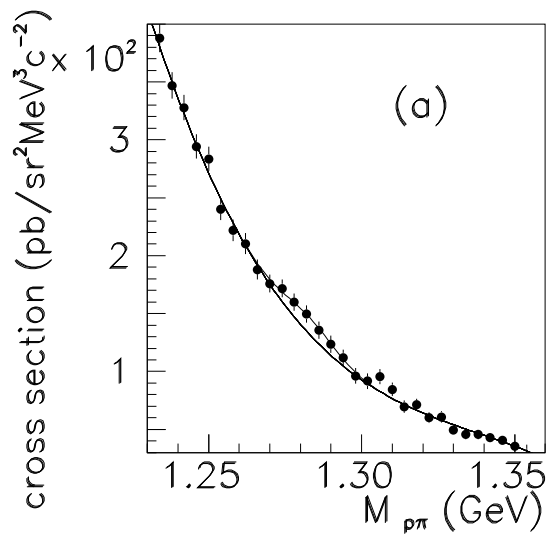


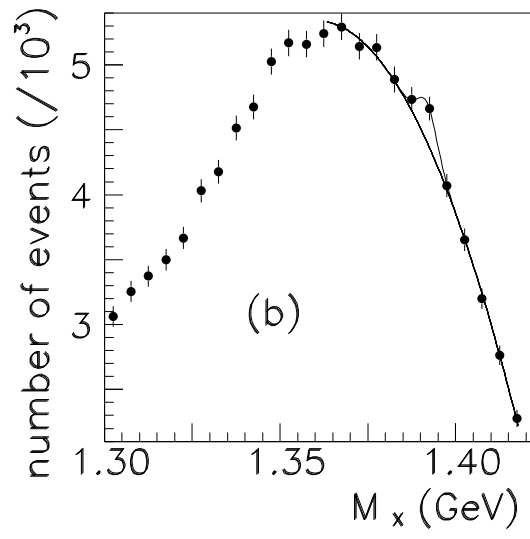
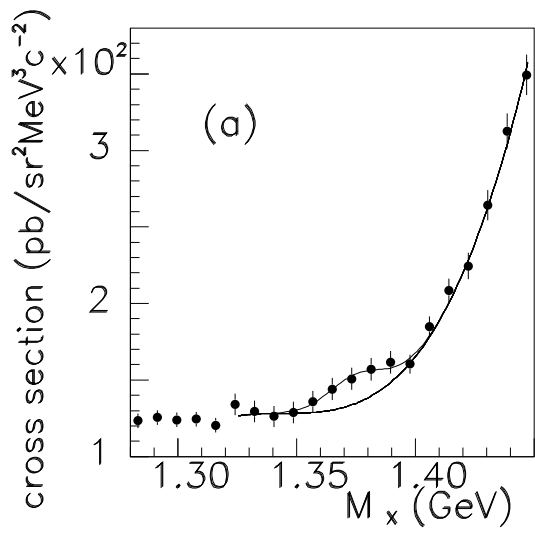


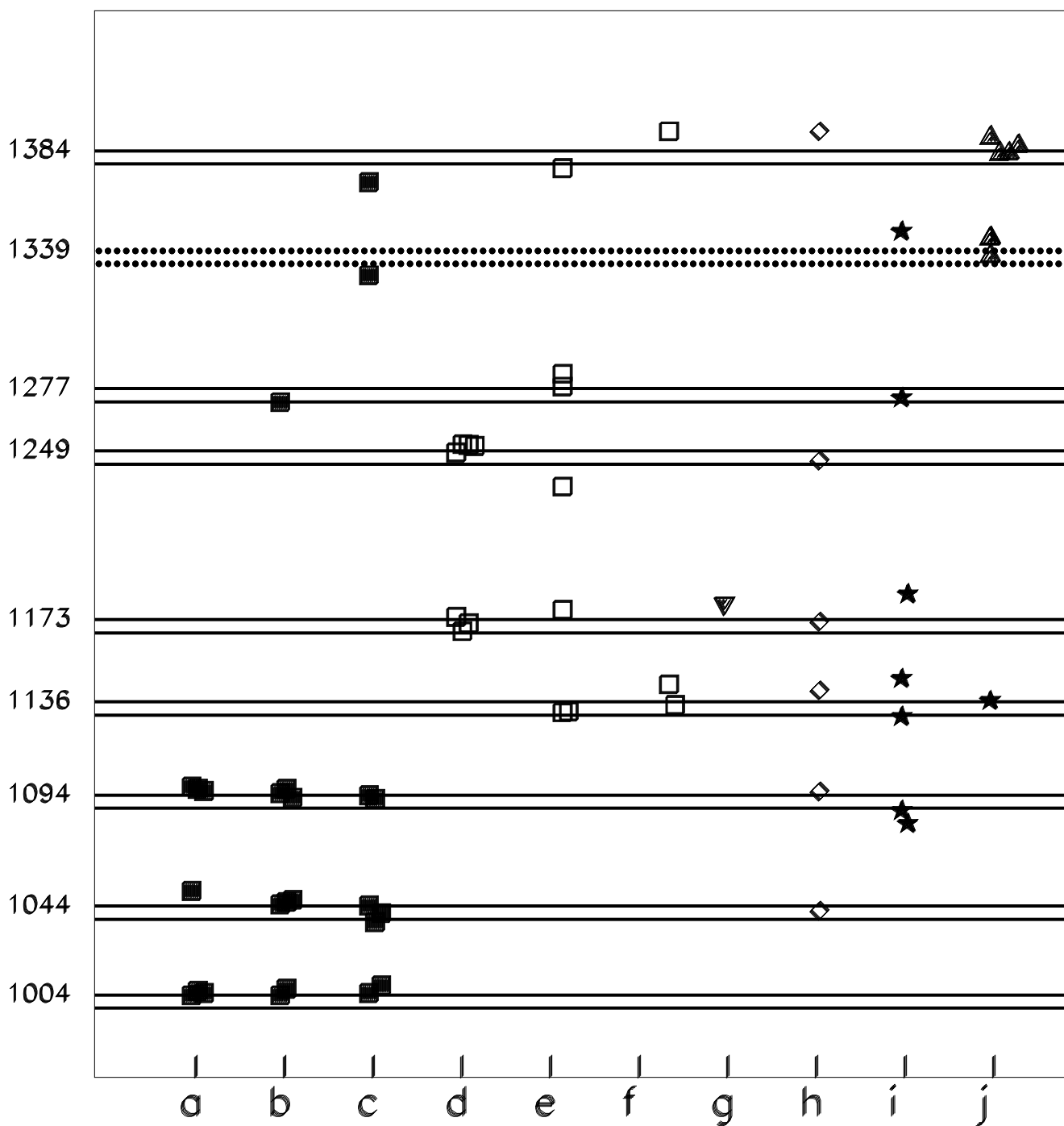












Experimental

Calculated

_____	1384	1440	$\frac{1}{2}, \dots, \frac{7}{2}$ $\frac{3}{2}, \frac{5}{2}$	_____	$\frac{1}{2}, \frac{3}{2}$ $\frac{3}{2}$
_____		1407	$\frac{1}{2}, \dots, \frac{5}{2}$ $\frac{5}{2}$	_____	$\frac{1}{2}, \dots, \frac{5}{2}$ $\frac{3}{2}$ $\frac{1}{2}, \frac{3}{2}$
-----	1339	1340	$\frac{3}{2}, \frac{5}{2}$ $\frac{3}{2}$ $\frac{5}{2}$	_____	$\frac{1}{2}, \frac{3}{2}$ $\frac{3}{2}$ $\frac{1}{2}$
_____	1277	1306	$\frac{1}{2}, \frac{3}{2}$ $\frac{1}{2}, \dots, \frac{5}{2}$	_____	$\frac{3}{2}$ $\frac{1}{2}, \frac{3}{2}$
_____	1249	1273	$\frac{3}{2}, \dots, \frac{7}{2}$	_____	$\frac{1}{2}$
_____		1239	$\frac{1}{2}, \dots, \frac{7}{2}$ $\frac{1}{2}$ $\frac{3}{2}$	_____	$\frac{1}{2}$ $\frac{3}{2}$ $\frac{1}{2}, \frac{3}{2}$
_____	1173	1206	$\frac{1}{2}, \frac{3}{2}$	_____	$\frac{1}{2}, \frac{3}{2}$
_____	1136	1139	$\frac{3}{2}, \frac{5}{2}$ $\frac{1}{2}$	_____	$\frac{1}{2}$ $\frac{1}{2}, \frac{3}{2}$
_____	1094	1106	$\frac{1}{2}, \dots, \frac{5}{2}$	_____	$\frac{1}{2}$
_____	1044	1039	$\frac{3}{2}$	_____	$\frac{1}{2}$
_____	1004	1005	$\frac{1}{2}, \frac{3}{2}$	_____	$\frac{1}{2}$
		939	$\frac{1}{2}$	_____	$\frac{1}{2}$
			Spin		Isospin

Experimental

Calculated $I(J^P)$

	1435	=====	$1/2(1/2^-, 3/2^-, 5/2^-)$
	1425	=====	$1/2(1/2^-, 3/2^-, 5/2^-)$
_____	1384		
	1365	_____	$1/2(3/2^-) \quad 3/2(3/2^-)$
-----	1339		
	1315	_____	$1/2(3/2^+)$
_____	1277		
	1275	_____	$1/2(1/2^+, 3/2^+, 5/2^+)$
_____	1249		
	1210	=====	$1/2(1/2^+, 3/2^+)$
	1200	=====	$1/2(1/2^+, 3/2^+) \quad 3/2(1/2^+, 3/2^+)$
_____	1173		
_____	1136		
	1140	_____	$1/2(1/2^+) \quad 3/2(1/2^+)$
_____	1094		
	1090	_____	$1/2(1/2^-)$
	1060	=====	$1/2(1/2^-, 3/2^-)$
_____	1044	=====	$1/2(1/2^-, 3/2^-) \quad 3/2(1/2^-, 3/2^-)$
_____	1004		
	990	_____	$1/2(1/2^-) \quad 3/2(1/2^-)$